RIMS-1772

Boussinesq convection and motions of boundary spheres in a rotating spherical shell

By

Keiji KIMURA

January 2013

京都大学　数理解析研究所

RESEARCH INSTITUTE FOR MATHEMATICAL SCIENCES

KYOTO UNIVERSITY, Kyoto, Japan

Boussinesq convection and motions of boundary spheres in a rotating spherical shell

Keiji Kimura

Research Institute for Mathematical Sciences,
Kyoto University, Kyoto, Japan

January 2013

Abstract

Boussinesq thermal convection in rotating spheres or spherical shells has been investigated for over half a century, not only as one of the fundamental models for global thermal convection, which is considered to occur in astronomical bodies, but also as a purely fluid mechanical problem.

There are a lot of researches for this convection problem, but most of the studies performed so far assume that the inner and outer spheres co-rotate, that is, both spheres rotate with the same angular velocity. However, the spheres need not be co-rotating in the actual astronomical bodies. It is a more natural setup that both spheres rotate freely due to the viscous torques operating on the surface of these spheres from the fluid. Therefore, in this thesis, we consider effects of the rotation of the inner and outer spheres on a fundamental behaviour of convective solutions of this Boussinesq thermal convection model.

First, we numerically evaluate torques on the inner and outer spheres induced by thermal convection in a co-rotating system in order to assess to what extent the convective motion changes the rotation rates of the spheres (Chap.2). We use stable traveling wave solutions which bifurcate at the critical points and propagate in the azimuthal direction (Kimura *et al.*, 2011). We find that the direction of the torque on the inner sphere is prograde when the rotation rate is small, while it becomes retrograde when the rotation rate is large. We also find that the torque on the inner sphere can be large enough to change the angular velocity of the inner sphere significantly even in a period of rotation. At the same time, using numerical weakly nonlinear analyses, we also examine generation mechanisms of mean zonal flows excited by thermal convection, since shear stress of the mean zonal flows on the spheres induces the axial component of the torques. We find that the nonlinear term in the energy equation is most effective to generate the global distribution of mean zonal flows, however, the azimuthal component of the nonlinear term in the Navier-Stokes equation becomes most important for generation of the torque on the inner sphere when the rotation rate is large.

Second, we develop a model of Boussinesq thermal convection in a rotating spherical shell allowing the inner sphere rotation (Chap.3). We obtain a bifurcation diagram of traveling wave solutions which bifurcate at the critical point and propagate in the azimuthal direction, by the Newton method and numerical eigenvalue calculations. These traveling wave solutions are stable in the region $R_c \leq R \lesssim 1.2 - 2R_c$ depending on the rotation rate, where R and R_c are the Rayleigh number and the critical value, respectively. The inner sphere rotates in the prograde direction when the rotation rate is small while it rotates in the retrograde direction when the rotation rate is large.

These rotating directions corresponds to directions of torques on inner sphere in the co-rotating system. The stable region of these traveling wave solutions is quantitatively similar to that in the co-rotating system. The structures of convective motions of these solutions, such as the radial component of velocity, are also quantitatively similar to those in the co-rotating system, but amplitude of mean zonal flows and propagating velocity of this traveling wave solutions are effectively changed by the inner sphere rotation. This tendency can be explained that the nonlinear effect by convective motions is small because these traveling wave solutions are stable only near the critical curve.

Third, we construct a model of the Boussinesq thermal convection allowing the rotation of both the inner and outer spheres (Chap.4). We perform numerical simulations in the range $4R_c \lesssim R \lesssim 5R_c$ at moderately rotating case. In this parameter region finite-amplitude convective solution transits from an equatorially symmetric pattern to an equatorially asymmetric one as the Rayleigh number is increased. We find that the route of this transition in the system allowing rotation of both spheres is different from that in the co-rotating system: $\mathrm{QP}^{\mathrm{S}} \to \mathrm{QP}^{\mathrm{A}} \to \mathrm{C}^{\mathrm{A}}$ in the co-rotating system while $\mathrm{QP}^{\mathrm{S}} \to \mathrm{C}^{\mathrm{S}} \to \mathrm{C}^{\mathrm{A}}$ in the system allowing rotation of both spheres, as the Rayleigh number is increased, where QP^{S} is an equatorially symmetric quasi-periodic solution, QP^{A} an equatorially asymmetric quasi-periodic solution, C^{S} an equatorially symmetric chaotic solution, and C^{A} an equatorially asymmetric chaotic solution. The transition route in the system where only the inner sphere rotation is permitted is exactly same as that in the system allowing rotation of both the spheres. Therefore, we conclude that the inner sphere rotation causes the different transition route from that in the co-rotating system.

Contents

List of Figures

List of Tables

Chapter 1

Introduction

There are a lot of astronomical bodies in the universe and they possibly show a great wide variety of their features. However, global thermal convection is thought to occur commonly in many of these astronomical bodies, due to the internal heat sources and/or the external cooling. For example, the Sun has a convective envelope around the radiative core, the band structure observed in the giant planets is considered to be generated by the internal thermal convection, and fluid motions in the liquid metallic cores of the terrestrial planets would be the origin of their intrinsic magnetic fields.

The Boussinesq thermal convection in rotating spheres and spherical shells, proposed by Chandrasekhar [1], is one of the fundamental frameworks to investigate behaviour of this kind of global thermal convection. This convection model has been vigorously investigated for over half a century.

The critical Rayleigh numbers, critical frequencies and critical modes [1] have been investigated theoretically and numerically, and now their behaviours come to be known in wide parameter ranges. Finite-amplitude convection patterns also have been actively investigated through numerical simulations. Thanks to the recent remarkable progress of computational ability, some recent large scale numerical simulations with high-resolutions obtained finite-amplitude convective solutions similar to the observed flow fields, such as the zonal-band structures [2] of the solar planets. Although these solutions could propose possible dynamics realized in the atmospheres of the planets,

[1] The Rayleigh number means the degree of thermal instability in a thermal convection system. As the Rayleigh number is increased, thermal convection occurs at a certain Rayleigh number. This Rayleigh number is called the critical Rayleigh number, and the emerging convection patterns are referred to the critical modes.

[2] Zonal-band structure means a structure consists of alternating prograde (eastward) and retrograde (westward) jets, where prograde means the direction same as the rotation direction of reference, while retrograde does the opposite direction against the rotation direction of reference.

they may not reproduce the atmospheric flow fields adequately, because control parameters of these large scale numerical simulations are still far from the expected values of the parameters in actual astronomical bodies. It is severe to perform numerical simulations with realistic parameters for actual astronomical bodies even when computational ability is highly developed in the near future.

On the other hand, using numerical time integrations, some researchers have been investigating fundamental behaviour of convection patterns, *i.e.*, what kinds of convection patterns appear or disappear as the Rayleigh number is increased from the critical value. Transition of convective solutions from critical modes to chaotic solutions has been gradually revealed. Nevertheless, global behaviour of the convective solutions in this system is not yet well understood. Especially, stability and a bifurcation structure of convective solutions of this model have not been investigated, which are one of the fundamental information to understand global behaviour of convective solutions. We consider this is because most of the researchers have used the time integration method to study the finite-amplitude convection patterns. This method has two difficulties: (i) the unstable solutions cannot be obtained, (ii) it requires quite long integration time to find the marginal stability point. As a result, it is difficult to investigate many cases in wide parameter ranges.

Therefore, in order to investigate the bifurcation structure of this convection model, we used the Newton method instead of the time integration method, and obtained stability and the bifurcation diagram of traveling wave solutions propagating in the azimuthal direction which bifurcate at the critical points (Kimura *et al.* [2]). The bifurcation structure can be investigated systematically and efficiently with the Newton method, thanks to the following advantages: (i) not only stable but also unstable solutions can be obtained, (ii) the number of the steps for convergence of the solutions is small (less than 10 steps in our calculations).

Based on the results of Kimura *et al.* (2011) [2], in this thesis, we consider effects of the rotation of the inner and outer spheres on fundamental behaviour of convective solutions of this Boussinesq thermal convection model. There are many researches to investigate this thermal convection in rotating spherical shells, but most of the studies performed so far assume that the inner and outer spheres co-rotate, that is, both spheres rotate with the same angular velocity. However, the spheres need not be co-rotating in the actual astronomical bodies. It is a more natural setup that both the spheres rotate freely due to the torques operating on the surface of these spheres from the fluid.

Therefore, in this thesis, we construct a model of Boussinesq thermal convection in a rotating spherical shell allowing rotation of the inner and

outer spheres, and investigate fundamental behaviour of convective solutions through comparing with those in the co-rotating system.

In the following of the introduction, we briefly summarize previous works for Boussinesq thermal convection in rotating spheres and spherical shells in Sec. 1.1. The summary of our previous study, Kimura *et al.* [2], is described in Sec. 1.2. The motivation, viewpoint and results in this thesis are summarized in Sec. 1.3.

1.1 Research history of Boussinesq thermal convection in rotating spheres and spherical shells

The critical Rayleigh numbers, critical frequency and critical modes of Boussinesq thermal convection in rotating spheres and spherical shells have been investigated theoretically [3, 4, 5, 6, 7, 8, 9] and numerically [10], since the pioneering works by Chandrasekhar [1], Roberts [11] and Busse [12, 13], and their behaviours come to be known in wide parameter ranges.

When the rotation rate is small, retrograde propagating convection pattern bending along the shell emerges as a critical mode [12, 14] except for the cases of thick shells and large Prandtl numbers, where the axisymmetric convection pattern appears as a critical mode [15]. When the rotation rate is large, various convection patterns emerge as critical modes: a prograde propagating columnar mode [13], a spiralling columnar mode which has a spiralling structure spreading from inner to outer sphere [16], an equatorially attached mode which concentrates near the equatorial surface [4, 5, 17], and a multi-cellular mode which have some convection cells in the radial direction [18, 19]. However, behaviour of critical parameters and critical modes in extremely rapid rotation region are still challenging due to necessary massive computational resources for large scale eigenvalue calculations [20, 21].

Finite-amplitude convection has also been studied actively by using numerical time integrations thanks to the recent massive powerful computers [22, 23, 24, 25]. Especially, finite-amplitude convection solutions similar to the observed zonal-band structures of the solar planets were obtained by recent large scale numerical simulations. Heimpel and Aurnou [23] showed that the multiple zonal-band structure on the outer sphere can be obtained in rapidly rotating thin shell cases; this flow structure corresponds to that in the previous studies by Busse [26, 27, 28]. Their surface flows are similar to the zonal-band structure observed on the surface of Jupiter [29] and

	Radius ratio	Prandtl	Taylor	Rayleigh
Heimpel *et al.* [23]	$0.85 - 0.9$	0.1	$\sim 10^{11}$	$\lesssim 10^{9}$
Aurnou *et al.* [24]	0.75	$0.1 - 1$	$\lesssim 10^{10}$	$\lesssim 10^{11}$
Ice giants	$0.80 - 1$	0.1	10^{30}	10^{29}
Gas giants	$0.80 - 1$	0.1	10^{36}	10^{33}

Table 1.1: Comparison of non-dimensional control parameters of Boussinesq thermal convection in rotating spherical shells with those of the expected astronomical bodies. The second and third rows show the control parameters used in Heimpel and Aurnou [23] and Aurnou *et al.* [24]. The fourth and fifth rows show the expected values of these parameters for corresponding astronomical bodies, which are described in Aurnou *et al.* [24], while the actual physical values are highly uncertain. Here the radius ratio is defined as $r_{\rm in}/r_{\rm out}$, the Prandtl number ν/κ, the Taylor number $(2\Omega d^2/\nu)^2$ and the Rayleigh number $\alpha g_{\rm out}\Delta T d^3/(\nu\kappa)$. $r_{\rm in}$ and $r_{\rm out}$ are radii of the inner and outer spheres, respectively. ν is the kinematic viscosity, κ the thermal diffusivity, α the thermal expansion coefficient, $g_{\rm out}$ the gravity given on the outer sphere, Ω the rotation rate of the reference frame, ΔT the temperature difference of the inner sphere from the outer sphere.

Saturn [30]. Aurnou *et al.* [24] showed that retrograde zonal flows [3] can be generated near the outer sphere around the equatorial region when the shell is thin and the Rayleigh number is sufficiently large. This zonal flow structure could explain that in the ice giants, Uranus [31, 32] and Neptune [33]. Note that, however, the parameters used in these numerical simulations are far from the expected values of the actual planets (Table 1.1), although the expected value of the parameters for the planets are uncertain. Therefore, these convective solutions may not represent the flow fields of the planetary atmospheres adequately.

On the other hand, transition of convective solutions from critical solutions to chaotic solutions has been gradually revealed in the parameter space [18, 19, 34, 35].

Ardes *et al.* [18] showed that, as the Rayleigh number is increased, transition occurs from traveling wave solutions which propagate in the azimuthal direction to vacillating solutions, quasi-periodic solutions and chaotic solutions succeedingly. Grote and Busse [35] showed that, as the Rayleigh number is increased larger than that in Ardes *et al.* [18], localized turbulent convec-

[3] Zonal flow means the azimuthally averaged azimuthal component of velocity.

tion pattern appears and is sustained. As the Rayleigh number is further increased, the relaxation oscillation occurs, *i.e.*, kinetic energy slowly decays periodically after its rapid increasing.

Simitev and Busse [19] showed that, when the Prandtl number is relatively small, the spiralling columnar convection emerging in rapidly rotating cases becomes unstable at a certain large Rayleigh number, and found that the amplitude vacillations, shape vacillations and the chaotic behaviours occur when the Rayleigh number is further increased. On the other hand, when the Prandtl number becomes small, the equatorially attached convection pattern emerging as a critical mode becomes modulate but keeps still concentrated near the outer sphere at a larger Rayleigh number. As the Rayleigh number is further increased, the equatorially attached eddies spread into interior region and are detached in some cases.

Chossat [36] mathematically investigated a bifurcation point of conductive rest state (basic state) using asymptotic analyses by expanding the governing equations both with the Rayleigh number and the rotation rate. He showed that, when the rotation rate is small but positive and the ratio of the inner and outer radii is 0.3, the degeneracy of solution space can be resolved and an axisymmetric solution bifurcates. This bifurcation is slightly transcritical. He also showed the conditions that the stable region of this bifurcated solution exists [4] . However, due to limit of the perturbation analyses, the behaviour and stable region of the bifurcated solutions could not be known.

In the next section we summarize our previous work, Kimura *et al.* [2], and show a bifurcation diagram of finite-amplitude convective solutions.

1.2 Summary of Kimura *et al.* (2011)

In our previous work [2], we obtained the bifurcation diagram of the finite-amplitude traveling wave solutions with the Newton method in supercritical and moderately rotating cases, because the convective solutions can be resolved with relatively low spatial degree of freedom (Fig. 1.1). We chose the boundary condition as impermeable, no-slip and isothermal on both spheres. The ratio of the inner and outer radii of the shell and the Prandtl number are fixed to 0.4 and 1 respectively, while the Taylor number is varied from 52^2 to 500^2 and the Rayleigh number is from about 1500 to 10000. In this parameter region, the critical azimuthal wavenumber is always 4. The finite-amplitude

[4] Chossat [36] also showed that, when a spherical shell do not rotate, the bifurcation occurs supercritically but the solution space keeps degenerated. He showed the conditions that the stable region of this supercritically bifurcated solution exists.

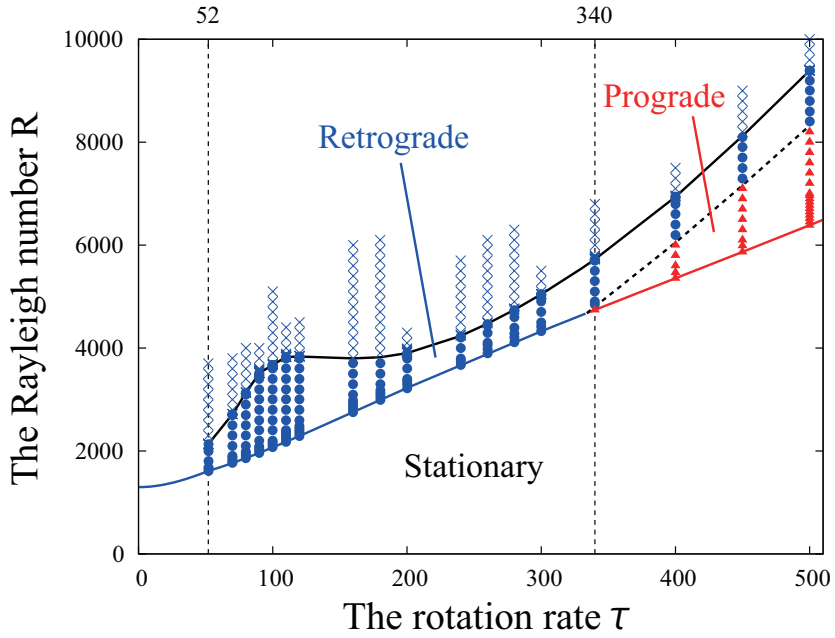

Figure 1.1: A bifurcation diagram of the stable TW4s, which is shown in Fig. 4 of Kimura *et al.* [2]. The propagating direction of the solution is shown by a blue circle (retrograde) and a red triangle (prograde). The lower solid curve shows the marginal stability of the stationary (conductive) solution, where the blue curve ($\tau < 340$) shows that the propagating direction is retrograde, and the red curve ($\tau \geq 340$) prograde. All circles and triangles mean that the nonlinear solutions are stable. TW4s become unstable above the upper black solid line. The propagating velocity v_p vanishes on the dashed line. The blue crosses mean that the nonlinear solutions propagating in the retrograde direction are unstable.

traveling wave solutions, which have four-fold symmetry in the azimuthal direction, bifurcate supercritically from the critical point. Hereafter we call these traveling wave solutions TW4s.

Figure 1.1 shows the obtained bifurcation diagram, which indicates stable TW4s and their propagating directions in $\tau - R$ parameter space, where τ is the square root of the Taylor number and R is the Rayleigh number. TW4s bifurcate supercritically from the conductive rest state at the critical points and are stable in the region $R_c \leq R \lesssim 1.2 - 2R_c$ depending on the rotation rate τ, where R_c is the critical Rayleigh number. TW4s propagate in the retrograde direction for $\tau \leq 330$. On the other hand, in $\tau \geq 340$, where the propagating direction of the critical modes becomes prograde,

the propagating direction of TW4s changes to retrograde as the Rayleigh number is increased. These all the transitions of the propagating velocity are continuous, and the associated transitions of the convection structures are also continuous.

We also found that the transition of the propagating direction of TW4s near the critical curve can be interpreted with the vortex stretching/shrinking mechanism proposed by Takehiro [37]. On the other hand, we confirmed quantitatively that the transition of the propagating direction of TW4s in finite-amplitude region can be interpreted with the advection of the vortex tube by the mean zonal flow, which is generated by the nonlinear effect of thermal convection. The comprehensive studies in $\tau - R$ parameter space by the Newton method made it possible to find this advection mechanism through detailed comparison between different solutions in different parameters.

1.3 Motivation and summary of this thesis

Based on the results of Kimura *et al.* (2011) [2] shown in the previous section, in this thesis, we consider effects of the rotation of the inner and outer spheres on fundamental behaviour of convective solutions of this Boussinesq thermal convection model. It is a more natural setup that both the spheres rotate freely due to the torques operating on the surface of these spheres from the fluid, because the spheres need not be co-rotating in the actual astronomical bodies. For instance, it is discussed whether the Earth's inner core differentially rotates with respect to the mantle in this decade [38, 39, 40]. However, most of the studies on thermal convection in rotating spherical shells performed so far assume that the inner and outer spheres co-rotate. This is possibly due to simplification of the configuration of the problem, although some MHD dynamo models permit differential rotation of the inner sphere [41, 42, 43, 44, 45]. Araki *et al.* [46] investigated the bifurcation structure of the axisymmetric steady thermal convection patterns in a spherical shell with the inner sphere differential rotation using the Newton method, but they fixed the rotation rate of the inner sphere.

Therefore, in this thesis, we construct a model of Boussinesq thermal convection in a rotating spherical shell allowing rotation of the inner and outer spheres, and investigate fundamental behaviour of convective solutions comparing with those in the co-rotating system.

In Chap. 2, we first evaluate torques on the inner and outer spheres induced by thermal convection in a co-rotating system in order to assess to what extent the convective motion changes the rotation rates of the spheres.

We use stable traveling wave solutions TW4s which bifurcate at critical points and propagate in the azimuthal direction (shown in Sec.1.2). We find that the direction of the torque on the inner sphere is prograde when the rotation rate is small, while it becomes retrograde when the rotation rate is large. We also find that the torque on the inner sphere can be large enough to change the angular velocity of the inner sphere significantly even in a period of rotation. At the same time, we also examine generation mechanisms of mean zonal flows excited by thermal convection using the numerical weakly nonlinear analyses proposed by Takehiro and Hayashi [10, 47], since shear stress of the mean zonal flows on the spheres induces the axial component of the torques. Weakly nonlinear analyses show that the nonlinear term in the energy equation is most effective to generate the global distribution of mean zonal flows, however, the azimuthal component of the nonlinear term in the Navier-Stokes equation becomes most important for generation of the torque on the inner sphere when the rotation rate is large.

In Chap. 3, we develop a model of Boussinesq thermal convection allowing the inner sphere rotation and investigate effects of the inner sphere rotation on a bifurcation structure and convection patterns. We use the Newton method and numerical eigenvalue calculations, and obtain a bifurcation diagram of the finite-amplitude traveling wave solutions TW4s, which bifurcate at critical points, have four-fold symmetry in the azimuthal direction and propagate in the azimuthal direction. These traveling wave solutions are stable in the region $R_c \leq R \lesssim 1.2 - 2R_c$ depending on the rotation rate, where R and R_c are the Rayleigh number and the critical value, respectively. The inner sphere rotates in the prograde direction due to the viscous torque of the fluid when the rotation rate is small while it rotates in the retrograde direction when the rotation rate is large. The stable region of these traveling wave solution TW4s is quantitatively similar to that in the co-rotating system, shown in Fig. 1.1. The structures of convective motions of these TW4 solutions, such as the radial component of velocity, are also quantitatively similar to those in the co-rotating system, but amplitude of mean zonal flows and propagating velocity of TW4s are effectively changed by the inner sphere rotation. This tendency can be explained that the nonlinear effect is small because the traveling wave solutions are stable only near the critical curve.

In Chap. 4, we extend the model of Boussinesq thermal convection to allow rotation of both the inner and outer spheres. We perform numerical time integrations in the range $4R_c \lesssim R \lesssim 5R_c$ at a moderately rotating case, and investigate the difference of the convective solutions, especially focusing on the emergence of the equatorially asymmetric convection patterns. In this parameter region, the pattern of the finite-amplitude convective solution transits from equatorial symmetric one to equatorial asymmetric one

as the Rayleigh number is increased. We find that the route of this transition in the system allowing rotation of both spheres is different from that in the co-rotating system: $\mathrm{QP}^{\mathrm{S}} \rightarrow \mathrm{QP}^{\mathrm{A}} \rightarrow \mathrm{C}^{\mathrm{A}}$ in the co-rotating system while $\mathrm{QP}^{\mathrm{S}} \rightarrow \mathrm{C}^{\mathrm{S}} \rightarrow \mathrm{C}^{\mathrm{A}}$ in the system allowing rotation of both spheres, as the Rayleigh number is increased, where QP^{S} is an equatorially symmetric quasi-periodic solution, QP^{A} an equatorially asymmetric quasi-periodic solution, C^{S} an equatorially symmetric chaotic solution, and C^{A} an equatorially asymmetric chaotic solution. The transition route in the system where only the inner sphere is permitted is exactly same as that in the system allowing rotation of both the spheres. Therefore, we conclude that the inner sphere rotation causes the different transition route from that in the co-rotating system.

Chapter 2

Torques on the inner and outer spheres induced by the Boussinesq thermal convection in a rotating spherical shell [1]

2.1 Introduction

There are many researches to investigate the Boussinesq thermal convection in rotating spherical shells, however, most of the ones performed so far assume that the inner and outer spheres co-rotate, that is, both spheres rotate with the same angular velocity. It is a more natural setup that both the spheres rotate freely due to the torques operating on the surface of these spheres from the fluid, because the spheres need not be co-rotating in the actual astronomical bodies. For instance, it is discussed whether the Earth's inner core differentially rotates with respect to the mantle in this decade [38, 39, 40]. Few researches on thermal convection have focused on the torques on the rotating spheres, although some MHD dynamo models permit differential rotation of the inner sphere [41, 42, 43, 44, 45].

Accordingly, in this chapter, we evaluate torques on the inner and outer spheres induced by thermal convection in a rotating spherical shell in order to assess to what extent the convective motion changes the rotation rates of the spheres. At the same time, we also examine generation mechanisms of mean zonal flows excited by thermal convection using the numerical weakly nonlinear analyses proposed by Takehiro and Hayashi [10, 47], since shear stress of the mean zonal flows on the spheres induces the axial component of

[1] Published in Kimura *et al.* (2012) [48].

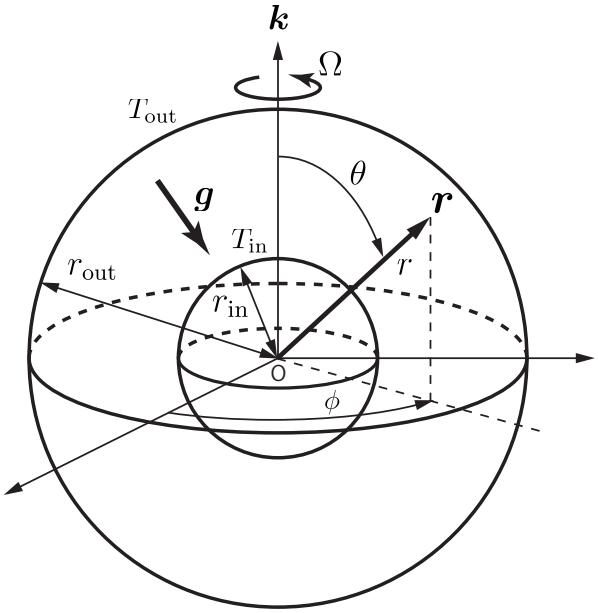

Figure 2.1: A schematic picture of the configuration of the Boussinesq thermal convection problem in co-rotating spheres.

the torques.

For the analyses, we use the finite-amplitude nonlinear traveling wave solutions investigated by Kimura *et al* [2], whose bifurcation structure is shown in Fig. 1.1. These solutions are obtained systematically by the Newton method at moderate rotation rates, and their stability and bifurcation diagram is established successfully. Since the solutions have four-fold symmetry in the azimuthal direction, we call them TW4s (Traveling Wave 4) hereafter.

In the following, the model, governing equations and numerical method are described in Sec.2.2. In Sec.2.3, we evaluate the torques on the inner and outer spheres induced by the stable TW4s and estimate the rate-of-change of the angular velocity of the inner sphere. In Sec.2.4, we perform the weakly nonlinear analyses numerically to investigate the generation mechanism of the mean zonal flows and the axial torque operating on the inner sphere. Conclusions and discussions are given in Sec.2.5.

2.2 Model and numerical method

Let us consider a Boussinesq fluid in a spherical shell whose radii of the inner and outer spheres are $r_{\rm in}$ and $r_{\rm out}$, respectively (Figure 2.1). Both spheres

are rotating with angular velocity Ω about the fixed unit vector $\boldsymbol{k}$. Since the fluid contains the uniform heat source H per unit mass, the temperature distribution of the basic conductive state $T_s(r)$ is

$$T_s(r) = -\frac{1}{2}\beta r^2 + T_0, \tag{2.1}$$

where $\beta \equiv H/(3\kappa C_p)$, κ is the thermal diffusivity, C_p the specific heat capacity, r the distance from the center of the spherical shell and T_0 a constant. We consider the self-gravitational field of homogeneous media whose density is ρ, that is,

$$\boldsymbol{g} = -\gamma \boldsymbol{r}, \tag{2.2}$$

where $\gamma \equiv 4\pi G\rho/3$ is a positive constant (G is the universal gravitational constant) and $\boldsymbol{r}$ the position vector with respect to the center of the shell.

We choose the thickness of the spherical shell $d \equiv r_{\text{out}} - r_{\text{in}}$ as the length scale, the viscous dissipation time d^2/ν as the time scale, and $\nu^2/(\gamma\alpha d^4)$ as the temperature scale, where ν is the kinematic viscosity and α the thermal expansion coefficient. The pressure is normalized with $(\rho\nu^2)/d^2$. The non-dimensional governing equations for the deviations from the conductive state (rest state) in the rotating frame of reference moving with the spherical shell are as follows:

$$\nabla \cdot \boldsymbol{u} = 0, \tag{2.3}$$

$$\frac{\partial \boldsymbol{u}}{\partial t} + (\boldsymbol{u}\cdot\nabla)\boldsymbol{u} + \tau \boldsymbol{k}\times\boldsymbol{u} = -\nabla\pi + \Theta\boldsymbol{r} + \nabla^2\boldsymbol{u}, \tag{2.4}$$

$$P\left(\frac{\partial \Theta}{\partial t} + (\boldsymbol{u}\cdot\nabla)\Theta\right) = R\boldsymbol{u}\cdot\boldsymbol{r} + \nabla^2\Theta, \tag{2.5}$$

where $\boldsymbol{u}$ is the non-dimensional velocity, π the non-dimensional pressure and Θ the non-dimensional temperature deviation from the basic state $T_s(r)$. The non-dimensional parameters in the above equations are

$$\tau = \sqrt{T} = \frac{2\Omega d^2}{\nu}, \quad P = \frac{\nu}{\kappa}, \quad R = \frac{\alpha\beta\gamma d^6}{\nu\kappa}, \tag{2.6}$$

where T is the Taylor number, P the Prandtl number and R the Rayleigh number.

Since the velocity field is solenoidal, it can be represented with the toroidal and poloidal potentials w and v as follows:

$$\boldsymbol{u} \equiv \nabla\times\{\nabla\times(\boldsymbol{r}v)\} + \nabla\times(\boldsymbol{r}w). \tag{2.7}$$

The governing equations for the potentials and Θ become

$$\left[\left(\Delta - \frac{\partial}{\partial t}\right)\hat{L}_2 + \tau(\boldsymbol{k}\times\boldsymbol{r})\cdot\nabla\right] w - \tau\hat{Q}v = \boldsymbol{r}\cdot\left[\nabla\times((\boldsymbol{u}\cdot\nabla)\boldsymbol{u})\right], \tag{2.8}$$

$$\left[\left(\Delta - \frac{\partial}{\partial t}\right)\hat{L}_2 + \tau(\boldsymbol{k}\times\boldsymbol{r})\cdot\nabla\right]\Delta v + \tau\hat{Q}w - \hat{L}_2\Theta = -\boldsymbol{r}\cdot\left[\nabla\times\nabla\times((\boldsymbol{u}\cdot\nabla)\boldsymbol{u})\right], \tag{2.9}$$

$$P\left(\frac{\partial\Theta}{\partial t} + (\boldsymbol{u}\cdot\nabla)\Theta\right) = R\hat{L}_2 v + \Delta\Theta, \tag{2.10}$$

where $\hat{L}_2$ and $\hat{Q}$ are the operators defined as

$$\hat{L}_2 = -\frac{1}{\sin^2\theta}\left[\sin\theta\frac{\partial}{\partial\theta}\left(\sin\theta\frac{\partial}{\partial\theta}\right) + \frac{\partial^2}{\partial\phi^2}\right], \tag{2.11}$$

$$\hat{Q} \equiv \boldsymbol{k}\cdot\nabla - \frac{1}{2}\left[\hat{L}_2(\boldsymbol{k}\cdot\nabla) + (\boldsymbol{k}\cdot\nabla)\hat{L}_2\right]. \tag{2.12}$$

Here, θ is the colatitude (zenith) and ϕ is the longitude (azimuth) with respect to the rotation axis. These governing equations are equivalent to those of Simitev and Busse [19] with $R_e = 0$.

We apply impermeable, no-slip, and fixed temperature conditions at the inner and outer spheres.

$$\boldsymbol{u} = \Theta = 0, \quad \text{at} \quad r = \frac{\eta}{1-\eta},\ \frac{1}{1-\eta}, \tag{2.13}$$

where $\eta = r_{\rm in}/r_{\rm out}$, is the ratio of the inner and outer radii of the shell. The boundary conditions for potentials are as follows:

$$v = \frac{\partial v}{\partial r} = w = 0, \quad \text{at} \quad r = \frac{\eta}{1-\eta},\ \frac{1}{1-\eta}. \tag{2.14}$$

We will fix the values of η and P as the standard value $\eta = 0.4$ and $P = 1$, while the rotation rate is varied in the range of $52 \le \tau \le 500$.

The Galerkin-spectral method is applied to the toroidal and poloidal potentials and the temperature disturbance. They are expanded with the spherical harmonics in the horizontal (azimuthal and zenith) directions, and with the combinations of Chebyshev polynomials which satisfy the boundary conditions in the radial direction. The truncation wavenumber of spherical harmonics L and the maximum degree of the Chebyshev polynomials N are both fixed to 16, while $(N, L) = (16, 21)$ or $(21, 16)$ are used in some calculations

to spot-check the results and the accuracy is confirmed to be less than 0.5%. The nonlinear terms are evaluated in the physical space and are converted back into the spectral space (the spectral transform method). The numbers of the grid points on the physical space are fixed to $(N_r, N_\theta, N_\phi) = (65, 32, 64)$ in order to eliminate the aliasing errors, where N_r, N_θ and N_ϕ are the number of grid points in the radial, zenith (colatitudinal) and azimuthal (longitudinal) directions, respectively. Note that the traveling wave solution propagates in the azimuthal direction, so denoting the propagating velocity is v_p, this solution becomes the stationary solution in the frame of reference moving with the azimuthal velocity v_p with respect to the rotating frame. Thus we transform the time t and longitude ϕ into $T \equiv t$ and $\Phi \equiv \phi - v_p t$, and seek the stationary solution in this moving frame of reference. However, one arbitrariness corresponding to the arbitrariness of the origin of the longitude Φ remains, so we lock the phase of the complex spectral coefficient whose absolute value is maximum among all the spectral coefficients in the critical state (actually we lock the phase as 0 [rad]). The detailed numerical method is described in the Appendices. Torques operating on the spheres are calculated for each stable TW4s, and the rate-of-change of angular velocity of the inner sphere is evaluated. After that, weakly nonlinear analyses are performed by using TW4s on the critical points to assess the generation mechanism of mean zonal flows and the axial torque on the inner sphere.

2.3 Torques operating on the inner sphere and its rotation

When $52 \leq \tau \leq 500$, TW4s bifurcate supercritically at the critical points and become unstable when the Rayleigh number is increased up to about 1.2 to 2 times the critical Rayleigh numbers. The bifurcation diagram of TW4s is shown in Fig. 1.1. Note that TW4s induce only the axial component of the torque on the inner sphere because of their equatorial symmetry. Moreover, since TW4s are stationary waves in the frame of reference moving with their propagation speed, the summation of the torques on the inner and outer spheres is equivalent to zero due to the conservation of the angular momentum. Therefore, we evaluate only the axial component of torque $N_{\rm in}$ operating on the inner sphere, which is calculated as,

$$N_{\rm in} = 2\pi r_{\rm in}^3 \int_0^\pi \left[\frac{\partial \langle u_\phi \rangle}{\partial r} \right]_{r=r_{\rm in}} \sin^2\theta d\theta, \tag{2.15}$$

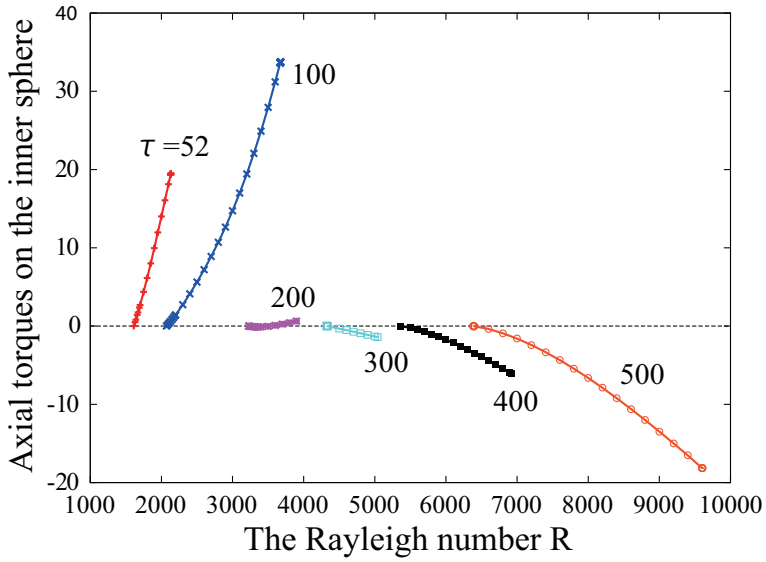

Figure 2.2: The axial component of torques operating on the inner sphere $N_{\rm in}$ induced by the stable TW4s for each τ.

where $\langle f \rangle(r, \theta)$ means the azimuthal (longitudinal or zonal) average defined as

$$\langle f \rangle(r, \theta) \equiv \frac{1}{2\pi} \int_0^{2\pi} f(r, \theta, \phi) d\phi. \tag{2.16}$$

Figure 2.2 shows $N_{\rm in}$ for each τ induced by the stable TW4s. This figure shows that when $\tau = 52$ and 100, $N_{\rm in}$ is positive, that is, the inner sphere tends to be rotated in the prograde direction, and is strengthened as the Rayleigh number is increased. However, when τ is increased to 200, $N_{\rm in}$ almost vanishes and the torque becomes quite weak. As τ is further increased, $N_{\rm in}$ becomes negative, that is, the inner sphere tends to be rotated in the retrograde direction, and is strengthened again as the Rayleigh number is increased.

Figure 2.3 shows the distributions of mean zonal flow $\langle u_\phi \rangle$ of the stable TW4s at slightly supercritical states $R = R_1$ and below the marginal stability states $R = R_2$. The detailed parameters are shown in Table 2.1. Note that since these mean zonal flows are generated by the nonlinear effects of TW4s, the torques at the critical states ($R = R_c$) are equivalently zero as seen in Fig. 2.2. From Fig. 2.3, we can find that the distributions of mean zonal flow at $R = R_1$ and $R = R_2$ are quite similar except for the difference of their amplitudes. When the rotation rate is small as $\tau = 52$ and 100 (Figs.

τ	R_c		R_1		R_2	R_c^{TW4}
52	1612.5026	(a)	1636.2	(A)	2100	2133
100	2070.3920	(b)	2100.8	(B)	3600	3675
200	3224.8090	(c)	3262.3	(C)	3800	3902
300	4324.7513	(d)	4373.3	(D)	5000	5044
400	5355.1777	(e)	5413.6	(E)	6900	6924
500	6386.6056	(f)	6453.9	(F)	9200	9590∗

Table 2.1: The values of the Rayleigh number of the panels in Fig. 2.3. R_c is the critical Rayleigh numbers, R_c^{TW4} is the marginal stability Rayleigh numbers of TW4s, R_1 is the typical Rayleigh numbers near the critical states ($R_1 \simeq 1.01R_c$), and R_2 is typical Rayleigh numbers slightly below the marginal states. Values labeled with asterisk appearing in cases $\tau = 500$ are calculated with the truncation wavenumbers $(N, L) = (21, 28)$. R_c and R_c^{TW4} have already been shown in Table 3 of Kimura *et al.* (2011) [2], but these values on this table are more accurate (nearly 0.1% or less).

2.3 (a), (b), (A) and (B)), the prograde zonal flows appear near the whole surface of the inner sphere. As the rotation rate is increased as $\tau = 200$ and 300, however, the strong retrograde zonal flows appear near the outer sphere around the equator and move inward (Figs. 2.3 (c), (d), (C) and (D)). Finally, the strong retrograde zonal flows attach to the equatorial region of the inner sphere (Figs. 2.3 (e), (f), (E) and (F)). Such transition of the distribution of mean zonal flows contributes to the transition of the direction of the torques on the inner sphere with increasing the rotation rate.

In order to examine the significance of the axial torques on the inner sphere evaluated above, let us calculate the rate-of-change of angular velocity of the inner sphere in a period of rotation. For this purpose, we have to define the inertial moment of the inner sphere. Here, we assume that density of the inner sphere is homogeneous and equivalent to that of fluid in the shell ρ. Then, the non-dimensional inertial moment of the inner sphere I_{in} can be calculated as

$$I_{\mathrm{in}} = \frac{8}{15}\pi \left(\frac{\eta}{1-\eta}\right)^5 \simeq 0.22, \tag{2.17}$$

where we choose ρd^5 as the scale of the inertial moment. Then, if the order of magnitude of the torque on the inner sphere is assumed to remain the same when the inner sphere rotates against the outer sphere, the rate-of-change of angular velocity of the inner sphere in a period of rotation is estimated as

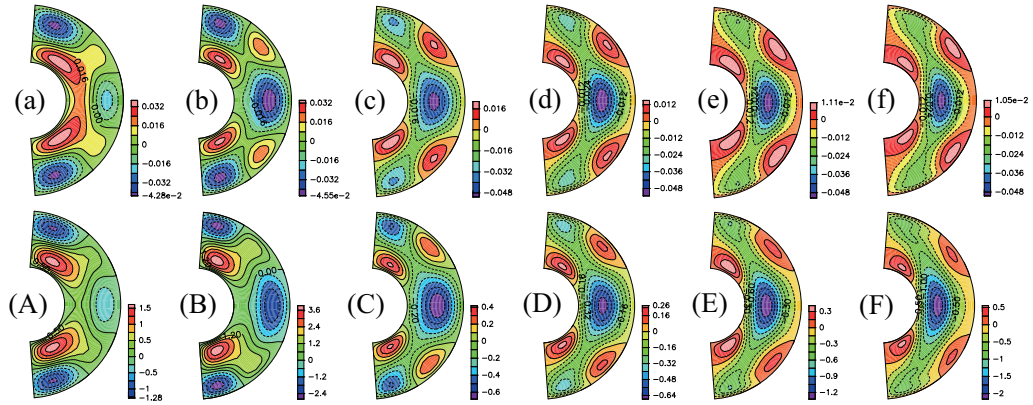

Figure 2.3: Distributions of mean zonal flow of the stable TW4s at each value of τ and the Rayleigh number shown in Table 2.1. The upper six panels show the zonal flows at slightly supercritical states $R = R_1 \simeq 1.01R_c$, while the lower six panels show zonal flows slightly below the marginally stable states $R = R_2$.

follows:

$$\frac{\Delta\Omega_{\rm in}}{\Omega} \sim \left(\frac{N_{\rm in}}{I_{\rm in}} \cdot \frac{2\pi}{\tau/2}\right) \Big/ \frac{\tau}{2} \simeq 0.11 \left(\frac{N_{\rm in}}{10}\right) \left(\frac{\tau}{100}\right)^{-2}. \tag{2.18}$$

Table 2.2 shows the maximum amplitude of the torque on the inner sphere $|N_{\rm in}|_{\rm max}$ and the maximum rate-of-change of the angular velocity of the inner sphere $|\Delta\Omega_{\rm in}/\Omega|_{\rm max}$ induced by the stable TW4s for each τ. When the rotation rate is small as $\tau = 52$ and 100, the rate-of-change of the angular velocity of the inner sphere becomes several tens percent. This means the torque on

τ	$\lvert N_{\rm in}\rvert_{\rm max}$	$\lvert\Delta\Omega_{\rm in}/\Omega\rvert_{\rm max}$
52	+19.5	82%
100	+33.8	39%
200	+0.64	0.18%
300	−1.42	0.18%
400	−6.08	0.43%
500	−18.2	0.83%

Table 2.2: The maximum amplitudes of the torque on the inner sphere $|N_{\rm in}|_{\rm max}$ and the maximum rate-of-change of the angular velocity of the inner sphere $|\Delta\Omega_{\rm in}/\Omega|_{\rm max}$ induced by the stable TW4s for each τ.

the inner sphere is sufficiently large enough to rotate the inner sphere. When the rotation rate is large as $\tau = 400$ and 500, the rate-of-change is less than 1 percent. However, it can be effective for changing the angular velocity of the inner sphere after 1 non-dimensional time (the viscous diffusion time scale), because both spheres rotate $\tau/(4\pi)$ times in 1 non-dimensional time.

2.4 Generation mechanism of mean zonal flows and torques

2.4.1 Results of weakly nonlinear analyses

In this section, we investigate the generation mechanism of mean zonal flows and the axial torques on the inner sphere through the numerical weakly nonlinear analyses using the critical modes [10, 47]. It is interesting to examine the mean zonal flow generation mechanisms because their characteristics are related to several aspects of phenomena in the system. As mentioned in the previous section, they are directly related to the axial component of the torque and determine its direction. Kimura *et al.* [2] shows that advection of mean zonal flows presumably affects to the propagation direction of TW4s when the rotation rate is large ($\tau \geq 340$).

Following the procedure of Takehiro and Hayashi [10, 47], we expand the dependent variables $\boldsymbol{u}$, T, π and the Rayleigh number R with the amplitude ϵ around the critical state, that is,

$$\boldsymbol{u}(\boldsymbol{r}, t) = \epsilon \boldsymbol{u}^{(1)} + \epsilon^2 \boldsymbol{u}^{(2)} + \cdots , \tag{2.19}$$

$$T(\boldsymbol{r}, t) = T_s(r) + \epsilon \Theta^{(1)} + \epsilon^2 \Theta^{(2)} + \cdots , \tag{2.20}$$

$$\pi(\boldsymbol{r}, t) = \pi_s(r) + \epsilon \pi^{(1)} + \epsilon^2 \pi^{(2)} + \cdots , \tag{2.21}$$

$$R = R_c + \epsilon R^{(1)} + \epsilon^2 R^{(2)} + \cdots . \tag{2.22}$$

The axial component of torque on the inner sphere N_{in} can also be expanded as

$$N_{\mathrm{in}} = \epsilon N_{\mathrm{in}}^{(1)} + \epsilon^2 N_{\mathrm{in}}^{(2)} + \cdots , \tag{2.23}$$

where

$$N_{\mathrm{in}}^{(j)} = 2\pi r_{\mathrm{in}}^3 \int_0^{\pi} \left[\frac{\partial \left\langle u_\phi^{(j)} \right\rangle}{\partial r} \right]_{r=r_{\mathrm{in}}} \sin^2 \theta d\theta, \tag{2.24}$$

here j is an any positive integer. First, we obtain the critical Rayleigh numbers and critical modes from the $O(\epsilon)$ equations of the governing equations (2.3) –(2.5), that is, the linearized equations around the conductive state. Assuming the solution of the form as $e^{\sigma t}$ and solving the eigenvalue problem with respect to the growth rate σ repeatedly, we can obtain the critical Rayleigh numbers and critical modes. Note that in the parameter ranges of our calculations ($\eta = 0.4$, $P = 1$ and $52 \leq \tau \leq 860$), the critical azimuthal wavenumber m_c is 4, not zero. Therefore $\left\langle u_\phi^{(1)} \right\rangle$ vanishes due to sinusoidal oscillation of $u_\phi^{(1)}$ in the azimuthal direction. Then $N_{\text{in}}^{(1)}$ must be zero. Secondly, we find the second order zonal mean steady solutions induced by the critical modes by solving $O(\epsilon^2)$ equations. Taking the zonal average $\langle \cdot \rangle$ and dropping the time derivative term in the $O(\epsilon^2)$ equations, we obtain the following equations:

$$\frac{1}{r^2}\frac{\partial}{\partial r}\left(r^2 \left\langle u_r^{(2)} \right\rangle\right) + \frac{1}{r\sin\theta}\frac{\partial}{\partial \theta}\left(\sin\theta \left\langle u_\theta^{(2)} \right\rangle\right) = 0, \tag{2.25}$$

$$\left\langle \left[(\boldsymbol{u}^{(1)} \cdot \nabla)\boldsymbol{u}^{(1)}\right]_r \right\rangle - \tau \left\langle u_\phi^{(2)} \right\rangle \sin\theta = -\frac{\partial \left\langle \pi^{(2)} \right\rangle}{\partial r} + \left\langle \Theta^{(2)} \right\rangle r + \left[\nabla^2 \left\langle \boldsymbol{u}^{(2)} \right\rangle\right]_r, \tag{2.26}$$

$$\left\langle \left[(\boldsymbol{u}^{(1)} \cdot \nabla)\boldsymbol{u}^{(1)}\right]_\theta \right\rangle - \tau \left\langle u_\phi^{(2)} \right\rangle \cos\theta = -\frac{1}{r}\frac{\partial \left\langle \pi^{(2)} \right\rangle}{\partial \theta} + \left[\nabla^2 \left\langle \boldsymbol{u}^{(2)} \right\rangle\right]_\theta, \tag{2.27}$$

$$\left\langle \left[(\boldsymbol{u}^{(1)} \cdot \nabla)\boldsymbol{u}^{(1)}\right]_\phi \right\rangle + \tau \left(\left\langle u_\theta^{(2)} \right\rangle \cos\theta + \left\langle u_r^{(2)} \right\rangle \sin\theta\right) = \left[\nabla^2 \left\langle \boldsymbol{u}^{(2)} \right\rangle\right]_\phi, \tag{2.28}$$

$$P \left\langle (\boldsymbol{u}^{(1)} \cdot \nabla)\Theta^{(1)} \right\rangle = R_c \, r \left\langle u_r^{(2)} \right\rangle + \nabla^2 \left\langle \Theta^{(2)} \right\rangle, \tag{2.29}$$

where (r, θ, ϕ) mean the radius, zenith (colatitude) and azimuth (longitude) of the spherical coordinates. The above equations can be rewritten as

$$\boldsymbol{0} = \hat{L} \left\langle \boldsymbol{x}^{(2)} \right\rangle + \left\langle \boldsymbol{n}(\boldsymbol{x}^{(1)}) \right\rangle, \tag{2.30}$$

where $\boldsymbol{x}^{(1)}$ and $\boldsymbol{x}^{(2)}$ are the vectors of dependent variables of $O(\epsilon)$ and $O(\epsilon^2)$ respectively, $\hat{L}$ a linear operator and $\boldsymbol{n}$ a nonlinear term. Since we have already obtained the vector $\boldsymbol{x}^{(1)}$ as the critical mode, we can obtain the vector $\left\langle \boldsymbol{x}^{(2)} \right\rangle$ by solving the above linear equations.

Four nonlinear terms in eqs. (2.26) –(2.29) can be classified into three groups as follows:

(i) the azimuthal (longitudinal) component of the nonlinear term in the Navier-Stokes equation (the nonlinear term in eq. (2.28)),

(ii) the zenith (colatitudinal) and radial components of the nonlinear term of the Navier-Stokes equation (the nonlinear terms in eqs. (2.26) and (2.27)),

(iii) the nonlinear term in the energy equation (2.29).

Each nonlinear term generates the mean zonal flow through the following mechanism:

(i): the meridional transfer of the angular momentum by the Reynolds stress directly generates the mean zonal flow,

(ii): the Coriolis force against the mean meridional flow induced by the Reynolds stress generates the mean zonal flow,

(iii): the Coriolis force against the mean meridional flow induced by the zenith (colatitudinal) gradient of the secondary mean temperature disturbance, which is caused by the convective heat transfer, generates the mean zonal flow.

Considering the conservation of the angular momentum, the mechanism (i) can be understood more easily. Multiplying $r\sin\theta$ to eq. (2.28) and taking the zonal average, we can obtain

$$\nabla\cdot\left[\frac{\tau}{2}r^2\sin^2\theta\left\langle\boldsymbol{u}^{(2)}\right\rangle+r\sin\theta\left\langle u_\phi^{(1)}\boldsymbol{u}^{(1)}\right\rangle\right]=r\sin\theta\left\langle\left[\nabla^2\boldsymbol{u}^{(2)}\right]_\phi\right\rangle. \tag{2.31}$$

The first term in the left hand side means the advection flux of the absolute angular momentum due to the rotation of the shell and the second term means the Reynolds stress induced by the critical mode. The mechanism (iii) can be understood more easily through the curl of eqs. (2.26) and (2.27), that is,

$$-\tau(\boldsymbol{k}\cdot\nabla)\left\langle u_\phi^{(2)}\right\rangle=-\frac{\partial\left\langle\Theta^{(2)}\right\rangle}{\partial\theta}+\left[\nabla\times\nabla^2\left\langle\boldsymbol{u}^{(2)}\right\rangle\right]_\phi. \tag{2.32}$$

Here, we have neglected the nonlinear terms in eqs. (2.26) and (2.27). When the rotation rate is small, mean meridional flow is induced by the latitudinal gradient of the secondary mean temperature disturbance through the viscous term in the above equation (2.32), and the mean zonal flow is generated due to the Coriolis force against this mean meridional flow. On the other hand, when the rotation rate is large enough, the latitudinal gradient of

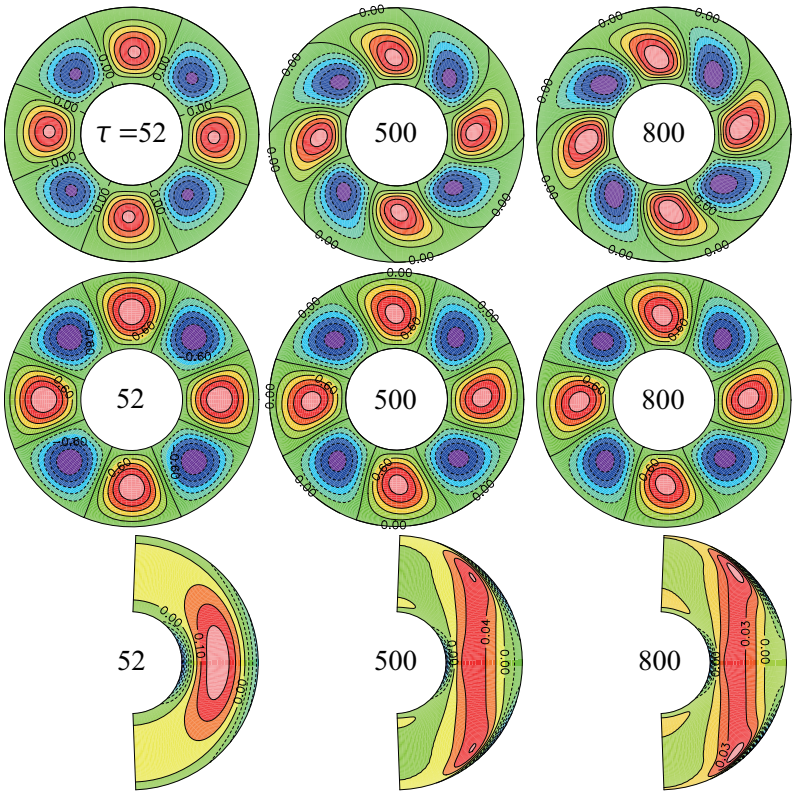

Figure 2.4: The patterns of the critical modes at $\tau = 52$, 500 and 800. The upper three panels show the distributions of the radial velocity $u_r^{(1)}$ in the equatorial plane ($\theta = 90°$), the middle three panels show the distributions of the temperature disturbance $\Theta^{(1)}$ in the equatorial plane, while the lower three panels show the axial component of vorticity $\omega_z = \boldsymbol{k} \cdot (\nabla \times \boldsymbol{u}^{(1)})$ in a meridional plane.

the secondary mean temperature disturbance generates the mean zonal flow directly through thermal wind balance, that is, the balance between the term in the left hand side and the first term in the right hand side in the equation (2.32). By comparing the amplitudes of the mean zonal flow $\left\langle u_\phi^{(2)} \right\rangle$ generated by these three groups of the nonlinear terms, we can quantitatively diagnose the principal nonlinear effect on the generation of the mean zonal flow.

Figure 2.4 shows the distributions of the radial velocity in the equatorial plane and the axial component of vorticity in a meridional plane of the critical modes at $\tau = 52$, 500 and 800. We find that even $\tau = 500$ the convection cell already becomes the spiralling columnar shape, which is a typical characteristic of the convection cell in rapidly rotating cases [13].

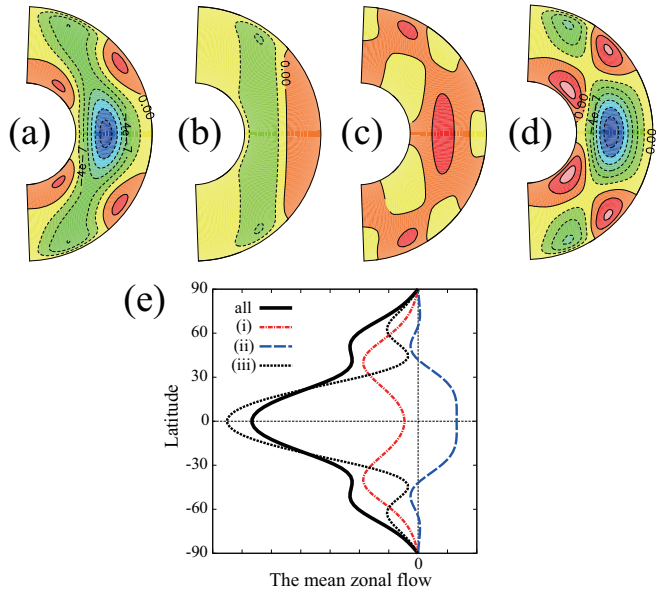

Figure 2.5: The results of the weakly nonlinear analyses at $\tau = 500$. (a) The mean zonal flow $\left\langle u_\phi^{(2)} \right\rangle$ generated by the all nonlinear terms (i), (ii) and (iii). (b) The mean zonal flow generated only by the nonlinear term (i). (c) The mean zonal flow generated only by the nonlinear terms (ii). (d) The mean zonal flow generated only by the nonlinear term (iii). (e) The latitudinal (zenith) distributions of the mean zonal flows at $r = (r_{\rm in} + r_{\rm out})/2$ generated by the all nonlinear terms and by each group of the nonlinear terms.

Figure 2.5 shows the mean zonal flow $\left\langle u_\phi^{(2)} \right\rangle$ generated by all the nonlinear terms (Fig. 2.5(a)), and that only by one group of the nonlinear terms (Figs. 2.5 (b), (c) and (d)). Comparison of the latitudinal (zenith) distributions of the mean zonal flow at $r = (r_{\rm in} + r_{\rm out})/2$ is shown in (e). From Fig. 2.5(e), we find that the amplitude of the mean zonal flow generated by the nonlinear term (iii) is several times larger than those generated by (i) and (ii) around the equator. This means that the nonlinear effect (iii) is the principal generation mechanism of the strong retrograde zonal flow in the middle of the shell around the equator when $\tau = 500$.

Figures 2.6 and 2.7 compare the meridional distribution of the mean zonal flows generated by all the nonlinear terms and by each group of nonlinear terms at $\tau = 52$ and 800, respectively. From these figures, we can find that the amplitude of the mean zonal flow generated by the nonlinear effect (iii) is larger than those generated by (i) and (ii) at both $\tau = 52$ and 800. This

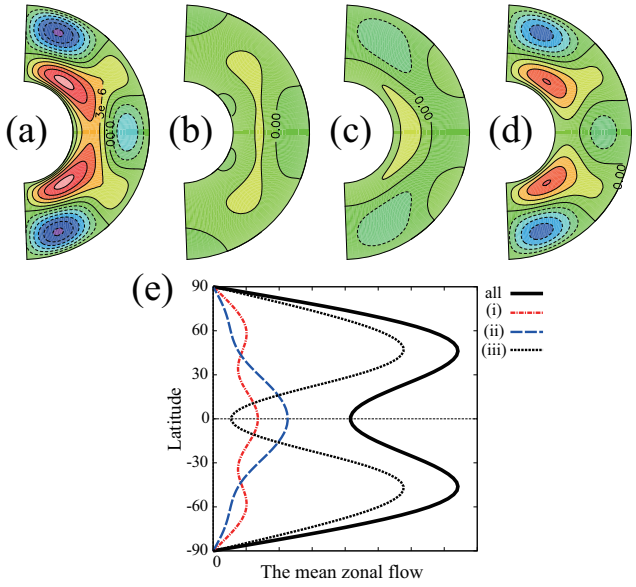

Figure 2.6: Same as Fig. 2.5 but for $\tau = 52$. Note that (e) shows the latitudinal (zenith) distribution at $r = r_{\rm in} + d/4 = \eta/(1-\eta) + 0.25$.

tendency can be observed at $\tau = 860$. Therefore, we can conclude that the nonlinear effect (iii) is the principal mechanism on generation of the mean zonal flow in $52 \leq \tau \leq 860$.

Here we concretely discuss the geometric structures of the zonal flows, which are shown in Figs. 2.5, 2.6 and 2.7, through the most important mechanism (iii) in terms of those of $\boldsymbol{u}^{(1)}$ and $\Theta^{(1)}$, shown in Fig. 2.4, especially at $\tau = 500$.

The geometric structures of the zonal flows, shown in Figs. 2.5, 2.6 and 2.7 can be explained more precisely in terms of those of $\boldsymbol{u}^{(1)}$, $\Theta^{(1)}$ and $\left\langle \Theta^{(2)} \right\rangle$ as below. Briefly speaking, the latitudinal gradient of $\left\langle \Theta^{(2)} \right\rangle$ induced by $\boldsymbol{u}^{(1)}$ and $\Theta^{(1)}$ generates mean zonal flows through the thermal wind balance or the Coriolis force acting on the secondary mean meridional circulations.

Figure 2.8 shows the results of the weakly nonlinear analyses at $\tau = 52$, 500 and 800. The upper three panels show the mean zonal values of the nonlinear term of the energy equation (iii) $P \left\langle (\boldsymbol{u}^{(1)} \cdot \nabla)\Theta^{(1)} \right\rangle$. The middle three panels show the mean meridional circulation $\left\langle u_r^{(2)} \right\rangle$ and $\left\langle u_\theta^{(2)} \right\rangle$ generated by the nonlinear term (iii). The lower three panels show the mean zonal flows generated by the nonlinear term (iii).

First, the secondary mean temperature disturbance $\left\langle \Theta^{(2)} \right\rangle$ is induced by the thermal flux convergence $-\left\langle (\boldsymbol{u}^{(1)} \cdot \nabla)\Theta^{(1)} \right\rangle = -\left\langle \nabla \cdot (\boldsymbol{u}^{(1)}\Theta^{(1)}) \right\rangle$, through

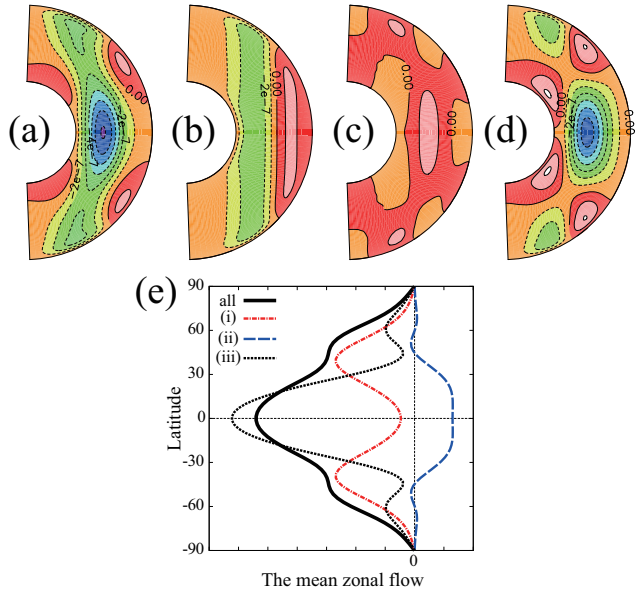

Figure 2.7: Same as Fig. 2.5 but for $\tau = 800$.

the energy equation (2.29). The thermal flux diverges near the inner sphere on the equatorial plane while it converges near the outer sphere because $u_r^{(1)}\Theta^{(1)}$ is positive for almost all region on the equatorial plane and is maximum in the middle of the spherical shell (Fig. 2.4). This flux divergence, balancing mainly with the diffusion term $\nabla^2 \left\langle \Theta^{(2)} \right\rangle$, induces $\left\langle \Theta^{(2)} \right\rangle$. Actually, as is observed in Fig. 2.8, each pattern of the thermal flux divergence is similar to that of $\left\langle \Theta^{(2)} \right\rangle$ except for its sign.

Second, the mean meridional circulation $\left(\left\langle u_r^{(2)} \right\rangle, \left\langle u_\theta^{(2)} \right\rangle \right)$ is driven by the latitudinal gradient of the secondary temperature disturbance $\partial \left\langle \Theta^{(2)} \right\rangle / \partial\theta$, through the azimuthal component of the curl of Navier-Stokes equation (2.32). When $\tau = 500$ and 800, the mean zonal flow pattern can be explained by the thermal wind balance,

$$-\tau(\boldsymbol{k} \cdot \nabla) \left\langle u_\phi^{(2)} \right\rangle = -\frac{\partial \left\langle \Theta^{(2)} \right\rangle}{\partial\theta},$$

since the rotation rate of the system is sufficiently large so that the Coriolis term surmounts over the viscous term. For example, $\partial \left\langle \Theta^{(2)} \right\rangle / \partial\theta$ in the outer layer produces positive shear in the direction of the rotating axis $(\boldsymbol{k} \cdot \nabla) \left\langle u_\phi^{(2)} \right\rangle$, causing that strong retrograde zonal flow around the equator and prograde zonal flow near the outer sphere in the mid-latitudes. On the other

τ	All	(i)	(ii)	(iii)
52	+1	+0.01	+0.37	+0.62
500	−1	−4.20	−1.16	+4.36
800	−1	−2.63	−0.67	+2.30

Table 2.3: The ratio of contribution of each group of nonlinear terms to the axial component of the torque on the inner sphere. These are normalized with the amplitude of the total torque (described as "All" in this table). Note that the sign of the values denotes the direction of the torque.

hand, when $\tau = 52$, the mean zonal flow is generated by the Coriolis force acting on the mean meridional circulations $\nabla \times \nabla^2 \left\langle \boldsymbol{u}^{(2)} \right\rangle$, which is induced through the balance

$$0 = -\frac{\partial \left\langle \Theta^{(2)} \right\rangle}{\partial \theta} + \left[\nabla \times \nabla^2 \left\langle \boldsymbol{u}^{(2)} \right\rangle \right]_\phi .$$

The mean meridional circulations in the polar region is prominent in the left middle panel in Fig. 2.8, which is caused by the temperature differences between the warm polar regions and cold mid-latitude regions in the inner half layer. The Coriolis force acts on these mean meridional circulations and induces the mean zonal flows in the polar regions. The strong poleward flows along the inner sphere generate the strong prograde mean zonal flow in the inner parts of the polar regions, while inverse flows along the outer sphere generate the retrograde mean zonal flow in the outer parts of the polar regions.

Figure 2.9 shows the axial component of torque operating on the inner sphere generated by each group of nonlinear terms at $\tau = 52$, 500 and 800, respectively. Table 2.3 shows the ratio of contribution of each group of the nonlinear terms to the axial component of the torque on the inner sphere. We find that when $\tau = 52$, contribution of the nonlinear term (iii) almost determines the distribution of the axial torque. However, when $\tau = 500$ and 800, contribution of the nonlinear term (i) is most effective, and determines the direction of the axial torque.

2.4.2 The validity of the weakly nonlinear analyses at supercritical regime

In this subsection we confirm the validity of the weakly nonlinear analyses at supercritical regime where the TW4 solutions are stable. We determine

the value of ϵ from the amplitude of $m = 4$ components of the TW4 solution and the critical mode, and compare u_ϕ^{TW4} and $\epsilon^2 u_\phi^{(2)}$.

Figure 2.10 compares the zonal flow profiles of TW4 with those obtained by the weakly nonlinear analyses at $\tau = 500$, $R = 6453.9 (\simeq 1.01 R_c)$ and $\tau = 500$, $R = 9200 (\simeq 1.44 R_c)$. It is shown that these profiles are in good agreement both in the case of $R = 6453.9$ and $R = 9200$. The difference of the minimum values of zonal flows is about 1.5% at $R = 6453.9$ ($\min(u_\phi^{\mathrm{TW4}}) = -5.03 \times 10^{-2}$ while $\min(\epsilon^2 u_\phi^{(2)}) = -4.95 \times 10^{-2}$) and is about 17% at $R = 9200$ ($\min(u_\phi^{\mathrm{TW4}}) = -2.16$ while $\min(\epsilon^2 u_\phi^{(2)}) = -2.52$). Therefore, the perturbation solution is valid even in the finite amplitude supercritical regime.

We also evaluate the torques on inner sphere by comparing the weakly nonlinear analyses $\epsilon^2 N_{\mathrm{in}}^{(2)}$ with the torques of the TW4s $N_{\mathrm{in}}^{\mathrm{TW4}}$. When $\tau = 500$ and $R = 6453.9$, $N_{\mathrm{in}}^{\mathrm{TW4}} = -9.78 \times 10^{-2}$ and $\epsilon^2 N_{\mathrm{in}}^{(2)} = -8.49 \times 10^{-2}$. The difference of these values is about 13%. When $\tau = 500$ and $R = 9200$, $N_{\mathrm{in}}^{\mathrm{TW4}} = -15.0$ and $\epsilon^2 N_{\mathrm{in}}^{(2)} = -4.33$. The difference of these values is about 70%. The differences of the values of the torque calculated with the weakly nonlinear analyses from those of TW4 are relatively large compared with the difference of the minimum values of the mean zonal flow. This is due to differences of the radial derivative of the mean zonal flow at the inner sphere although the gross structures of mean zonal flows are sufficiently described by the weakly nonlinear analysis (see Figs. 2.10 (c) and (f)).

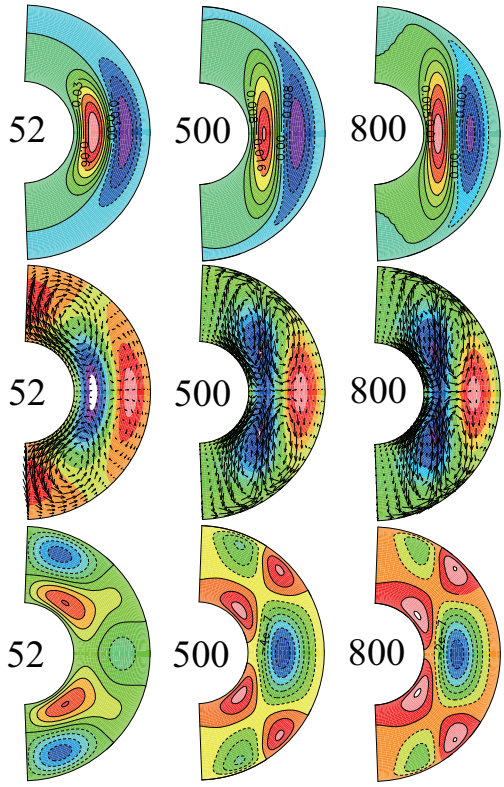

Figure 2.8: The results of the weakly nonlinear analyses at $\tau = 52$, 500 and 800. The upper three panels show the nonlinear term of the energy equation (iii) $P\ \left\langle (\boldsymbol{u}^{(1)} \cdot \nabla)\Theta^{(1)} \right\rangle$. The middle three panels show the mean meridional circulation $\left\langle u_r^{(2)} \right\rangle$ and $\left\langle u_\theta^{(2)} \right\rangle$ (arrows) and zonal mean temperature $\left\langle \Theta^{(2)} \right\rangle$ (tone) generated by the nonlinear term (iii). The lower three panels show the mean zonal flows generated by the nonlinear term (iii), which are same as the panels (d) in Figs. 2.5, 2.6 and 2.7.

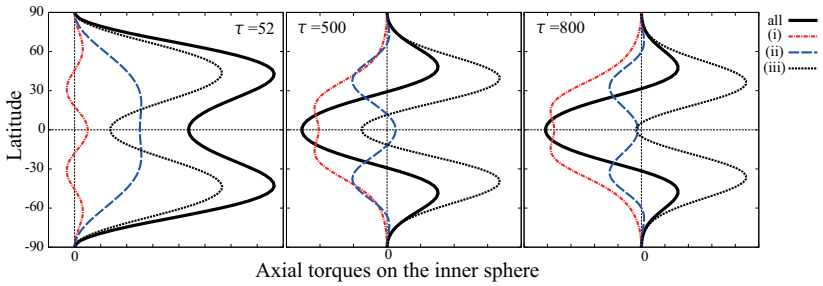

Figure 2.9: The axial component of torque operating on the inner sphere generated by each group of nonlinear terms at $\tau = 52$ (left), 500 (middle) and 800 (right).

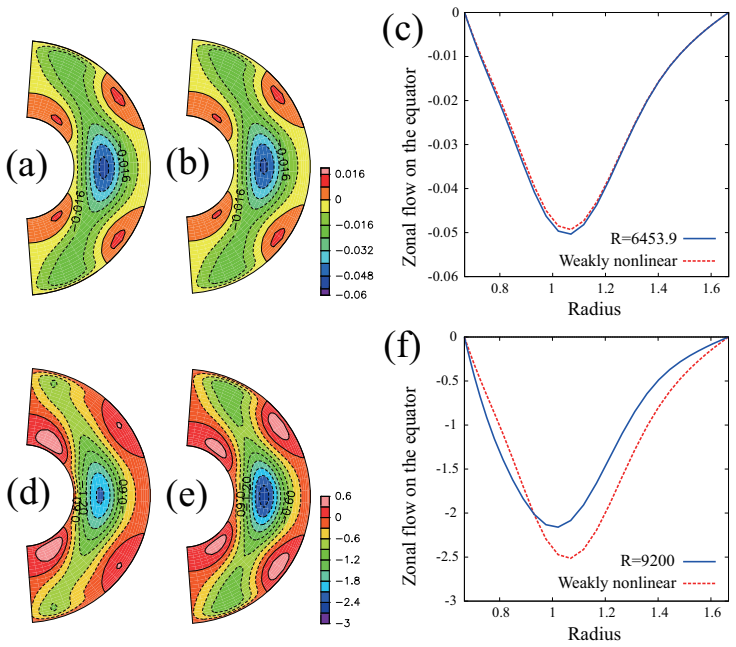

Figure 2.10: Comparison of the zonal flow profiles of TW4 with those obtained by weakly nonlinear analyses. The upper and lower panels show the cases with $\tau = 500$, $R = 6453.9(\simeq 1.01R_c)$ and and $\tau = 500$, $R = 9200(\simeq 1.44R_c)$, respectively. (a) and (d): $\left\langle u_\phi^{\mathrm{TW4}} \right\rangle$. (b) and (e): $\epsilon^2 \left\langle u_\phi^{(2)} \right\rangle$. (c) and (f): Comparison of zonal flow profiles at the equator. Blue solid and red dashed curves denote $\left\langle u_\phi^{\mathrm{TW4}} \right\rangle$ and $\epsilon^2 \left\langle u_\phi^{(2)} \right\rangle$, respectively. (a) and (d) are same as (f) and (F) in Fig. 2.3, respectively.

2.5 Conclusion and discussion

We have investigated the directions and amplitudes of torques on the inner and outer spheres induced by the stable finite-amplitude traveling wave solutions (TW4s) which bifurcate supercritically at the critical points under the impermeable, no-slip and fixed-temperature boundary conditions for the ratio of inner and outer radii of the shell $\eta = 0.4$ and the Prandtl number $P = 1$. Due to the equatorial symmetry of TW4 patterns, only the axial component of torques is induced. Moreover, since TW4 is a stationary solution in the frame of reference moving with the propagating velocity of TW4, summation of torques on the inner and outer spheres vanishes due to the conservation of angular momentum. Then the axial torque on the outer sphere has the same amplitude as that on the inner sphere, but has the opposite signature.

When the rotation rate is small as $\tau = 52$ and 100, the axial torque tends to rotate the inner sphere in the prograde direction, and stable TW4s can generate so strong axial torque that can change the angular velocity of the inner sphere significantly even in a period of rotation. When the rotation rate is increased as $\tau \simeq 200$, the axial torque induced by stable TW4s becomes very weak even increasing the Rayleigh number. However, as the rotation rate is further increased, the axial torque tends to rotate the inner sphere in the retrograde direction, and its amplitude is large enough to change the angular velocity of the inner sphere significantly after the viscous diffusion time scale. The transition of the direction of torque on the inner sphere is caused by the transition of the structure of the mean zonal flows of TW4s.

In order to find the generation mechanism of the mean zonal flows, the weakly nonlinear analyses are performed. By splitting the nonlinear terms into three groups (i), (ii) and (iii) defined in Sec. 2.4, calculating the secondary mean zonal flow induced by each nonlinear effect, the principal generation mechanism of mean zonal flows is determined quantitatively. It is revealed that the nonlinear term of the energy equation $P\left\langle \left(\boldsymbol{u}^{(1)} \cdot \nabla\right) \Theta^{(1)} \right\rangle$ (iii) most effectively contributes to the gross distribution of mean zonal flows compared to the other nonlinear terms (i) and (ii) when $52 \leq \tau \leq 860$ where the critical azimuthal wavenumber $m_c = 4$. Especially, contribution of the nonlinear term (iii) to the strong retrograde zonal flow at the middle on the equatorial plane in moderately rotating cases ($\tau \geq 300$) is several times larger than the other nonlinear terms (i) and (ii).

However, relative strength of contributions of these three groups of nonlinear terms to the axial torque on the inner sphere is somewhat different. When the rotation rate is small, the nonlinear term (iii) contributes to the prograde torque most effectively, while when the rotation rate is large, the

nonlinear term (i) contributes to the retrograde torque most effectively. The reason for this difference is that the axial torque on the inner sphere is not related to the mean zonal flow distribution inside the shell, but is induced by its shear stress on the inner sphere.

Takehiro and Hayashi [10, 47] show that when $\eta = 0.4$ and $P = 1$, the most effective mechanism on generating the mean zonal flow on the outer sphere is the nonlinear term (i), which seems to be inconsistent with our study. This difference may be due to the dynamical boundary condition. They use the free-slip boundary condition, while the no-slip boundary condition is adopted in the present study. When the Prandtl number is $O(1)$, the relative contributions of these three nonlinear effects are comparable and seem to be sensitive to the dynamical boundary conditions. At the moment, we cannot find the reason why the dynamical nonlinear effects are weakened when the no-slip boundary condition is adopted. Further detailed analyses are needed to solve this problem.

We have confirmed the validity of the weakly nonlinear analyses in the supercritical regime where the TW4 solutions are stable. Not only near the critical point but also near the marginal point of TW4 solutions, the result of weakly nonlinear analyses and TW4 solutions are in good agreement. Therefore we conclude that not only in the slightly supercritical regime but also in the finite amplitude supercritical regime the nonlinear term (iii) contributes to generate the mean zonal flow more effectively than the other nonlinear terms.

Chapter 3

Stability and a bifurcation diagram of Boussinesq thermal convection in a moderately rotating spherical shell allowing rotation of the inner sphere

3.1 Introduction

In the previous chapter, we evaluated torques on the inner and outer spheres induced by the stable traveling wave solutions TW4s, which bifurcate at critical points and propagate in the azimuthal direction (shown in Sec.1.2), in a co-rotating system. We found that the torque on the inner sphere can be large enough to change the angular velocity of the inner sphere.

Then, in this chapter, based on the result of Kimura *et al.*(2011) [2], we investigate effects of the inner sphere rotation on the bifurcation structure and the convection patterns. Almost previous studies of the Boussinesq thermal convection in rotating spheres and spherical shells assume the inner and outer spheres co-rotate, possibly due to simplification of the configuration of the problem. Araki *et al.*[46] investigated the bifurcation structure of the axisymmetric steady thermal convection patterns in a spherical shell with the inner sphere differential rotation using the Newton method, however, they fixed the rotation rate of inner sphere. There are some magnetohydrodynamic (MHD) dynamo models which permit the axial differential rotation of the inner sphere [41, 42, 43, 44, 45], but bifurcation structure in the MHD system has not been studied yet.

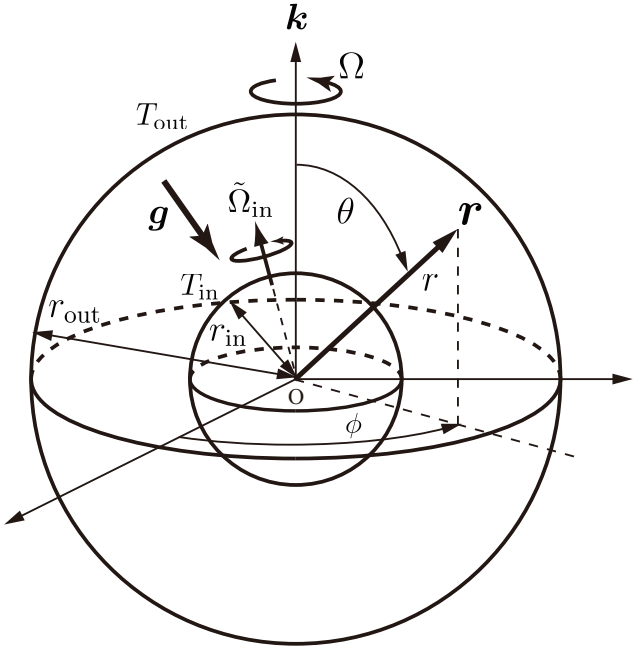

Figure 3.1: A schematic picture of the configuration of the Boussinesq thermal convection problem allowing the rotation of the inner sphere.

The model, governing equations and numerical methods are described in Sec. 3.2. In Sec. 3.3, we show the bifurcation diagram of the nonlinear traveling wave solutions which bifurcate at the critical points under the assumption of freely rotating inner sphere. The structures of these convective motions and mean zonal flow patterns are compared with those in the co-rotating system where both the inner and outer spheres rotate with the same angular velocity. The conclusions and discussions are described in Sec. 3.4.

3.2 Model and numerical method

Let us consider a Boussinesq fluid in a spherical shell whose radii of the inner and outer spheres are $r_{\rm in}$ and $r_{\rm out}$, respectively, shown in Fig. 3.1. This system is same as that in Sec. 2.2 except for the inner sphere rotation. The inner sphere is rotating with $\tilde{\boldsymbol{\Omega}}_{\rm in}$ in the rotating frame of reference with constant angular velocity $\Omega\boldsymbol{k}$. This means that the inner sphere is rotating with $\tilde{\boldsymbol{\Omega}}_{\rm in} + \Omega\boldsymbol{k}$ in the inertial frame of reference.

We choose the same scales introduced in Sec. 2.2. The inertial moment

of the inner sphere is normalized with ρd^5. The non-dimensional governing equations for the deviations from the state of rest in the rotating frame of reference moving with the constant angular velocity $\Omega \boldsymbol{k}$ are as follows:

$$\nabla \cdot \boldsymbol{U} = 0, \tag{3.1}$$

$$\frac{\partial \boldsymbol{U}}{\partial t} + (\boldsymbol{U} \cdot \nabla)\boldsymbol{U} + \tau \boldsymbol{k} \times \boldsymbol{U} = -\nabla \pi + \Theta \boldsymbol{r} + \Delta \boldsymbol{U}, \tag{3.2}$$

$$P\left(\frac{\partial \Theta}{\partial t} + (\boldsymbol{U} \cdot \nabla)\Theta\right) = R\, \boldsymbol{U} \cdot \boldsymbol{r} + \nabla^2 \Theta, \tag{3.3}$$

where $\boldsymbol{U}$ is the non-dimensional velocity and Θ is the non-dimensional temperature deviation from the basic state $T_s(r)$ (2.1). The equation of motion of the inner sphere is

$$I_{\mathrm{in}} \frac{d\tilde{\boldsymbol{\Omega}}_{\mathrm{in}}}{dt} = \boldsymbol{N}_{\mathrm{in}}(\boldsymbol{U}), \tag{3.4}$$

where I_{in} is the non-dimensional inertial moment of the inner sphere and $\boldsymbol{N}_{\mathrm{in}}$ is the non-dimensional torque operating the inner sphere. The axial component of this torque $\boldsymbol{k} \cdot \boldsymbol{N}_{\mathrm{in}} = N_{\mathrm{in},z}$ can be written as

$$N_{\mathrm{in},z} = 2\pi r_{\mathrm{in}}^3 \int_0^\pi \left[\frac{\partial \langle U_\phi \rangle}{\partial r} - \frac{\langle U_\phi \rangle}{r}\right]_{r=r_{\mathrm{in}}} \sin^2\theta d\theta, \tag{3.5}$$

where U_ϕ is the azimuthal component of velocity and $\langle f \rangle(r, \theta)$ means the azimuthal (longitudinal or zonal) average defined as

$$\langle f \rangle(r, \theta) \equiv \frac{1}{2\pi} \int_0^{2\pi} f(r, \theta, \phi) d\phi.$$

Here we assume the centers of both spheres always keep the same position. The non-dimensional parameters in the equations are,

$$\tau = \sqrt{T} = \frac{2\Omega d^2}{\nu}, \quad P = \frac{\nu}{\kappa}, \quad R = \frac{\alpha\beta\gamma d^6}{\nu\kappa}, \quad I_{\mathrm{in}} = \frac{I_{\mathrm{in}}^*}{\rho d^5}, \tag{3.6}$$

where T is the Taylor number, P the Prandtl number, R the Rayleigh number, I_{in}^* the dimensional inertial moment of the inner sphere.

We choose the boundary condition of the velocity as no-slip and impermeable on both spheres, and the temperature disturbance is fixed to zero at the inner and outer spheres:

$$\boldsymbol{U}(r = r_{\mathrm{in}}, \theta, \phi, t) = \tilde{\boldsymbol{\Omega}}_{\mathrm{in}} \times (r_{\mathrm{in}} \boldsymbol{e}_r), \quad \boldsymbol{U}(r = r_{\mathrm{out}}, \theta, \phi, t) = \boldsymbol{0}, \tag{3.7}$$

$$\Theta(r = r_{\mathrm{in}}, \theta, \phi, t) = 0, \quad \Theta(r = r_{\mathrm{out}}, \theta, \phi, t) = 0, \tag{3.8}$$

where $\boldsymbol{e}_r$ is the unit vector in the radial direction.

Since the velocity field is solenoidal, it can be represented with the toroidal and poloidal potentials w and v as follows:

$$\boldsymbol{U} \equiv \nabla \times (\boldsymbol{r}(w + w_S)) + \nabla \times \{\nabla \times (\boldsymbol{r}v)\}, \tag{3.9}$$

where w_S is defined as

$$w_S(\boldsymbol{r}, \tilde{\boldsymbol{\Omega}}_{\rm in}(t)) \equiv -\frac{r_{\rm in}^3}{r_{\rm out}^3 - r_{\rm in}^3}\left(r - \frac{r_{\rm out}^3}{r^2}\right)\left(\boldsymbol{e}_r \cdot \tilde{\boldsymbol{\Omega}}_{\rm in}(t)\right). \tag{3.10}$$

Note that the velocity field described by w_S satisfies the above velocity boundary condition (3.7) [49]. Then the boundary condition of v and w are

$$v = \frac{\partial v}{\partial r} = w = 0 \quad \text{at} \quad r = r_{\rm in},\ r_{\rm out}. \tag{3.11}$$

The governing equations of these potentials and Θ become

$$\begin{aligned}\frac{\partial}{\partial t}\left(\hat{L}_2 w\right) = &\left[\nabla^2 \hat{L}_2 + \tau\frac{\partial}{\partial \phi}\right] w - \tau\hat{Q}v + \left[\left(\nabla^2 - \frac{\partial}{\partial t}\right)\hat{L}_2 + \tau\frac{\partial}{\partial \phi}\right] w_S \\ &- \boldsymbol{r} \cdot [\nabla \times ((\boldsymbol{U} \cdot \nabla)\boldsymbol{U})], \end{aligned} \tag{3.12}$$

$$\begin{aligned}\frac{\partial}{\partial t}\left(\hat{L}_2 \nabla^2 v\right) = &\left[\nabla^2 \hat{L}_2 + \tau\frac{\partial}{\partial \phi}\right] \nabla^2 v + \tau\hat{Q}w - \hat{L}_2\Theta + \tau\hat{Q}w_S \\ &- \boldsymbol{r} \cdot [\nabla \times \nabla \times ((\boldsymbol{U} \cdot \nabla)\boldsymbol{U})], \end{aligned} \tag{3.13}$$

$$P\frac{\partial \Theta}{\partial t} = R\hat{L}_2 v + \nabla^2\Theta - P(\boldsymbol{U} \cdot \nabla)\Theta, \tag{3.14}$$

where $\hat{L}_2$ and $\hat{Q}$ are the operators defined as eqs.(2.11) and (2.12), respectively.

We will fix the values of η and P as the standard value $\eta = 0.4$ and $P = 1$. The inertial moment of the inner sphere is set to be $I_{\rm in} = 8\pi(\eta/(1-\eta))^5/15 \simeq 0.22$, assuming that the density of the inner sphere is the same as that of fluid. This assumption is consistent with the self-gravitational force (2.2). We seek for the nonlinear traveling wave solutions bifurcating at the critical point by the Newton method and examine their linear stability by solving the eigenvalue problems in the range of $52 \leq \tau \leq 500$ under the governing equations (3.12)–(3.14) and (3.4) with the boundary conditions (3.7) and (3.8) ((3.11) for potentials). We use the Galerkin-spectral method, which is shown in Sec. 2.2.

To obtain the nonlinear traveling wave solutions using the Newton method, the truncation wavenumber of spherical harmonics L and the maximum degree of the Chebyshev polynomials N are set to both fixed to 21 in the

standard calculations, while larger (N, L) pairs are used in some calculations to spot-check the results. When the nonlinear solution is calculated by the Newton method, the nonlinear terms are evaluated in the physical space and are converted back into the spectral space (the spectral transform method). The numbers of the grid points on the physical space are chosen as $(N_r, N_\theta, N_\phi) = (33, 32, 64)$ in order to eliminate the aliasing errors, where N_r, N_θ and N_ϕ the number of grid points in the radial, zenith (colatitudinal) and azimuthal (longitudinal) directions, respectively. The detailed numerical methods are described in Appendices.

3.3 Results

We first consider critical convection with respect to the conductive rest state. Both the spheres are assumed to co-rotate until the thermal convection occurs. The linearized equations of the governing equations (3.12)–(3.14) and (3.4) can be separated into those for each azimuthal wavenumber m. The critical parameters and the critical modes with $m > 0$ in the system allowing the inner sphere rotation are exactly same as those in the co-rotating system, because the critical modes with $m > 0$ do not produce torque operating the inner sphere and then do not rotate the inner sphere differentially against the outer sphere (discussed in Sec. 2.3). The freely-rotating inner sphere condition does not affect the critical parameters and critical modes with $m > 0$. Therefore, we only calculate the critical parameters and critical modes with $m = 0$ in the system allowing the inner sphere rotation. In the range of $0 \leq \tau \leq 500$, the results of numerical calculations show that all the critical modes with $m = 0$ are equatorially anti-symmetric. Then they do not produce torque operating the inner sphere and do not rotate the inner sphere differentially. The critical parameters and critical modes with $m = 0$ are exactly same as those in the co-rotating system. Therefore, from the result of our previous study [2], we conclude that the critical azimuthal (longitudinal) wavenumber m_c is 3 in the range of $0 < \tau \leq 51$ while $m_c = 4$ in the range of $52 \leq \tau \leq 500$ in the system allowing the inner sphere rotation.

The finite-amplitude nonlinear traveling wave solutions which have fourfold symmetry in the azimuthal direction bifurcate at the critical points when $52 \leq \tau \leq 500$, and we call these solutions as TW4s (Traveling Wave 4). In the following, we seek these TW4 solutions using the Newton method and their linear stability is evaluated by solving eigenvalue problems in the system allowing the inner sphere rotation. In contrast to the critical convection, these finite-amplitude TW4 solutions accompany the differentially rotating inner sphere. The finite-amplitude solutions in the co-rotating system pro-

duce non-zero torque operating the inner sphere due to mean zonal flows (discussed in Sec. 2.3), and these solution induce only the axial component of torque because of the equatorial symmetry. When these solutions are allowed to rotate the inner sphere freely, the inner sphere accelerates in the direction of this torque until the steady rotation is established, while structure of the solutions are modified and the final convection pattern converges to the TW4 solutions in the system allowing the inner sphere rotation. In these TW4 solutions, the inner sphere rotates with e constant angular velocity $\boldsymbol{k}\cdot\tilde{\boldsymbol{\Omega}}_{\rm in} = \tilde{\Omega}_{{\rm in},z}$ against the outer sphere, and torques operating on both the inner and outer sphere exactly vanish because of stationary characteristics of the solutions.

3.3.1 Bifurcation diagram and inner sphere rotation

Figure 3.2 shows the stable region of the finite-amplitude TW4 solutions in the system allowing the inner sphere rotation. In these solutions, the inner sphere rotates against z-axis with the angular velocity $\boldsymbol{k}\cdot\tilde{\boldsymbol{\Omega}}_{\rm in} = \tilde{\Omega}_{{\rm in},z}$, which are described as colors and sizes of circles and boxes, in $\tau - R$ parameter space. Figure 3.3 shows the axial component of the angular velocity of the inner sphere $\tilde{\Omega}_{{\rm in},z}$ driven by the stable TW4 solutions for each τ. From Figure 3.2, we found that TW4s bifurcate supercritically from the rest conductive state at the critical points and they are stable in the region $R_c \leq R \lesssim 1.2 - 2R_c$, depending on the rotation rate τ. It is also found that the stable region of TW4s generally extends with increasing τ for $\tau \gtrsim 250$ and $52 \leq \tau \lesssim 100$. From Figures 3.2 and 3.3, it is found that the inner sphere rotates in the prograde direction when the rotation rate is small ($\tau \lesssim 160$). When τ is increased ($200 \lesssim \tau \lesssim 300$), the angular velocity of the inner sphere keeps nearly zero even when the Rayleigh number is increased to the marginal Rayleigh number. When τ is further increased ($\tau = 400$ and 500), the inner sphere rotates in the retrograde direction. The increasing rate of the inner sphere rotation rate is relatively large in small τ cases compared with large τ cases. Note that this tendency is consistent with that of torques operating the inner sphere in the co-rotating system (Fig. 2.2).

Figure 3.4 shows the obtained bifurcation diagram, which indicates stable TW4s and their propagating directions in $\tau - R$ parameter space. Comparing this figure with the bifurcation diagram in the co-rotating system shown in Figure 4 of Kimura *et al.*(2011), it is found that the stable region of TW4 solutions is qualitatively similar to that in the co-rotating system. Table 3.1 quantitatively compares the marginal Rayleigh numbers in the co-rotating system with those in the system allowing the inner sphere rotation. We found that in slowly rotating cases such as $\tau = 52$ and 100, the inner sphere

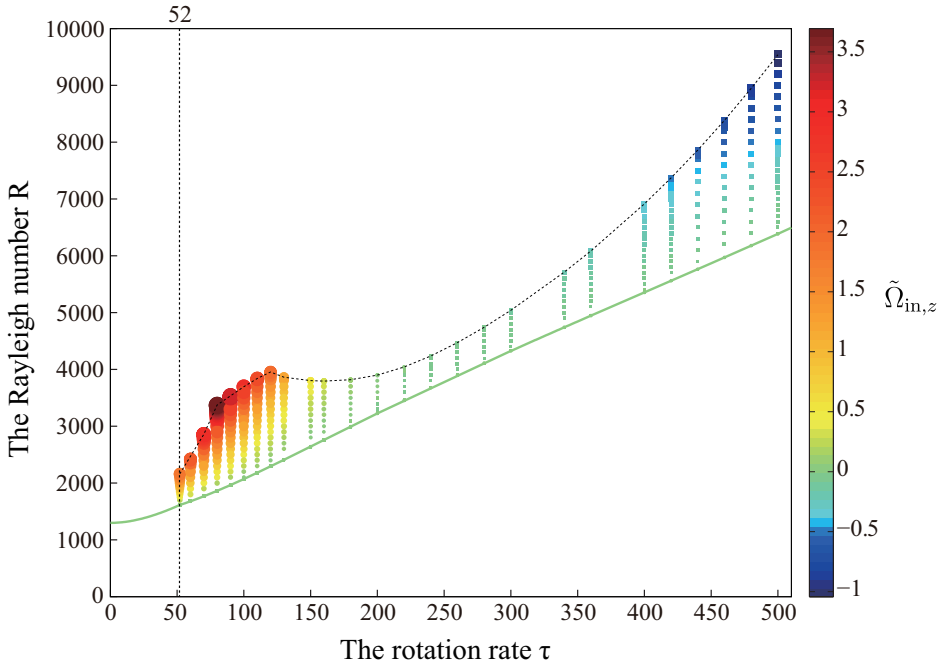

Figure 3.2: The stable region of the finite-amplitude TW4 solutions in the system allowing the inner sphere rotation. In these solutions, the inner sphere rotates against z-axis with the angular velocity $\boldsymbol{k} \cdot \tilde{\boldsymbol{\Omega}}_{\mathrm{in}} = \tilde{\Omega}_{\mathrm{in},z}$ All the TW4 solutions are stable on the colored circles and boxes. The circles mean $\tilde{\Omega}_{\mathrm{in},z} > 0$ while the boxes $\tilde{\Omega}_{\mathrm{in},z} < 0$, and the size of the symbols mean the amplitudes of $\tilde{\Omega}_{\mathrm{in},z}$. The upper black dashed line shows the marginal stability curve of the TW4 solutions, that is, TW4 solutions become unstable above the upper dashed line. The lower green solid line shows the critical curve of the conductive rest state in the rotating frame of reference, and the rotation rate of the inner sphere is absolutely zero on this line. The conductive rest state is stable below the lower solid line.

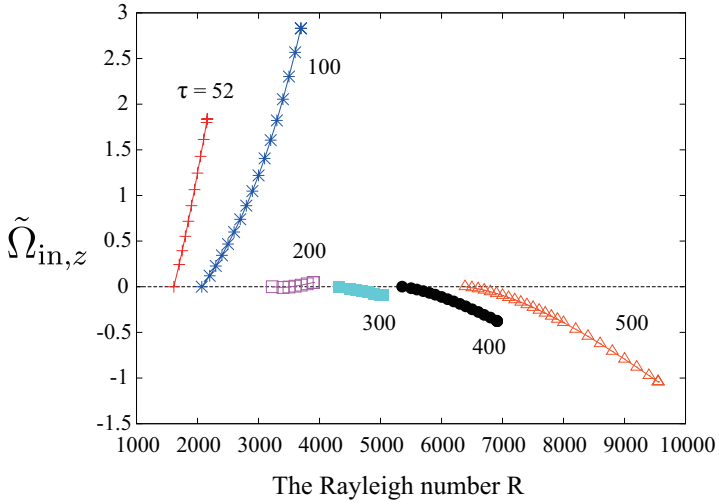

Figure 3.3: The axial component of the angular velocity of the inner sphere $\tilde{\Omega}_{\mathrm{in},z}$ induced by the stable TW4 solutions for each τ.

rotation stabilizes the TW4 solutions while that destabilizes TW4 solutions in moderately rotating cases ($\tau = 400$ and 500). However the ratio of the change of the marginal Rayleigh number is only about 1% or less. Therefore, we can conclude that the stable region of TW4 solutions is quantitatively similar to that in the co-rotating system.

3.3.2 Structure of convective motion

Figure 3.5 shows the distributions of the radial component of the velocity U_r on the equatorial plane and those of the axial component of the vorticity $\omega_z = \boldsymbol{k} \cdot (\nabla \times \boldsymbol{U})$ in a meridional cross section when the Rayleigh numbers are slightly below the marginal Rayleigh numbers of TW4 solutions. Note that all the TW4 solutions shown in Figure 3.5 propagate in the retrograde direction, that is, the patterns in the upper 6 panels drift in the clockwise direction. The propagating velocity of each panel is shown in Table 3.2. It is found that, when the rotation rate is small such as $\tau = 52$ and 100, the convection patterns are circular on the equatorial plane (upper (i) and (ii) in Figure 3.5) and the convection cells bend along the shell boundary (lower (i) and (ii) in Figure 3.5). As the rotation rate is increased, the convection patterns come to tilt in the prograde-outward direction (upper (v) and (vi) in Figure 3.5) and the convection cells elongate in the direction of the rotation axis of the outer sphere (lower (v) and (vi) in Figure 3.5). Comparing these

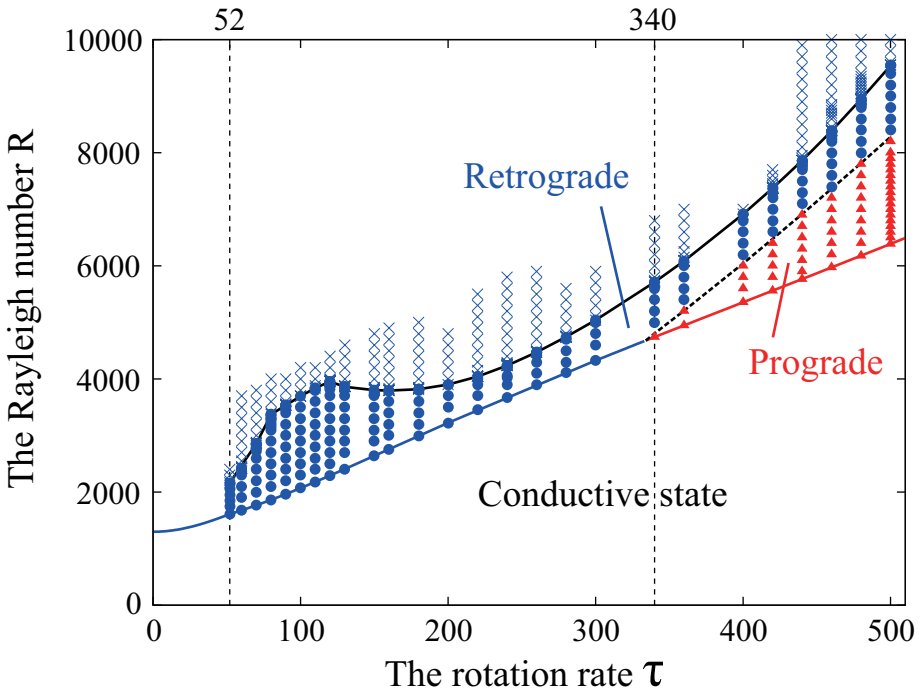

Figure 3.4: A bifurcation diagram of the stable finite-amplitude TW4 solutions in the system allowing the inner sphere rotation. The propagating direction of the solution is shown by a blue circle (retrograde) and a red triangle (prograde). The lower solid curve shows the marginal stability of the stationary (conductive) solution. where the blue curve ($\tau < 340$) shows that the propagating direction of the critical solutions is retrograde, and the red curve ($\tau \geq 340$) prograde. All circles and triangles mean that the TW4 solutions are stable. TW4s become unstable above the upper black solid line. The propagating velocity v_p vanishes on the dashed line. The blue crosses mean that the TW4 solutions propagating in the retrograde direction are unstable.

τ	R_c	R_f^{TW4}	R_c^{TW4}	
52	1612.5026	2162	2133	+1.4%
100	2070.3920	3695	3675	+0.5%
200	3224.8090	3900	3902	−0.0%
300	4324.7513	5040	5044	−0.0%
400	5355.1777	6914	6924	−0.1%
500	6386.6056	9540*	9590*	−0.5%

Table 3.1: The critical Rayleigh number R_c, the marginal Rayleigh number R_c^{TW4} in the co-rotating system and the marginal Rayleigh number R_f^{TW4} in the system allowing the inner sphere rotation for each τ. The last column shows $(R_f^{\mathrm{TW4}} - R_c^{\mathrm{TW4}})/R_c^{\mathrm{TW4}}$. The error of each marginal Rayleigh number is less than ± 1 for $\tau \leq 400$ and ± 10 for $\tau = 500$. Values labeled with asterisk appearing in cases $\tau = 500$ are calculated with the truncation wavenumbers $(N, L) = (21, 28)$. R_c and R_c^{TW4} have already been shown in Table 3 of Kimura *et al* [2], but these values on this table are more accurate (nearly 0.1% or less).

patterns of TW4s with those in the co-rotating system shown in Figure 8 of Kimura *et al.*(2011) [2], we found that the convection patterns of stable TW4s in the system allowing the inner sphere rotation are quantitatively similar to those in the co-rotating system. The differences of the amplitude of U_r and ω_z are at most 2% and 5%, respectively.

Figure 3.6 shows the azimuthal component of the velocity U_ϕ of the stable TW4 solutions in the system allowing the inner sphere rotation on the equatorial plane ($\theta = 90°$) when the Rayleigh numbers are slightly below the marginal Rayleigh numbers of TW4 solutions. It is found that when the rotation rate is small, the distribution of U_ϕ on the equatorial plane is spiralling in the clockwise (retrograde) direction from the inner to the outer spheres ((i) and (ii) in Figure 3.6). However, as the rotation rate is increased, this spiral structure becomes weak ((iii) and (iv) in Figure 3.6), and as the rotation rate is further increased, the distribution becomes spiralling in the counter-clockwise (prograde) direction from the inner to the outer spheres ((v) and (vi) in Figure 3.6). Note again that all these distributions of U_ϕ shown in Figure 3.6 propagate in the retrograde direction. Figure 3.7 shows the radial profiles of U_ϕ of the stable TW4 solutions in the system allowing the inner sphere rotation and those in the co-rotating system on the section shown as the dashed lines in Figure 3.6. The maximum of U_ϕ on the equatorial plane exists on this section for each τ. We found that, when $\tau = 52$ and

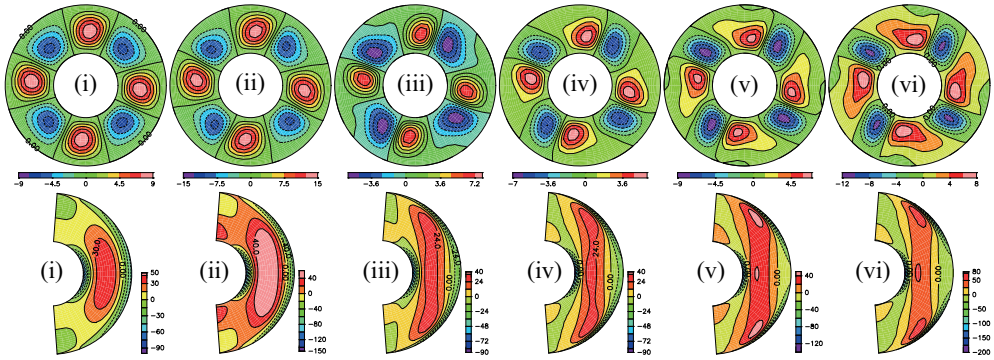

Figure 3.5: The convection patterns of stable TW4s in the system allowing the inner sphere rotation when the Rayleigh numbers are slightly below the marginal Rayleigh numbers of TW4 solutions. The upper 6 panels show the radial component of velocity U_r on the equatorial plane ($\theta = 90°$) and the lower 6 panels show the axial component of vorticity $\omega_z = \boldsymbol{k} \cdot (\nabla \times \boldsymbol{U})$ in a meridional section. The detailed parameters are listed in Table 3.2.

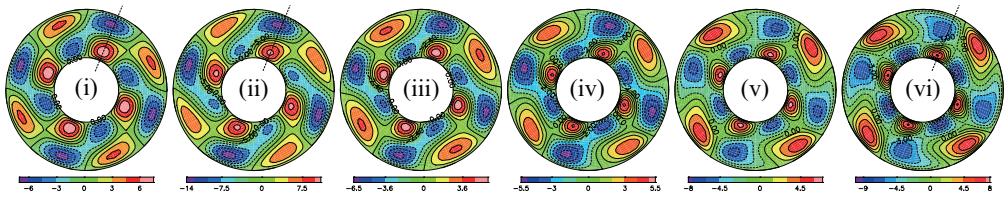

Figure 3.6: The azimuthal component of the velocity U_ϕ of the stable TW4 solutions in the system allowing the inner sphere rotation on the equatorial plane ($\theta = 90°$) when the Rayleigh numbers are slightly below the marginal Rayleigh numbers of the TW4 solutions. Dashed lines indicate the cross sections of Figure 3.7. The detailed parameters are listed in Table 3.2.

	τ	R	$v_p^{(\mathrm{frot})}$	$\tilde{\Omega}_{\mathrm{in},z}$	U_{in}
(i) and (I)	52	2100	-0.60	$+1.61$	$+1.07$
(ii) and (II)	100	3600	-1.58	$+2.57$	$+1.71$
(iii) and (III)	200	3800	-1.49	$+0.03$	$+0.02$
(iv) and (IV)	300	5000	-0.83	-0.09	-0.06
(v) and (V)	400	6900	-0.62	-0.37	-0.25
(vi) and (VI)	500	9200	-0.59	-0.88	-0.59

Table 3.2: The control and resulting parameters of the typical stable TW4 solutions in the system allowing the inner sphere rotation shown in the Figures and Tables below. $v_p^{(\mathrm{frot})}$ is the propagating velocity in the azimuthal direction. $\tilde{\Omega}_{\mathrm{in},z}$ is the axial angular velocity of the inner sphere rotation. U_{in} is the surface velocity of the inner sphere on the equatorial plane, that is, $U_{\mathrm{in}} = r_{\mathrm{in}}\tilde{\Omega}_{\mathrm{in},z}$. The Rayleigh numbers are slightly less than the marginal Rayleigh numbers R_c^{TW4} and R_f^{TW4}, which are shown in Table 3.1.

100, U_ϕ near the inner sphere is strengthened toward the prograde direction due to prograde rotation of the inner sphere. The difference of the maximum value of U_ϕ on the equatorial plane is about 8% for $\tau = 52$ and 6% for $\tau = 100$. When $\tau = 500$, U_ϕ near the inner sphere is strengthened toward the retrograde direction due to retrograde rotation of the inner sphere, but the difference of maximum value of U_ϕ on the equatorial plane is only about 2%. We also found that, the distributions of $\langle U_\phi \rangle$ in the outer region ($r \gtrsim 1.1$ for $\tau = 52$ and $\tau = 100$ and $r \gtrsim 0.8$ for $\tau = 500$) on the equatorial plane are scarcely changed compared with those in the co-rotating system.

Table 3.3 shows the comparison of the propagating velocity of the stable TW4 solutions in the azimuthal direction in the system allowing the inner sphere rotation and that in the co-rotating system. The last column shows that $(v_p^{(\mathrm{frot})} - v_p^{(\mathrm{corot})})/v_p^{(\mathrm{corot})}$, indicating the difference of the amplitude of the propagating velocity. We found that the propagating direction of the TW4 solution in the system allowing the inner sphere rotation is same as that in the co-rotating system for each τ. Also little different appears in the amplitudes. When the rotation rate is small, the relative difference is at most 15% while it is at most 9% when the rotation rate is large.

3.3.3 Structure of mean zonal flow

Figure 3.8 shows the distributions of the mean zonal flows $\langle U_\phi \rangle$ of the stable TW4 solutions in the system allowing the inner sphere rotation (labeled with

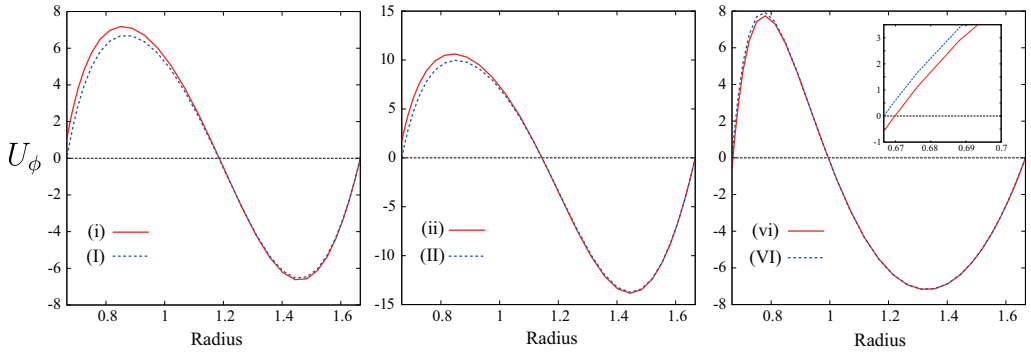

Figure 3.7: The radial profiles of U_ϕ of stable TW4 solutions in the system allowing the inner sphere rotation (red solid line) and those in the co-rotating system (blue dashed line) on the section shown by the dashed lines in Figure 3.6. The inset in the rightmost panel is the enlarged drawing near the inner sphere ($r_{\rm in} \leq r \leq 0.7$). The detailed parameters are listed in Table 3.2.

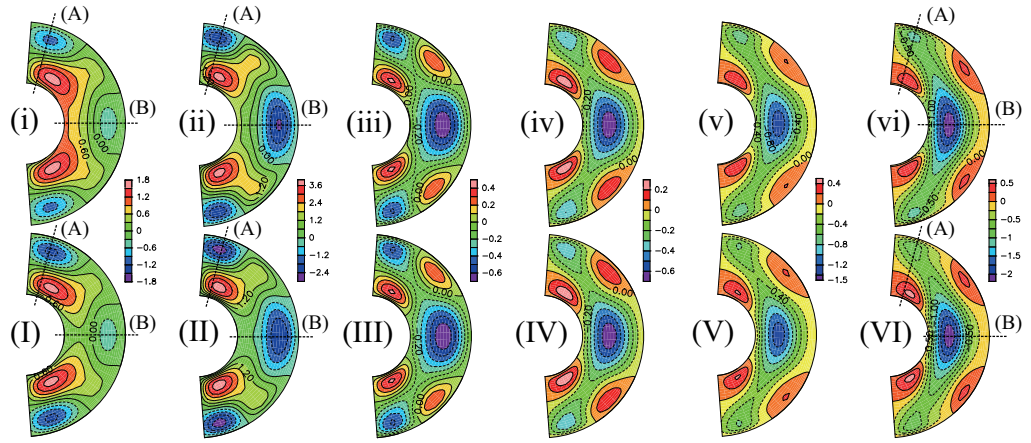

Figure 3.8: Meridional distributions of mean zonal flow $\langle U_\phi \rangle$ of the stable TW4 solutions in the system allowing the inner sphere rotation (upper 6 panels, labeled with lowercase Roman numerals) and in the co-rotating system (lower 6 panels, labeled with uppercase Roman numerals). The distributions in the co-rotating system already appear in Figure 9 of Kimura *et.al* (2011) [2]. Dashed lines (A) and (B) label the sections shown in Figure 3.9. The detailed parameters for each panel are listed in Table 3.2.

	$\tilde{\Omega}_{\mathrm{in},z}$	$v_p^{(\mathrm{frot})}$		$v_p^{(\mathrm{corot})}$	
(i)	$+1.61$	-0.60	(I)	-0.70	-15%
(ii)	$+2.57$	-1.58	(II)	-1.71	-8%
(iii)	$+0.03$	-1.49	(III)	-1.49	-0%
(iv)	-0.09	-0.83	(IV)	-0.83	$+0\%$
(v)	-0.37	-0.62	(V)	-0.60	$+3\%$
(vi)	-0.88	-0.59	(VI)	-0.54	$+9\%$

Table 3.3: The comparison of the propagating velocity of the stable TW4 solutions in the azimuthal direction in the system allowing the inner sphere rotation ($v_p^{(\mathrm{frot})}$) and that in the co-rotating system ($v_p^{(\mathrm{corot})}$). The first and second columns show the same parameters listed in Table 3.2. The last column shows $(v_p^{(\mathrm{frot})} - v_p^{(\mathrm{corot})})/v_p^{(\mathrm{corot})}$.

the small Roman numerals) and those in the co-rotating system (labeled with the capital Roman numerals). When the rotation rate is small the strong prograde (retrograde) zonal flow locates in the vicinity of the poles in the inner (outer) part of the shell and weak retrograde zonal flow locates near the outer spheres around the equatorial plane (Figure 3.8 (i)). As the rotation rate is increased, the retrograde equatorial zonal flow is strengthened and is extending to the inner region. The prograde regions near the inner sphere in high-latitudes extend to the outer regions, separate, and strong prograde zonal flows emerge in the mid-latitudes near the outer sphere (Figures 3.8 (ii) and (iii)). As the rotation rate is further increased, the retrograde zonal flows in the vicinity of the poles near the outer sphere are weakened, while the prograde flows near the inner sphere keep their magnitudes. The strong equatorial retrograde zonal flow near the inner sphere and the strong prograde zonal flows in the mid-latitude near the outer sphere keep their magnitudes. (Figures 3.8 (iv)–(vi)). These zonal flow patterns of the stable TW4 solutions in the system allowing the inner sphere rotation seem to be qualitatively similar to those in the co-rotating system (comparing (i)–(vi) with (I)–(V I) in Figure 3.8). However, the amplitudes of these zonal flows are slightly different.

Figure 3.9 shows the radial profiles of the mean zonal flows $\langle U_\phi \rangle$ on the section (A) and (B) shown in Figure 3.8. The lowercase Roman numerals indicate the system allowing the inner sphere rotation and the uppercase Roman numerals mean the co-rotating system. The minimum value of each zonal flow in the whole meridional domain exists on the section (A) when $\tau = 52$ and 100, and on the section (B) when $\tau = 500$. From (i)-(A), (I)-

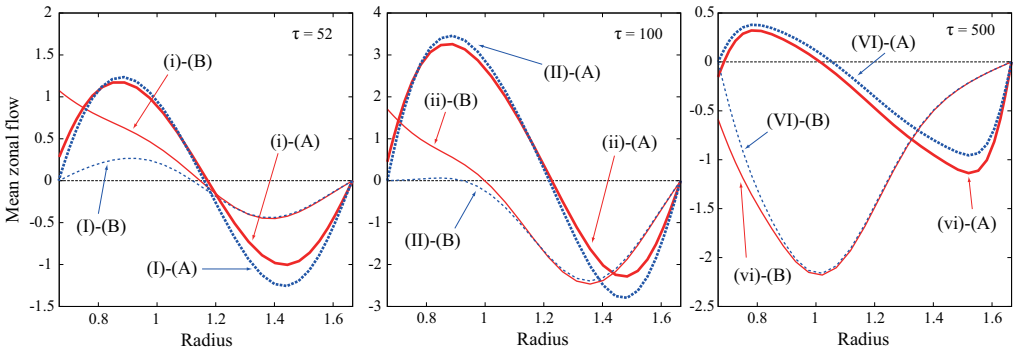

Figure 3.9: The radial profiles of the mean zonal flow $\langle U_\phi \rangle$ in the sections labeled with the dashed lines (A) and (B) shown in Fig. 3.8. The thick red solid and thick blue dashed lines mean the radial profiles of $\langle U_\phi \rangle$ on the section (A) in the system allowing the inner sphere rotation and in the co-rotating system, respectively. The thin red solid and thin blue dashed lines mean the distributions on the section (B) in the system allowing the inner sphere rotation and in the co-rotating system, respectively. The detailed parameters are listed in Table 3.2.

(A), (ii)-(A) and (II)-(A) on the left and middle panels in Figure 3.9, it is found that when $\tau = 52$ and 100, where the inner sphere rotates in the prograde direction, the maximum value of $\langle U_\phi \rangle$ on the section (A) is slightly smaller $(5 - 6\%)$ than that in the co-rotating system and the amplitude of the minimum value on the section (A) is also smaller than that in the co-rotating system (by 22 % for $\tau = 52$ and 12% for $\tau = 100$). Therefore, the amplitude of the mean zonal flow near the polar region becomes weaker due to the inner sphere rotation when the rotation rate is small. On the other hand, it is found that the entire radial profile of $\langle U_\phi \rangle$ on the section (A) becomes uniformly smaller than that in the co-rotating system when $\tau = 500$ where the inner sphere rotates in the retrograde direction ((vi)-(A), (VI)-(A) on the right panel in Figure 3.9). The maximum of the prograde zonal flow located in the vicinity of the poles near the inner sphere is also decreased by 16%. Therefore, when the rotation rate is large, the mean zonal flow is accelerated toward the retrograde direction not only near the inner sphere but also near the outer sphere due to the inner sphere rotation. When $\tau = 200$ and 300, where the inner sphere scarcely rotates, we found that the difference of the amplitudes of $\langle U_\phi \rangle$ from that in the co-rotating system is at most 3% (not shown). This difference is relatively small compared with that in the slowly and rapidly rotating cases. From the radial profile of

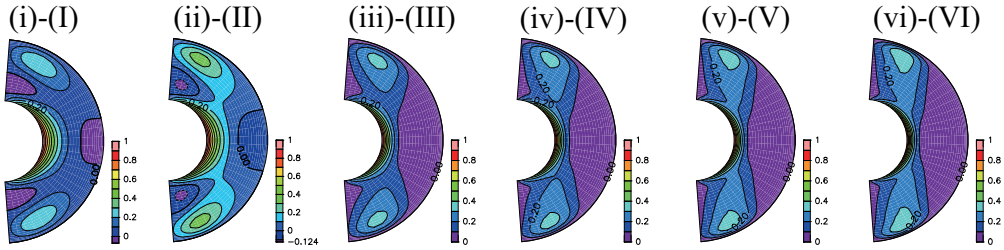

Figure 3.10: The difference of the mean zonal flows in the system allowing the inner sphere rotation from those in the co-rotating system normalized with the equatorial surface velocity of the inner sphere $\Delta\langle U_\phi\rangle/U_{\rm in}$, where $\Delta\langle U_\phi\rangle \equiv \langle U_\phi^{(\rm frot)}\rangle - \langle U_\phi^{(\rm corot)}\rangle$, $U_\phi^{(\rm frot)}$ and $U_\phi^{(\rm corot)}$ mean the azimuthal component of the velocity of stable TW4 solutions in the system allowing the inner sphere rotation and that in the co-rotating system, respectively, and $U_{\rm in}$ is the equatorial surface velocity of the inner sphere. $U_{\rm in}$ for each τ and the detailed parameters are listed in Table 3.2. Note that the actual direction of the mean zonal flows is opposite in the cases of (iv)-(IV), (v)-(V) and (vi)-(VI) due to the negative normalization factor $U_{\rm in}$.

$\langle U_\phi\rangle$ on the equatorial plane (section (B) in Figure 3.9), it is found that the strong equatorial prograde zonal flows are induced near the inner sphere when $\tau = 52$ and 100, while when $\tau = 500$ the retrograde zonal flow is induced there, which are consistent with the inner sphere rotation. On the other hand, the distributions of $\langle U_\phi\rangle$ in the equatorial outer region are scarcely changed compared with those in the co-rotating system, that is, the amplitudes of the retrograde zonal flow on the equatorial plane are hardly changed compared with those in the co-rotating system for $\tau = 52$, 100 and 500.

Figure 3.10 shows the difference of the mean zonal flows in the system allowing the inner sphere rotation from those in the co-rotating system normalized with the surface velocity of the inner sphere on the equatorial plane. Note that $U_{\rm in} > 0$ when $\tau \leq 200$ while $U_{\rm in} < 0$ when $\tau \geq 300$ (see Table 3.2). We found that, when $\tau = 52$ and 100 (left two panels in Figure 3.10), the difference of $\langle U_\phi\rangle$ is large near the whole inner sphere and becomes maximum on the surface of the inner sphere around the equator. The other positive peaks exist at high-latitude near the outer sphere. There are also negative peaks in the vicinity of the poles near the inner sphere, while the weak negative region exist near the outer sphere in the equatorial region. As the rotation rate is increased as $\tau = 200$ and 300 (middle two panels in Figure 3.10), the difference is large near the whole surface of the inner sphere and the maximum value of the difference locates on the equatorial surface of

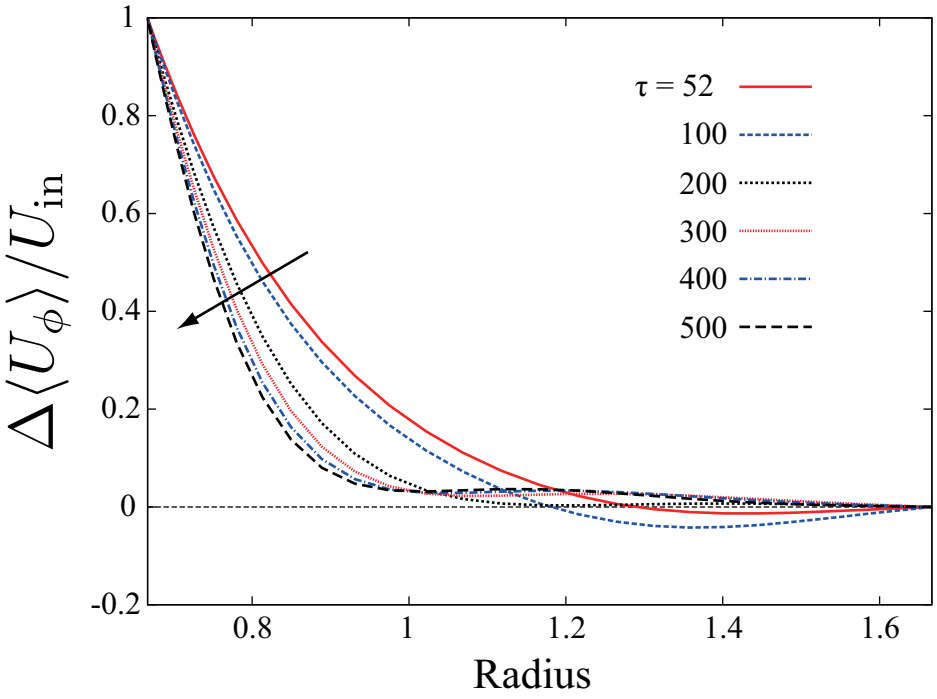

Figure 3.11: The radial profile of $\Delta\langle U_\phi\rangle/U_{\rm in}$ in the equatorial plane for each τ. The curves in the direction of the arrow corresponds to the variation of τ from 52 to 500.

the inner sphere, however, the radial width of large difference region around the equatorial plane becomes thinner. This can be seen quantitatively in the radial profile of $\Delta\langle U_\phi\rangle/U_{\rm in}$ on the equatorial plane shown in Figure 3.11. The negative difference regions in the vicinity of the poles near the inner sphere come to vanish. As the rotation rate is further increased as $\tau = 400$ and 500 (right two panels in Figure 3.10), the radial width of large difference region on the equatorial plane becomes further thinner, and the positive peaks locate at high-latitude near the outer sphere. However, the positive difference regions including the above peaks extend toward the inner sphere along the rotation axis in the tangential cylinder of the inner sphere.

3.4 Conclusion and discussion

We obtained the stability and a bifurcation diagram of the finite-amplitude traveling wave solution TW4, which bifurcates supercritically at the critical point and propagate in the azimuthal direction, in the system allowing the

inner sphere rotation under the no-slip and fixed-temperature boundary conditions for the ratio of the inner and outer radii $\eta = 0.4$ and the Prandtl number $P = 1$ (Figs. 3.2 and 3.4). Note that the TW4 solutions shown in the previous section are independent of the magnitude of the inertial moment of the inner sphere whenever the profile of the gravitational force (2.2) is unchanged, because the torque operating on the inner sphere vanishes for each steady solution. The obtained TW4 solutions bifurcate supercritically from the conductive rest state at the critical points, and are stable from the critical Rayleigh number R_c to $1.2 - 2R_c$, depending on the rotation rate τ (Figs. 3.2 and 3.4). When the rotation rate is small, the inner sphere rotates in the prograde direction against the outer sphere. As the rotation rate is increased, the inner sphere scarcely rotates even when the Rayleigh number is increased. As the rotation rate is further increased, the inner sphere rotates in the retrograde direction (Figs. 3.2 and 3.3). However, the difference of the stable regions of the TW4 solutions between in the system allowing the inner sphere rotation and in the co-rotating system is quite small as about 1% or less (Table 3.1). Therefore the bifurcation diagram is quantitatively similar to that in the co-rotating system (Fig. 1.1).

We also found that, the difference of the convection patterns of the stable TW4 solutions in the system allowing the inner sphere rotation from those in the co-rotating system is at most several percent, and those patterns are quantitatively similar. (Figs. 3.5, 3.6 and 3.7). The patterns of the mean zonal flows are qualitatively similar (Fig. 3.8), however, the apparent difference of the mean zonal flow profile can be seen on the equatorial plane near the inner sphere due to the inner sphere rotation. The maximum difference of the amplitudes of the mean zonal flows of the stable TW4 solutions is about 20%, which is relatively large compared with that of U_r, ω_z of convection patterns.

The difference of the mean zonal flows is larger than that of the convection patterns. This tendency can be explained in terms of the weakly nonlinear analyses, discussed in Sec. 2.4. In the co-rotating system, we expand the dependent variables $\boldsymbol{u}$ (velocity), T (temperature), π (pressure) and the Rayleigh number R around the critical state with a small parameter ϵ as $\boldsymbol{u} = \epsilon \boldsymbol{u}^{(1)} + \epsilon^2 \boldsymbol{u}^{(2)} + \cdots$, $R = R_c + \epsilon R^{(1)} + \epsilon^2 R^{(2)} + \cdots$, where R_c is the critical Rayleigh number of the conductive rest state and $\boldsymbol{u}^{(1)}$ is the critical mode which can be obtained using the eigenpair calculation. The axial component of torque operating the inner sphere $N_{\mathrm{in},z}$ also can be expanded as $N_{\mathrm{in},z} = \epsilon N_{\mathrm{in},z}^{(1)} + \epsilon^2 N_{\mathrm{in},z}^{(2)} + \cdots$, where each order of this torque $N_{\mathrm{in},z}^{(i)}$ can be calculated by $u_\phi^{(i)}$ using the equation (3.5). However, in the range of the parameters we examine, $N_{\mathrm{in},z}^{(1)}$ vanishes due to the sinusoidal oscillation of $u_\phi^{(1)}$

in the azimuthal direction (the critical azimuthal wavenumber is non-zero). Therefore, the torque on the inner sphere is $O(\epsilon^2)$. As a result, in the system allowing the inner sphere rotation, the magnitude of the inner sphere rotation due to this torque operating the inner sphere is $O(\epsilon^2)$. This means that the effect of the inner sphere rotation on the convection patterns is $O(\epsilon^2)$ and the patterns of convective motion described such as U_r and ω_z, shown in Fig. 3.5, are hardly affected because these are $O(\epsilon)$. On the other hand, the mean zonal flow $\langle U_\phi \rangle$ can be affected by the inner sphere rotation effectively since it is $O(\epsilon^2)$. Specifically speaking, the velocity of TW4 solution $\boldsymbol{U}$ in the system allowing the inner sphere rotation can be written as

$$\boldsymbol{U} = \epsilon \boldsymbol{u}^{(1)} + \epsilon^2 \left(\boldsymbol{u}^{(2)} + \boldsymbol{u}^{(\mathrm{f},2)} \right) + \cdots , \tag{3.15}$$

where $\boldsymbol{u}^{(\mathrm{f},2)}$ is the second order correction term due to the inner sphere rotation and must satisfy

$$0 = 2\pi r_{\mathrm{in}}^3 \int_0^\pi \left[\frac{\partial \left\langle u_\phi^{(2)} \right\rangle}{\partial r} + \left(\frac{\partial \left\langle u_\phi^{(\mathrm{f},2)} \right\rangle}{\partial r} - \frac{\left\langle u_\phi^{(\mathrm{f},2)} \right\rangle}{r} \right) \right]_{r=r_{\mathrm{in}}} \sin^2\theta d\theta, \tag{3.16}$$

because the torque on the inner sphere of the TW4 solutions must vanish in the system allowing the inner sphere rotation due to the stationarity of these solutions. Each higher order correction term is also needed to satisfy the condition that the torque operating the inner sphere must vanish.

The structure of the correction term $\boldsymbol{u}^{(\mathrm{f})}$ in the rapidly rotating case can be interpreted as a spherical Couette flow, where the flow is driven only by slightly differential rotation of the inner and outer spheres in a rapidly rotating spherical shell [50, 51, 52, 53]. Figure 3.12 compares the correction of the flow in the system allowing the inner sphere rotation from the co-rotating system with the spherical Couette flow with the same rotation parameters at $\tau = 500$. Note that the actual direction of the mean meridional circulations is opposite since the normalization factor $U_{\mathrm{in}} < 0$ at $\tau = 500$. From this Figure we found that the difference of the flow in the system allowing the inner sphere rotation from that in the co-rotating system is quite similar to the spherical Couette flow. The features of spherical Couette flows listed below are investigated theoretically in Stewartson (1966) [51] and well described numerically in Hollerbach (1994) [52] and Dormy *et al.* (1998) [53];

(i) the magnitude of the z-component of the angular velocity of the fluid and that of the mean meridional circulation are large only inside the tangential cylinder and there is almost no flow outside the tangential cylinder,

(ii) the Ekman boundary layers exist near the whole inner sphere and near the outer sphere at high-latitude inside the tangential cylinder,

(iii) the strong mean meridional circulation from the inner sphere to the outer sphere (the actual direction of the mean circulation is opposite) exists near the tangential cylinder.

Moreover, when $\tau = 500$, the torque operating on the inner sphere due to the TW4 solution in co-rotating system is -15.0 while that due to the flow induced by only the inner sphere differential rotation shown at the lower two panels in Figure 3.12 is $+14.0$. Therefore, the summation of these torques on the inner sphere is nearly zero, meaning that the equation (3.16) is almost satisfied.

The propagating velocity of the TW4 solutions in the azimuthal direction is also changed and the difference is large compared with the differences of U_r and ω_z (Table 3.3). This can also be explained in terms of the weakly nonlinear analyses. Propagating direction of the large amplitude TW4 solutions in the co-rotating system is not determined by the vortex stretching/shrinking mechanism proposed by Takehiro [37], but by the advection of the convection cell by the mean zonal flow (Figs. 11, 12 and 13 in Kimura *et al.*(2011)). Since the magnitudes of the mean zonal flow is $O(\epsilon^2)$ it effectively affects the inner sphere rotation. Then, the propagating velocity is effectively changed by the inner sphere rotation through the effective change of the amplitude of the mean zonal flow. Actually, the change of the propagating velocity shown in Table 3.3 corresponds to the change of the mean zonal flow. When the rotation rate is small, the retrograde propagating velocity is weakened because the amplitude of the retrograde zonal flow becomes small while that of prograde zonal flows is unchanged. When the rotation rate is large, the retrograde propagating velocity is strengthened because the retrograde zonal flow is strengthened in the whole meridional plane.

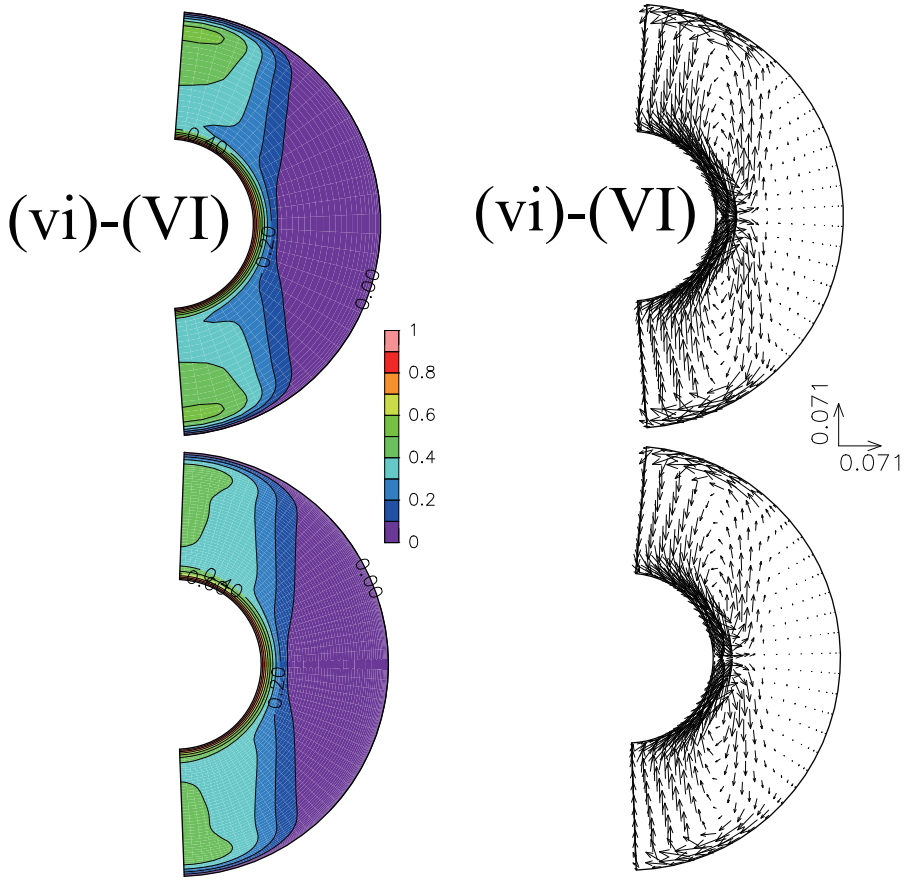

Figure 3.12: Comparison between the difference of the flow in the system allowing the inner sphere rotation from those in the co-rotating system (upper two panels) and the flow in the rotating spherical shell with slightly differential inner sphere rotation (lower two panels) when $\tau = 500$. The upper left panel shows the difference of the z-component of the angular velocity of the fluid in the system allowing the inner sphere rotation from those in the co-rotating system normalized with the inner sphere rotation rate $\Delta\langle U_\phi/s\rangle/\tilde{\Omega}_{\mathrm{in},z}$, where $\Delta\langle U_\phi/s\rangle \equiv \langle U_\phi^{(\mathrm{frot})}/s\rangle - \langle U_\phi^{(\mathrm{corot})}/s\rangle$ and $s = r\sin\theta$. The right upper panel shows the difference of the mean meridional circulation in the system allowing the inner sphere rotation from those in the co-rotating system normalized with the equatorial surface velocity of the inner sphere $(\Delta\langle U_r\rangle/U_{\mathrm{in}}, \Delta\langle U_\theta\rangle/U_{\mathrm{in}})$. The lower left (right) panel shows the z-component of the angular velocity (mean meridional circulation) of the fluid in a rotating spherical shell whose the inner sphere rotates with $\tilde{\Omega}_{\mathrm{in},z} = -0.88$ against the outer sphere, which is the same value of the rotation rate of the case (vi). Note that the actual direction of the mean meridional circulations is opposite since the normalization factor $U_{\mathrm{in}} < 0$ at $\tau = 500$.

Chapter 4

Emergence of equatorially asymmetric convection pattern

4.1 Introduction

In the previous chapter, we found that the stable region and bifurcation structure of finite-amplitude convective solution TW4s in the system allowing the rotation of both spheres are quantitatively similar to those in the co-rotating system. The convective motions of TW4 solution are also qualitatively similar but the amplitude of the mean zonal flow and the propagating velocity of TW4 are effectively changed due to inner sphere rotation. We consider that this behaviour can be explained in terms of weakly nonlinear analyses: the amplitude of convective motions $O(\epsilon)$ while that of mean zonal flow and of inner sphere rotation are both $O(\epsilon^2)$ because the torque on the inner sphere is $O(\epsilon^2)$ in the co-rotating system.

Then, in this chapter, we investigate the difference of behaviours of convective solutions between in the co-rotating system and in the system allowing the rotation of both spheres at larger Rayleigh numbers, where nonlinear effect of convective solution is expected to larger than that of stable TW4 solution.

As is mentioned in Chap. 1, there have been many researches for finite-amplitude convective solutions in terms of fluid mechanics thanks to recent remarkable progress of computational ability [18, 19, 34, 35].

Ardes *et al.* [18] focused on a little rapid rotation region ($\tau = 2 \times 10^3$) at the ratio of the inner and outer radii of the shell $\eta = 0.4$ and relatively low Prandtl number ($P = 0.1$) under stress-free and fixed-temperature boundary conditions for investigating finite-amplitude convection patterns [1]. They

[1] Ardes *et al.* [18] found that not only the columnar mode, equatorially attached mode,

found that the convective solution transits as follows: stationary drifting solution (called as a traveling wave solution in this thesis), vacillating solution, quasi-periodic solution and aperiodic solution (called as a chaotic solution in this thesis), in the range $1.0\times10^4 \leq R \leq 2.0\times10^4$, where the critical Rayleigh number is about 4500. Note that the dominant azimuthal wavenumbers of the traveling wave solution and vacillating solution are both 1 (shown in Fig.9 in their paper) while the critical azimuthal wavenumber is 3. Note also that the chaotic solution at $R = 2.0 \times 10^4$ still remains symmetric with respect to the equatorial plane, called as equatorial symmetry in this thesis.

Grote and Busse [35] investigated the behaviour of convective solutions as the Rayleigh number is increased when the rotation rate is large ($\tau = 10^4$ and 1.5×10^4) and the Prandtl number is moderate ($P = 1.0$ and 0.5). They showed that, when the Rayleigh number is relatively small, the transition of convection patterns is same as that in Ardes *et al.* (1997). As the Rayleigh number is increased, localized turbulent convection pattern appears and is sustained. As the Rayleigh number is further increased, the relaxation oscillation occurs, that is, kinetic energy slowly decays periodically after its rapid increasing.

Simitev and Busse [19] investigated the behaviour of convective solutions when the rotation rate is large ($\tau = 3.0 \times 10^4$) and the Prandtl numbers are moderate and small ($P = 0.5$, 0.1 and 0.025). They showed that, when the Prandtl number is relatively small ($P = 0.1$), the spiralling columnar convection emerging as a critical mode in rapidly rotating cases becomes unstable at a larger Rayleigh number. When the Rayleigh number is increased, the amplitude vacillations, shape vacillations and the chaotic behaviours occur, and the relaxation oscillation occurs as the Rayleigh number is further increased. When the Prandtl number is small ($P = 0.025$), the equatorially attached convection pattern, which emerges as a critical mode, becomes modulate but is still concentrated near the outer sphere at a larger Rayleigh number. As the Rayleigh number is further increased, the equatorially attached eddies spread into interior region and become detached in some cases.

In this way, transition of convective solutions from traveling wave solutions to chaotic solutions has been gradually revealed in the parameter space. However, there have been few researches around an emerging point of equatorial asymmetric convection patterns. Especially the route from equatorially symmetric pattern to equatorially asymmetric pattern is not known. Then, in this chapter, we investigate the effect of inner and outer spheres rotation

spiralling columnar mode but also multi-cellular mode appear as critical modes, in a wide parameter range on $P - \tau$ plane, where P is the Prandtl number and τ is the square root of the Taylor number. They fixed the ratio of the inner and outer radii as 0.4.

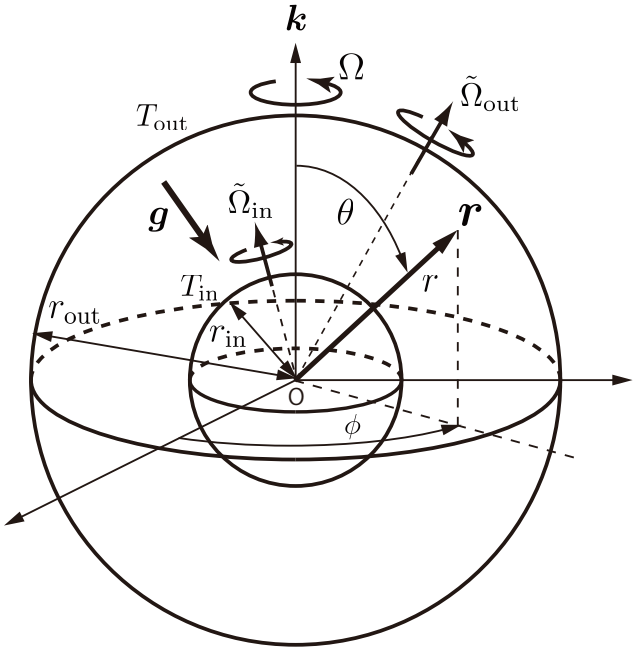

Figure 4.1: A schematic picture of the configuration of the Boussinesq thermal convection problem allowing the rotation of both the spheres.

to an emergence of equatorially asymmetric pattern through focusing on the routes from equatorially symmetric convection pattern to equatorially asymmetric convection pattern both in the co-rotating system and in the system allowing rotation of the inner sphere.

The model, governing equations and numerical methods are described in Sec. 4.2. In Sec. 4.3, we show the routes from equatorially symmetric convective solution to equatorially asymmetric one both in the co-rotating system and in the system allowing the rotation of both spheres, with some typical behaviours of each convective solution. The conclusions and discussions are described in Sec. 4.4.

4.2 Model and numerical method

Let us consider a Boussinesq fluid in a spherical shell whose radii of the inner and outer spheres are $r_{\rm in}$ and $r_{\rm out}$, respectively, shown in Figure 4.1. This system is same as that in Sec. 3.2 except for the outer sphere rotation. The inner and outer spheres are rotating with $\tilde{\boldsymbol{\Omega}}_{\rm in}$ and $\tilde{\boldsymbol{\Omega}}_{\rm out}$, respectively in the rotating frame of reference with constant angular velocity $\Omega\boldsymbol{k}$. These mean

that the inner and outer spheres are rotating with $\tilde{\boldsymbol{\Omega}}_{\rm in} + \Omega\boldsymbol{k}$ and $\tilde{\boldsymbol{\Omega}}_{\rm out} + \Omega\boldsymbol{k}$, respectively in the inertial frame of reference.

Using the same scales introduced in Sec. 3.2, the non-dimensional governing equations for the deviations from the state of rest in the rotating frame of reference moving with the constant angular velocity $\Omega\boldsymbol{k}$ are as follows:

$$\nabla \cdot \boldsymbol{U} = 0, \tag{4.1}$$

$$\frac{\partial \boldsymbol{U}}{\partial t} + (\boldsymbol{U}\cdot\nabla)\boldsymbol{U} + \tau\boldsymbol{k}\times\boldsymbol{U} = -\nabla\pi + \Theta\boldsymbol{r} + \Delta\boldsymbol{U}, \tag{4.2}$$

$$P\left(\frac{\partial\Theta}{\partial t} + (\boldsymbol{U}\cdot\nabla)\Theta\right) = R\,\boldsymbol{U}\cdot\boldsymbol{r} + \nabla^2\Theta, \tag{4.3}$$

where $\boldsymbol{U}$ is the non-dimensional velocity and Θ is the non-dimensional temperature deviation from the basic state $T_s(r)$ (2.1). The equation of motions of the inner and outer spheres are

$$I_{\rm in}\frac{d\tilde{\boldsymbol{\Omega}}_{\rm in}}{dt} = \boldsymbol{N}_{\rm in}(\boldsymbol{U}), \tag{4.4}$$

$$I_{\rm out}\frac{d\tilde{\boldsymbol{\Omega}}_{\rm out}}{dt} = \boldsymbol{N}_{\rm out}(\boldsymbol{U}), \tag{4.5}$$

where $I_{\rm in}$ and $I_{\rm out}$ are the non-dimensional inertial moments of the inner and outer spheres, respectively, and $\boldsymbol{N}_{\rm in}$ and $\boldsymbol{N}_{\rm out}$ are the non-dimensional torques operating on the inner and outer spheres, respectively. Here we assume the centers of both spheres always keep the same position. The non-dimensional parameters in the equations are,

$$\tau = \sqrt{T} = \frac{2\Omega d^2}{\nu},\quad P = \frac{\nu}{\kappa},\quad R = \frac{\alpha\beta\gamma d^6}{\nu\kappa},\quad I_{\rm in} = \frac{I^*_{\rm in}}{\rho d^5},\quad I_{\rm out} = \frac{I^*_{\rm out}}{\rho d^5}, \tag{4.6}$$

where T is the Taylor number, P the Prandtl number, R the Rayleigh number, $I^*_{\rm in}$ and $I^*_{\rm out}$ the dimensional inertial moments of the inner and outer spheres, respectively.

We choose the boundary condition of the velocity as no-slip and impermeable on both spheres, and the temperature disturbance is fixed to zero at the inner and outer spheres:

$$\boldsymbol{U}(r = r_{\rm in},\theta,\phi,t) = \tilde{\boldsymbol{\Omega}}_{\rm in}\times(r_{\rm in}\boldsymbol{e}_r),\quad \boldsymbol{U}(r = r_{\rm out},\theta,\phi,t) = \tilde{\boldsymbol{\Omega}}_{\rm out}\times(r_{\rm out}\boldsymbol{e}_r), \tag{4.7}$$

$$\Theta(r = r_{\rm in},\theta,\phi,t) = 0,\quad \Theta(r = r_{\rm out},\theta,\phi,t) = 0, \tag{4.8}$$

where $\boldsymbol{e}_r$ is the unit vector in the radial direction.

As is shown in Sec. 3.2, since the velocity field is solenoidal, it can be represented with the toroidal and poloidal potentials w and v as follows:

$$\boldsymbol{U} \equiv \nabla \times (\boldsymbol{r}(w + w_S)) + \nabla \times \{\nabla \times (\boldsymbol{r}v)\}, \tag{4.9}$$

where w_S is defined as

$$\begin{aligned} w_S(\boldsymbol{r}, \tilde{\boldsymbol{\Omega}}_{\rm in}(t), \tilde{\boldsymbol{\Omega}}_{\rm out}(t)) \equiv & -\frac{r_{\rm in}^3}{r_{\rm out}^3 - r_{\rm in}^3}\left(r - \frac{r_{\rm out}^3}{r^2}\right)\left(\boldsymbol{e}_r \cdot \tilde{\boldsymbol{\Omega}}_{\rm in}(t)\right) \\ & + \frac{r_{\rm out}^3}{r_{\rm out}^3 - r_{\rm in}^3}\left(r - \frac{r_{\rm in}^3}{r^2}\right)\left(\boldsymbol{e}_r \cdot \tilde{\boldsymbol{\Omega}}_{\rm out}(t)\right), \end{aligned} \tag{4.10}$$

which satisfies the above velocity boundary condition (4.7). Then the boundary conditions of v and w are

$$v = \frac{\partial v}{\partial r} = w = 0 \quad \text{at} \quad r = r_{\rm in},\ r_{\rm out}. \tag{4.11}$$

The governing equations of these potentials and Θ become

$$\begin{aligned} \frac{\partial}{\partial t}\left(\hat{L}_2 w\right) = & \left[\nabla^2 \hat{L}_2 + \tau\frac{\partial}{\partial \phi}\right] w - \tau \hat{Q} v + \left[\left(\nabla^2 - \frac{\partial}{\partial t}\right)\hat{L}_2 + \tau\frac{\partial}{\partial \phi}\right] w_S \\ & - \boldsymbol{r} \cdot [\nabla \times ((\boldsymbol{U} \cdot \nabla)\boldsymbol{U})], \end{aligned} \tag{4.12}$$

$$\begin{aligned} \frac{\partial}{\partial t}\left(\hat{L}_2 \nabla^2 v\right) = & \left[\nabla^2 \hat{L}_2 + \tau\frac{\partial}{\partial \phi}\right] \nabla^2 v + \tau \hat{Q} w - \hat{L}_2 \Theta + \tau \hat{Q} w_S \\ & - \boldsymbol{r} \cdot [\nabla \times \nabla \times ((\boldsymbol{U} \cdot \nabla)\boldsymbol{U})], \end{aligned} \tag{4.13}$$

$$P\frac{\partial \Theta}{\partial t} = R\hat{L}_2 v + \nabla^2 \Theta - P(\boldsymbol{U} \cdot \nabla)\Theta, \tag{4.14}$$

which is exactly same as the equations shown in Sec. 3.2 except for w_S. The operators $\hat{L}_2$ and $\hat{Q}$ are defined as eqs.(2.11) and (2.12), respectively.

We will fix the values of η and P as the standard value $\eta = 0.4$ and $P = 1$, and also fix τ as 500, which means the moderate rotation region, and vary the Rayleigh number in the range of $2.6 \times 10^4 \leq R \leq 3.4 \times 10^4$. The inertial moment of the inner sphere is set to be $I_{\rm in} = 8\pi r_{\rm in}^5/15 \simeq 0.22$, assuming that the density of the inner sphere is the same as that of fluid. The inertial moment of the outer sphere is set to be $I_{\rm out} = 100$, which is the simulated value of the inertial moment of the Earth's mantle.

In this chapter we investigate the behaviour of the convection patterns using numerical time integrations. We use the Galerkin-spectral method, which is shown in Sec.2.2. We also use the Crank-Nicolson scheme to the diffusion terms and use the second order Adams-Bashforth scheme for all other terms,

with the time step $\Delta t = 10^{-4}$. The truncation wavenumber of spherical harmonics L and the maximum degree of the Chebyshev polynomials N are set to both fixed to 42 in the standard calculations. The nonlinear terms in the governing equations are evaluated in the physical space and are converted back into the spectral space (the spectral transform method). The numbers of the grid points on the physical space are chosen as $(N_r, N_\theta, N_\phi) = (65, 64, 128)$ in order to eliminate the aliasing errors, where N_r, N_θ and N_ϕ the number of grid points in the radial, zenith (colatitudinal) and azimuthal (longitudinal) directions, respectively. At the initial state, both the spheres do not rotate in the rotating frame of reference with constant angular velocity $\Omega\boldsymbol{k}$, and the random temperature disturbance is added to the conductive state.

4.3 Results

4.3.1 Transition from equatorially symmetric pattern to equatorially asymmetric pattern

In this section we show the transition routes from equatorially symmetric convective solutions to equatorially asymmetric ones in the system allowing the rotation of both spheres and those in the co-rotating system in the range $2.7 \times 10^4 \leq R \leq 3.2 \times 10^4$. We especially focus on the property (QP^{S}, QP^{A}, C^{S} or C^{A}, which are defined below) of each obtained solution, and the typical convection patterns are described in the next section.

We should remark the definition of the equatorial symmetry, asymmetry and antisymmetry of the convective solutions. The convective solution $(\boldsymbol{U}, \Theta)$ can be decomposed uniquely into two parts, that is, $(\boldsymbol{U}, \Theta) = (\boldsymbol{U}^{\mathrm{S}}, \Theta^{\mathrm{S}}) + (\boldsymbol{U}^{\mathrm{Anti}}, \Theta^{\mathrm{Anti}})$ such that the first term (the second term) satisfies the following relations with the upper signature in each right hand side (with the lower signature in each RHS):

$$U_r(r, \theta, \phi) = \pm U_r(r, \pi - \theta, \phi), \tag{4.15}$$
$$U_\theta(r, \theta, \phi) = \mp U_\theta(r, \pi - \theta, \phi), \tag{4.16}$$
$$U_\phi(r, \theta, \phi) = \pm U_\phi(r, \pi - \theta, \phi), \tag{4.17}$$
$$\Theta(r, \theta, \phi) = \pm \Theta(r, \pi - \theta, \phi). \tag{4.18}$$

If a convective solution has only $(\boldsymbol{U}^{\mathrm{S}}, \Theta^{\mathrm{S}})$ part, we call this solution equatorially symmetric solution, denoted by superscript S. If a convective solution has only $(\boldsymbol{U}^{\mathrm{Anti}}, \Theta^{\mathrm{Anti}})$ part, we call this solution equatorially antisymmetric solution, denoted by superscript Anti. If a convective solution consists of

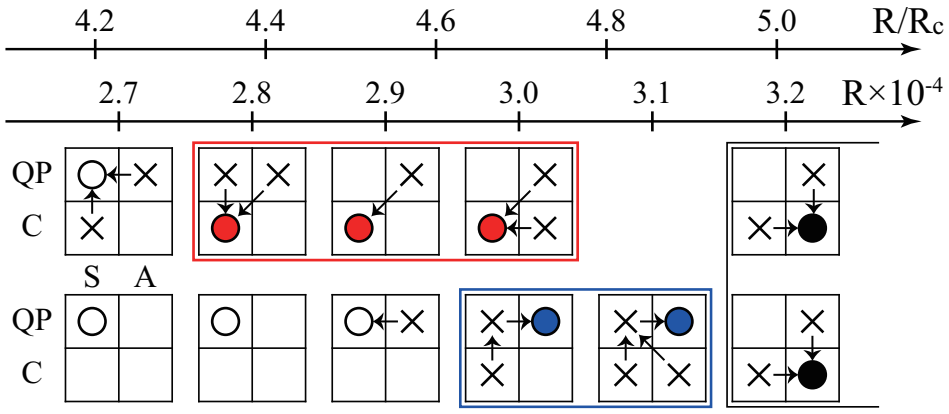

Figure 4.2: The property of the convective solution at each Rayleigh number $R = 2.7 \times 10^4$, 2.8×10^4, 2.9×10^4, 3.0×10^4, 3.1×10^4, 3.2×10^4, where $R_c = 6386.6056$ (shown in Table 2.1). The upper 7 panels show the properties of the convective solutions allowing the rotation of both spheres, while the lower 8 panels show those in the co-rotating system. Each panel shows the kind of the convective solution: the left upper box means the convective solutions is QP^{S}, the left lower box means C^{S}, the right upper box means QP^{A}, and the right lower box means C^{A}. The empty circles mean solutions are QP^{S}, circles filled with red mean solutions are C^{S}, circles filled with blue mean solutions are QP^{A}, and circles filled with black mean solutions are C^{A}. The crosses mean the solutions are only the transient state or are unstable and transit to other solutions along the arrows.

both the equatorially symmetric and antisymmetric part, we call this solution equatorially asymmetric solution, denoted by superscript A.

Figure 4.2 shows the property of the convective solution at each Rayleigh number R. Here we categorize the convection solutions into four kinds: equatorially symmetric quasi-periodic (or periodic) solution QP^{S}, equatorially asymmetric quasi-periodic (or periodic) solution QP^{A}, equatorially symmetric chaotic solution C^{S} and equatorially asymmetric chaotic solution C^{A}. The circle in Fig. 4.2 means that the property of each obtained solution does not change against small but finite-amplitude perturbations. On the other hand, the cross means that the property of the solution changes with time evolution (only a transient state), or the property of the solution changes to other properties against small perturbations (unstable solution). The arrow means transition direction of the solution denoted by a cross.

For example, let us focus on the upper leftmost panel in Fig. 4.2. In the system allowing the rotation of both spheres, we performed time integration

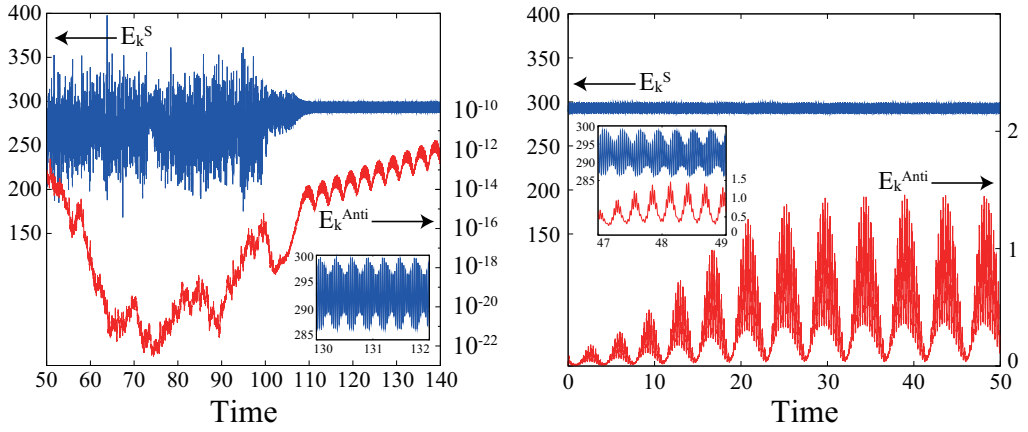

Figure 4.3: Time series of equatorially symmetric part of mean kinetic energy density E_k^{S} (blue line) and equatorially antisymmetric part of mean kinetic energy density E_k^{Anti} (red line) at $R = 3.1 \times 10^4$ in the co-rotating system. In the left panel the left longitudinal axis shows the magnitude of E_k^{S} while the right one shows the magnitude of E_k^{Anti} with log scale. The inset in the left figure is the enlarged drawing of the time series of E_k^{S} for $130 \leq t \leq 132$. The right figure also shows the time series of E_k^{S} and E_k^{Anti} long time after $t = 140$. In the right panel the left longitudinal axis shows the magnitude of E_k^{S} while the right one shows the magnitude of E_k^{Anti} with linear scale. The inset in the right figure is the enlarged drawing of the time series of E_k^{S} and E_k^{Anti} for $47 \leq t \leq 49$.

at $R = 2.7 \times 10^4$ with the initial condition being the obtained solution C^{S} at $R = 2.8 \times 10^4$, and the solution converged to QP^{S}. Therefore the cross is written in the lower left box, C^{S}, at $R = 2.7 \times 10^4$ and the arrow is written from the lower left box (C^{S}) to the upper left box (QP^{S}).

As an another example, Fig. 4.3 shows the time series of equatorially symmetric part of mean kinetic energy density E_k^{S} and equatorially antisymmetric part of mean kinetic energy density E_k^{Anti} at $R = 3.1 \times 10^4$ for $t \geq 50$ in the co-rotating system. Note that the rotating frame of reference rotates $\tau/(4\pi) \simeq 40$ times in 1 non-dimensional time. Here E_k^{S} and E_k^{Anti} are defined as the following equations, respectively:

$$E_k^{\mathrm{S}} \equiv \frac{1}{V_{\mathrm{shell}}} \int_{V_{\mathrm{shell}}} \frac{1}{2} \left| \boldsymbol{U}^{\mathrm{S}} \right|^2 dV, \tag{4.19}$$

$$E_k^{\mathrm{Anti}} \equiv \frac{1}{V_{\mathrm{shell}}} \int_{V_{\mathrm{shell}}} \frac{1}{2} \left| \boldsymbol{U}^{\mathrm{Anti}} \right|^2 dV, \tag{4.20}$$

while the entire mean kinetic energy density $E_k = E_k^{\mathrm{S}} + E_k^{\mathrm{Anti}}$ because $\int_{V_{\mathrm{shell}}} \boldsymbol{U}^{\mathrm{S}} \cdot \boldsymbol{U}^{\mathrm{Anti}} dV = 0$. The initial condition of the time series in Fig. 4.3 is a small temperature disturbance in addition to the conductive rest state with no flow in the rotating frame of reference with the angular velocity $\Omega \boldsymbol{k}$. After some decades of non-dimensional time, the antisymmetric part of the kinetic energy density E_k^{Anti} decays exponentially and becomes less than 10^{-10} for $t > 45$ (not shown), while the symmetric part of the kinetic energy density E_k^{S} keeps chaotic. We consider the convective solution for $50 \leq t \leq 100$ to be C^{S} because E_k^{S} keeps chaotic while E_k^{Anti} keeps less than $10^{-14} \times E_k^{\mathrm{S}}$, very small. Then, E_k^{S} starts oscillating for $t > 110$, so we consider C^{S} is only the transient state and the convective solution becomes QP^{S} (shown as the cross at the lower left box (C^{S}) and as the arrow toward the upper left box (QP^{S}) in lower fifth panel in Fig. 4.2). For $t > 110$ E_k^{Anti} also grows exponentially with oscillation, and after a long time, E_k^{Anti} converges to quasi-periodic oscillation while E_k^{S} keeps quasi-periodic oscillation (shown in the right panel in Fig. 4.3). Therefore, QP^{S} is unstable and the convective solution converges to QP^{A} (shown as the cross at the upper left box (QP^{S}) and as the arrow toward the upper right box (QP^{A}) in lower fifth panel in Fig. 4.2).

From Fig. 4.2, we summarize the transition from an equatorially symmetric solution to an equatorially asymmetric solution in the system allowing the rotation of both spheres and in the co-rotating system. In the system allowing the rotation of both spheres, as the Rayleigh number is increased, the property of the obtained solution changes as the following order: $\mathrm{QP}^{\mathrm{S}} \rightarrow \mathrm{C}^{\mathrm{S}} \rightarrow \mathrm{C}^{\mathrm{A}}$. The transition Rayleigh number from QP^{S} to C^{S} is between $R = 2.7 \times 10^4$ and 2.8×10^4, while that from C^{S} to C^{A} is between $R = 3.0 \times 10^4$ and 3.2×10^4. Note that, in the system allowing the rotation of only the inner sphere, the property of the obtained solution changes exactly same as the above order as the Rayleigh number is increased. Moreover, both the transition Rayleigh numbers from QP^{S} to C^{S} and from C^{S} to C^{A} are in the same regions, respectively, as those in the system allowing the rotation of both spheres. On the other hand, in the co-rotating system, as the Rayleigh number is increased, the property of the obtained solution changes as the following order: $\mathrm{QP}^{\mathrm{S}} \rightarrow \mathrm{QP}^{\mathrm{A}} \rightarrow \mathrm{C}^{\mathrm{A}}$. The transition Rayleigh number from QP^{S} to QP^{A} is between $R = 2.9 \times 10^4$ and 3.0×10^4, while that from QP^{A} to C^{A} is between $R = 3.1 \times 10^4$ and 3.2×10^4.

Note also that, in both systems, the critical Rayleigh number of the antisymmetric pattern $R_c^{\mathrm{Anti}} = 14023$ and the critical azimuthal wavenumber $m_c = 5$. Therefore we conclude that the antisymmetric instability of the conductive state is not related to the emergence of the equatorial asymmetric patterns discussed in this section.

Compared the properties of the obtained solutions in the system allow-

ing the rotation of both spheres with those in the co-rotating system in the region $2.6 \times 10^4 \leq R \leq 3.4 \times 10^4$, we found that the routes from the equatorially symmetric convective solutions to the equatorially asymmetric ones are completely different. We found the two important differences:

1. we could not find any QP^{A} solutions, and find C^{S} solutions instead in the system allowing the rotation of both spheres,

2. the chaotic solution appears at smaller Rayleigh number in the system allowing the rotation of both spheres (C^{S} appears at $R = 2.8 \times 10^4$) than in the co-rotating system (C^{A} appears at $R = 3.2 \times 10^4$).

These differences suggest that both sphere rotations make QP^{S} and QP^{A} solutions unstable around $R = 3.0 \times 10^4$, and make the solutions chaotic. Taking it into consideration that the route from the equatorially symmetric solutions to the equatorially asymmetric ones in the system allowing only the inner sphere rotation is exactly same as that in the system allowing the rotation of both spheres, we consider that the effect of the inner sphere rotation to make solutions chaotic is larger than that of the outer sphere rotation in this parameter range.

4.3.2 Convection patterns around the transition region

In this section we show typical convection patterns in the system allowing the rotation of both spheres and in the co-rotating system at $R = 2.6 \times 10^4$, 3.0×10^4 and 3.4×10^4, around the transition region discussed in the previous section (Fig. 4.2).

Convection patterns at $R = 2.6 \times 10^4$

Figure 4.4 shows the typical time series of the mean kinetic energy densities, those of angular velocities of both spheres, the energy spectra and typical convection patterns at $R = 2.6 \times 10^4$ in the system allowing the rotation of both spheres. Figure 4.5 shows the typical time series of the mean kinetic energy densities, those of torques on both spheres, the energy spectra and typical convection patterns at $R = 2.6 \times 10^4$ in the co-rotating system. In both cases, E_k^{Anti} are exactly zero (not shown), and the perpendicular components of $\tilde{\boldsymbol{\Omega}}_{\mathrm{in}}$, $\tilde{\boldsymbol{\Omega}}_{\mathrm{out}}$ against the axis of rotation are also exactly zero (the left third and fourth panels in Fig. 4.4) in the system allowing both spheres rotation and the perpendicular components of $\boldsymbol{N}_{\mathrm{in}}$, $\boldsymbol{N}_{\mathrm{out}}$ against the axis of rotation are also exactly zero (the left third and fourth panels in Fig. 4.5).

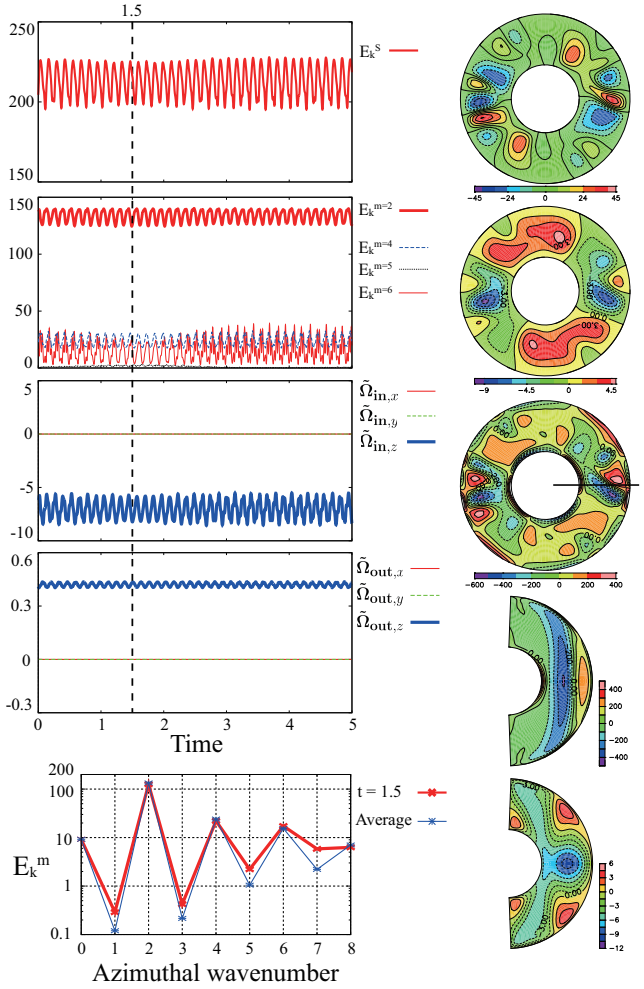

Figure 4.4: Time series of the mean kinetic energy densities, those of angular velocities of both spheres, the energy spectra and typical convection patterns at $R = 2.6 \times 10^4$ in the system allowing the rotation of both spheres. The left upper four panels show the time series: the equatorially symmetric part of the mean kinetic energy density E_k^{S}, the mean kinetic energy densities for each azimuthal wavenumbers E_k^m, the angular velocities of the inner sphere $\tilde{\boldsymbol{\Omega}}_{\mathrm{in}}$, and the angular velocities of the outer sphere $\tilde{\boldsymbol{\Omega}}_{\mathrm{out}}$, from top to bottom. The left lowermost panel shows the energy spectra E_k^m at $t = 1.5$ and the time averaged energy spectra $\overline{E_k^m}$. The right five panels show the convection patterns at $t = 1.5$: the radial component of the velocity U_r on the equatorial plane, the stream function on the equatorial plane $-r(\partial v/\partial\phi)$, the axial component of the vorticity $\omega_z = \boldsymbol{k} \cdot (\nabla \times \boldsymbol{U})$ on the equatorial plane, ω_z at the meridional section indicated by the black solid line in the above panel (right third panel), and the azimuthally averaged azimuthal velocity (mean zonal flow) $\langle U_\phi \rangle$, from top to bottom.

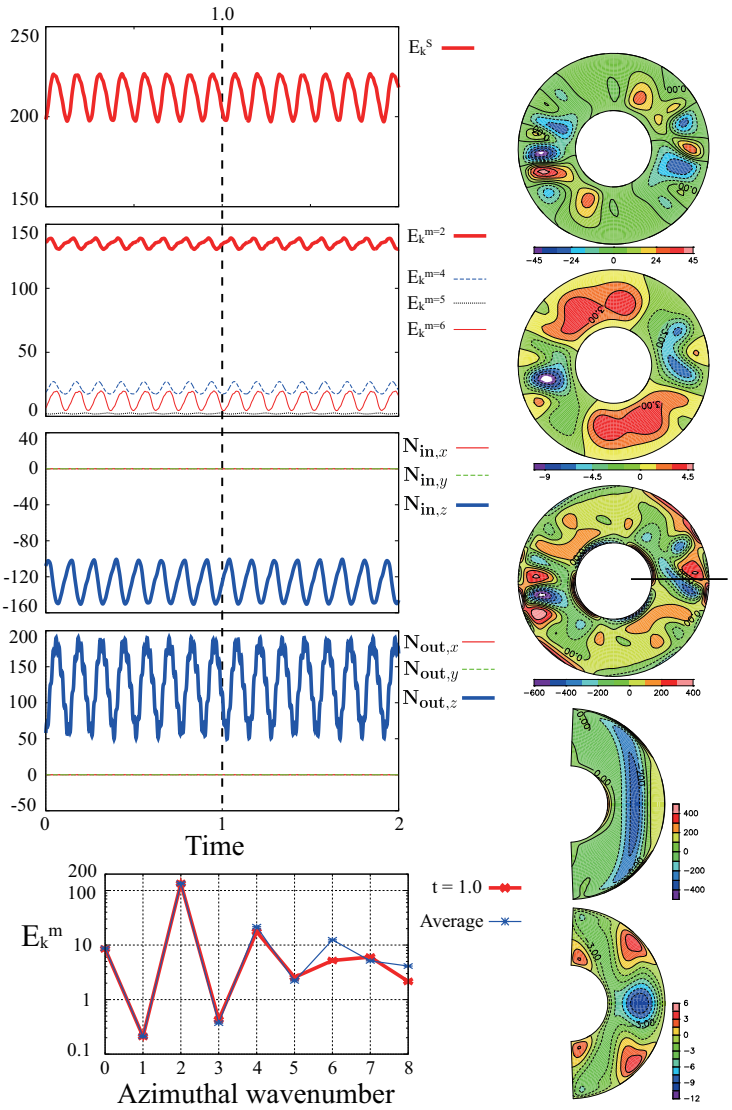

Figure 4.5: Time series of the mean kinetic energy densities, those of torques on both spheres, the energy spectra and typical convection patterns at $R = 2.6 \times 10^4$ in the co-rotating system. The left upper four panels show the time series: the equatorially symmetric part of the mean kinetic energy density E_k^{S}, the mean kinetic energy densities for each azimuthal wavenumbers E_k^m, the torque on the inner sphere $\boldsymbol{N}_{\mathrm{in}}$, and the torque on the outer sphere $\boldsymbol{N}_{\mathrm{out}}$, from top to bottom. The left lowermost panel shows the energy spectra E_k^m at $t = 1.0$ and the time averaged energy spectra $\overline{E_k^m}$. The right five panels show the convection patterns at $t = 1.0$, same as those at right five panels in Fig. 4.4.

Moreover, these all time series oscillate almost monotonically in bounded regions. Therefore, we conclude that these convective solutions are both QP^{S} (not shown in Fig. 4.2). Note that, the mean kinetic energy density for each azimuthal wavenumber E_k^m is defined as follows:

$$E_k^m \equiv \frac{1}{V_{\mathrm{shell}}} \int_{V_{\mathrm{shell}}} \frac{1}{2} \left| \boldsymbol{U}^m \right|^2 dV, \tag{4.21}$$

where $\boldsymbol{U}^m$ means the velocity field which has m-fold symmetry in the azimuthal direction, and V_{shell} is the volume of the spherical shell. The total mean kinetic energy density $E_k = \sum_{m=0}^{L} E_k^m$, because $\int_{V_{\mathrm{shell}}} \boldsymbol{U}^m \cdot \boldsymbol{U}^{m'} = 0$ for $m \neq m'$.

Compared the convective solution in the system allowing the rotation of both spheres with that in the co-rotating system, these are qualitatively similar in some aspects, which are described below, despite the inner and outer sphere rotation: $\tilde{\Omega}_{\mathrm{in},z} = -7.0 \pm 1.5$ (the left third panel in Fig. 4.4), at most 3.4 % against the rotation rate of the reference frame $\Omega = \tau/2 = 250$.

The time averaged energy spectra E_k^m of convection pattern is qualitatively similar in the range $0 \leq m \leq 5$, and especially $E_k^{m=2}$ is the dominant part of the kinetic energy density in both cases. Actually $\overline{E_k^{m=2}}/\overline{E_k} = 134/213 \simeq 63\%$ in the system allowing the rotation of both spheres and $\overline{E_k^{m=2}}/\overline{E_k} = 135/212 \simeq 64\%$ in the co-rotating system, where $\bar{\cdot}$ means the time averaged value. $\overline{E_k^{m=4}}/\overline{E_k}$ is only about 10% in both cases even though the critical modes have four-fold symmetry in the azimuthal direction and the TW4 solutions first bifurcate from the conductive state at the critical point (Fig. 1.1). This tendency is similar to the results in Ardes *et al.*, who found a large convection pattern in the azimuthal direction appears as the Rayleigh number is increased, while their control parameters and boundary conditions are totally different from those in this case.

While the long period oscillation occurs only in the system allowing the rotation of both spheres ($T \simeq 5.4$), the dominant frequency of these four time series in the system allowing the rotation of both spheres shown in Fig. 4.4 is almost same as that in the co-rotating system shown in Fig. 4.5: $\omega \simeq 48.3$ in the system allowing the rotation of both spheres and $\omega \simeq 49.0$ in the co-rotating system.

The convection patterns are qualitatively similar. Especially, the convection patterns in the equatorial plane appear to have almost two-fold symmetry in the azimuthal direction (the right first, second and third panels in Fig. 4.4 and those in Fig. 4.5), which is consistent with the fact that $E_k^{m=2}$ is the dominant part of the kinetic energy density. The strong negative vorticity regions are localized in two parts and the peaks of these exist at the outer

part of the shell on the equatorial plane (the right third panel in Fig. 4.4 and that in Fig. 4.5). The vortex tubes elongate in the direction of the axis of rotation (the right fourth panel in Fig. 4.4 and that in Fig. 4.5), which are the typical structures of the critical modes in rapidly rotating cases (lowermost right two panels in Fig. 2.4).

The distributions of the mean zonal flows are also qualitatively similar (the right lowermost panel in Fig. 4.4 and that in Fig. 4.5) except near the inner sphere, because of the inner sphere rotation. The strong retrograde zonal flow locates in the middle of the shell on the equatorial plane and is localized there while the strong prograde zonal flows locate in the vicinity of the poles near the inner sphere and in the mid-latitude near the outer sphere.

The convection patterns shown in Figs. 4.4 and 4.5 gradually propagate in the azimuthal direction with small oscillations. The averaged propagating velocity $\overline{v_p} \simeq -2.0$ in the system allowing the rotation of both spheres, while $\overline{v_p} \simeq -1.5$ in the co-rotating system. Both the propagating velocities have negative value, that is, the convection patterns propagate in the retrograde direction (clockwise direction in Figs. 4.4 and 4.5). However, the magnitude of the propagating velocity in the system allowing the rotation of both spheres is larger than that in the co-rotating system by about 33%.

Convection patterns at $R = 3.0 \times 10^4$

Figure 4.6 shows the typical time series of the mean kinetic energy densities, those of angular velocities of both spheres, the energy spectra and typical convection patterns at $R = 3.0 \times 10^4$ in the system allowing the rotation of both spheres. In this system, E_k^{Anti} are exactly zero (not shown), and the perpendicular components of $\tilde{\boldsymbol{\Omega}}_{\mathrm{in}}$, $\tilde{\boldsymbol{\Omega}}_{\mathrm{out}}$ against the axis of rotation are also exactly zero (the left third and fourth panels in Fig. 4.6). However, all these time series have chaotic fluctuations. Therefore we conclude that this convective solution is C^{S} (Fig. 4.2).

It is found that $E_k^{m=2}$ is the dominant part of the mean kinetic energy density for over half of the time series shown at the left second panel in Fig. 4.6, while $E_k^{m=2}$ decreases and the other E_k^m, such as $E_k^{m=3}$, $E_k^{m=4}$ and $E_k^{m=5}$, increase intermittently. These typical energy spectra E_k^m are shown in the left lowermost panel in Fig. 4.6. This panel shows that $E_k^{m=2}$ is the dominant part of the kinetic energy density at $t = 2.0$ ($E_k^{m=2}/E_k = 141/245 \simeq 58\%$) while there is no dominant part and the energy spectra E_k^m become flat at $t = 0.2$. The convection patterns also show this tendency: when $t = 2.0$ the convection patterns generally have two-fold symmetry in the azimuthal direction (the right first, second and third panels in Fig. 4.6). On the other hand, when $t = 0.2$, the convection patterns seem to consist of mainly $m = 4$

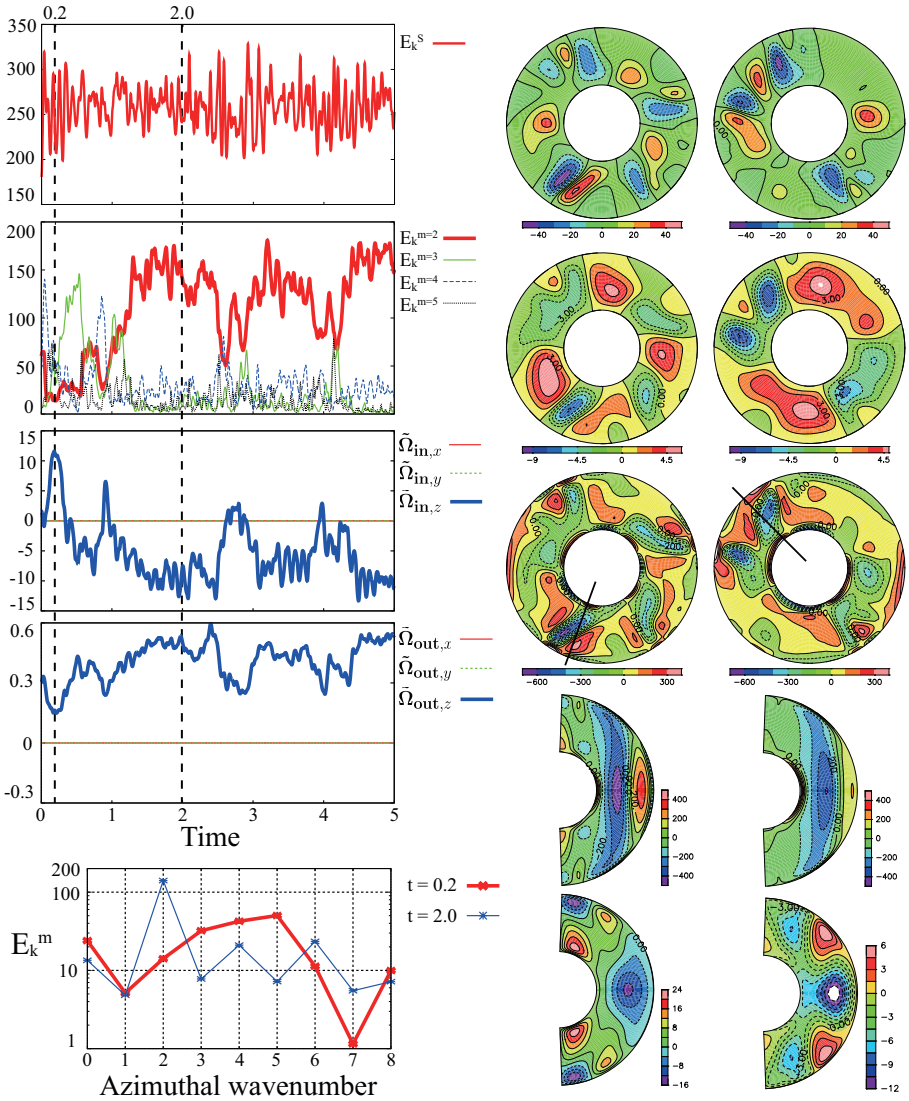

Figure 4.6: Time series of the mean kinetic energy densities, those of angular velocities of both spheres, the energy spectra and typical convection patterns at $R = 3.0 \times 10^4$ in the system allowing the rotation of both spheres, same as Fig. 4.4. The middle and right five panels show the convection patterns at $t = 0.2$ and $t = 2.0$, respectively, same as the right five panels in Fig. 4.4.

and $m = 5$ modes in the azimuthal direction. Note that, the vortex tubes always elongate in the direction of the axis of rotation (the middle and right fourth panels in Fig. 4.6), whenever $E_k^{m=2}$ is dominant or not.

We found that the rotation rate of the inner sphere $\tilde{\Omega}_{\mathrm{in},z}$ keeps negative for almost all time in $0 \leq t \leq 5$, but sometimes become positive intermittently around $t = 0.2$, 1, 2.8 and 4. The amplitude of the inner sphere rotation rate is that $-13.3 \lesssim \tilde{\Omega}_{\mathrm{in},z} \lesssim +11.6$, which is at most 5.3% against the rotation rate of the reference frame. On the other hand, the rotation of the outer sphere $\tilde{\Omega}_{\mathrm{out},z}$ keeps positive for all time in $0 \leq t \leq 5$, but the amplitude is that $+0.15 \lesssim \tilde{\Omega}_{\mathrm{in},z} \lesssim +0.60$, relatively small compared with $\tilde{\Omega}_{\mathrm{in},z}$ because of the large inertial moment of the outer sphere.

Note that, $\tilde{\Omega}_{\mathrm{in},z}$ keeps about -10 with fluctuations and $\tilde{\Omega}_{\mathrm{out},z}$ also keeps about $+0.5$ with fluctuations when $E_k^{m=2}$ is the dominant part of the mean kinetic energy density, that is, $1.5 \lesssim t \lesssim 2.3$, $3 \lesssim t \lesssim 4$ and $4.5 \lesssim t \lesssim 5$. On the other hand, when $E_k^{m=2}$ suddenly decreases and the other parts of the mean kinetic energy density increases, $\tilde{\Omega}_{\mathrm{in},z}$ increases and also $\tilde{\Omega}_{\mathrm{out},z}$ decreases rapidly. This sudden acceleration of the inner sphere rotation and the simultaneous deceleration of the outer sphere rotation can be understood as the change of the structure of the mean zonal flow. Actually when $t = 2.0$ ($E_k^{m=2}$ is dominant), the prograde zonal flows locate near the mid-latitude near the outer sphere while the retrograde zonal flows locate almost all the region near and inside the tangential cylinder and also locate on the equatorial plane near the outer sphere. On the other hand, when $t = 0.2$, the strong prograde zonal flows locate in the vicinity of the poles near the inner sphere while the strong retrograde zonal flows locate in the vicinity of the poles near the outer sphere and also locate on the equatorial plane near the outer sphere. The strong prograde zonal flows near the inner sphere accelerate the inner sphere to be the positive value.

Figure 4.7 shows the typical time series of the mean kinetic energy densities, those of torques on both spheres, the energy spectra and typical convection patterns at $R = 3.0 \times 10^4$ in the co-rotating system. In this system, E_k^{Anti} are non-zero, and the perpendicular components of $\tilde{\boldsymbol{\Omega}}_{\mathrm{in}}$, $\tilde{\boldsymbol{\Omega}}_{\mathrm{out}}$ against the axis of rotation are also non-zero (the left third and fourth panels in Fig. 4.7). Moreover, all these time series oscillate in bounded regions. Therefore we conclude that this convective solution is QP^{A} (Fig. 4.2).

However, it is found that the antisymmetric part of the mean kinetic energy density E_k^{Anti} is very small compared with the symmetric part of that E_k^{S} ($\overline{E_k^{\mathrm{Anti}}}/\overline{E_k^{\mathrm{S}}} = 2.05/274 \simeq 0.75\%$). The perpendicular components of the torques on the inner sphere $N_{\mathrm{in},x}$ and $N_{\mathrm{in},y}$ are also very small compared with the axial component of that $N_{\mathrm{in},z}$ ($\max(|N_{\mathrm{in},x}|)/|\overline{N_{\mathrm{in},z}}| = 9.3/160 \simeq 6\%$). On

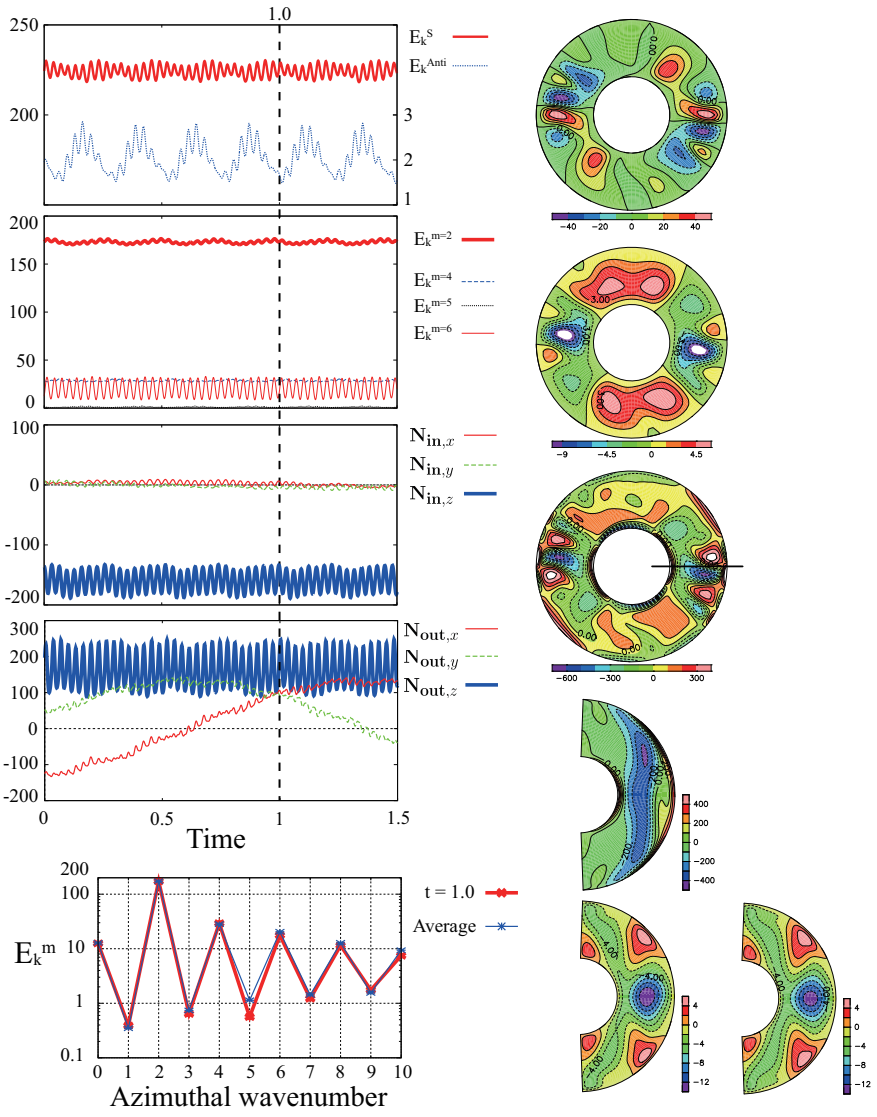

Figure 4.7: Time series of the mean kinetic energy densities, those of torques on both spheres, the energy spectra and typical convection patterns at $R = 3.0 \times 10^4$ in the co-rotating system, same as Fig. 4.5. The middle five panels show the typical convection patterns at $t = 1.0$, same as Fig. 4.5. The right lowermost panel show the distribution of the time averaged mean zonal flow $\overline{\langle u_\phi \rangle}$. Note that the time series of the antisymmetric part of the mean kinetic energy density E_k^{Anti} is also shown in the left uppermost panel, whose right longitude shows the magnitude of E_k^{Anti}.

the other hand, those of the torques on the outer sphere $N_{\mathrm{out},x}$ and $N_{\mathrm{out},y}$ are nearly same magnitude compared with the axial component of that N_{out}, z ($\max(|N_{\mathrm{out},x}|)/|\overline{N_{\mathrm{out},z}}| = 144/160 \simeq 90\%$).

The convection patterns are also equatorially asymmetric at $t = 1.0$, shown at the middle fourth and fifth panels in Fig. 4.7, but the asymmetry is very small and these convection patterns appear to be almost equatorially symmetric. Moreover, the time averaged mean zonal flow, which is shown at the rightmost lower panel in Fig. 4.7, appear to be equatorially symmetric.

It is also found that $E_k^{m=2}$ is the dominant part of kinetic energy density in this case ($\overline{E_k^{m=2}}/\overline{E_k} = 173/276 \simeq 63\%$). This is consistent with the fact that the convection patterns in the equatorial plane at $t = 1.0$ also appear to have almost two-fold symmetry in the azimuthal direction, which is shown at the middle first, second and third panels in Fig. 4.7. The strong negative vorticity regions are localized in two parts and the peaks of these exist at the outer part of the shell on the equatorial plane (the middle third panel in Fig. 4.7). The vortex tubes still elongate in the direction of the axis of rotation in spite of the equatorial asymmetry, shown at the middle fourth panel in Fig. 4.7. These convection patterns are qualitatively similar to those of QP^{S} at $R = 2.6 \times 10^4$ in the co-rotating system, shown in Fig. 4.5.

This convection pattern gradually propagates in the azimuthal direction, and the time averaged propagating velocity $\overline{v_p} \simeq -2.1$, which means the patterns propagate in the retrograde (clockwise) direction. The magnitude of this propagating velocity is larger than that at $R = 2.6 \times 10^4$ in the co-rotating system ($\overline{v_p} \simeq -1.5$). This propagating period can be confirmed by the period of the long time oscillation of the perpendicular components of the torques on the inner and outer spheres against the axis of rotation $N_{\mathrm{in},x}$, $N_{\mathrm{in},y}$, $N_{\mathrm{out},x}$ and $N_{\mathrm{out},y}$ ($T \simeq 3.0$).

However, the dominant frequency of all the time series of this stable QP^{A} shown in Fig. 4.7 is that $\omega \simeq 195$, which is larger that that of stable QP^{S} at $R = 2.6 \times 10^4$ in the co-rotating system ($\omega \simeq 49.0$).

Convection patterns at $R = 3.4 \times 10^4$

Figure 4.8 shows the typical time series of the mean kinetic energy densities, those of angular velocities of both spheres, the energy spectra and typical convection patterns at $R = 3.4 \times 10^4$ in the system allowing the rotation of both spheres, and Fig. 4.9 shows those at $R = 3.4 \times 10^4$ in the co-rotating system. In both cases, E_k^{Anti} are non-zero, and the perpendicular components of $\tilde{\boldsymbol{\Omega}}_{\mathrm{in}}$, $\tilde{\boldsymbol{\Omega}}_{\mathrm{out}}$ against the axis of rotation are also non-zero (the left third and fourth panels in Fig. 4.8 and those in Fig. 4.9). Moreover, all these time series have chaotic fluctuations in both cases. Therefore we conclude that

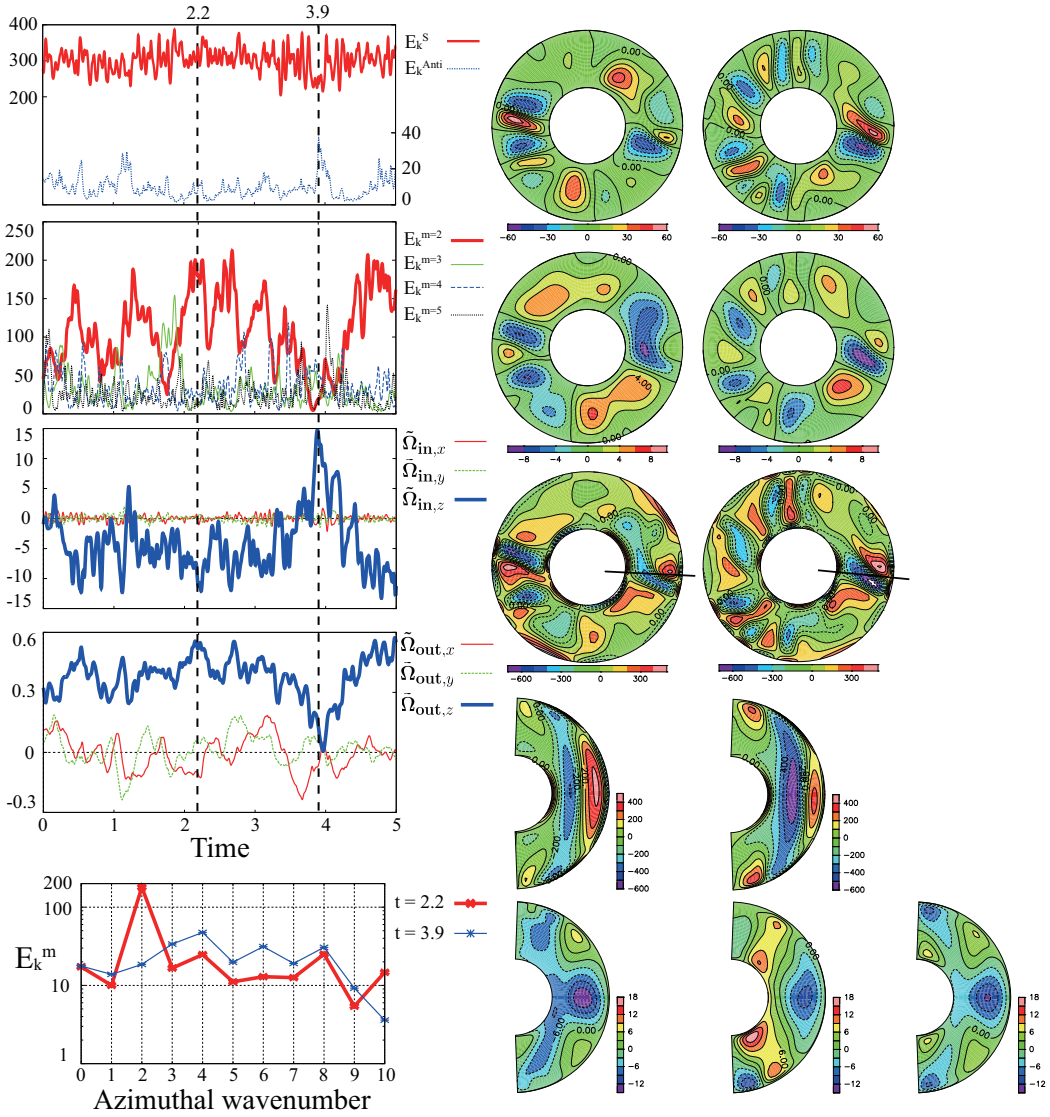

Figure 4.8: Time series of the mean kinetic energy densities, those of angular velocities of both spheres, the energy spectra and typical convection patterns at $R = 3.4 \times 10^4$ in the system allowing the rotation of both spheres, same as Fig. 4.4. The five panels at the second and third columns show the convection patterns at $t = 2.2$ and $t = 3.9$, respectively, same as the right five panels in Fig. 4.4. The rightmost lower panel shows the time averaged mean zonal flow. Note that the time series of the antisymmetric part of the mean kinetic energy density E_k^{Anti} is also shown in the left uppermost panel, whose right longitude shows the magnitude of E_k^{Anti}.

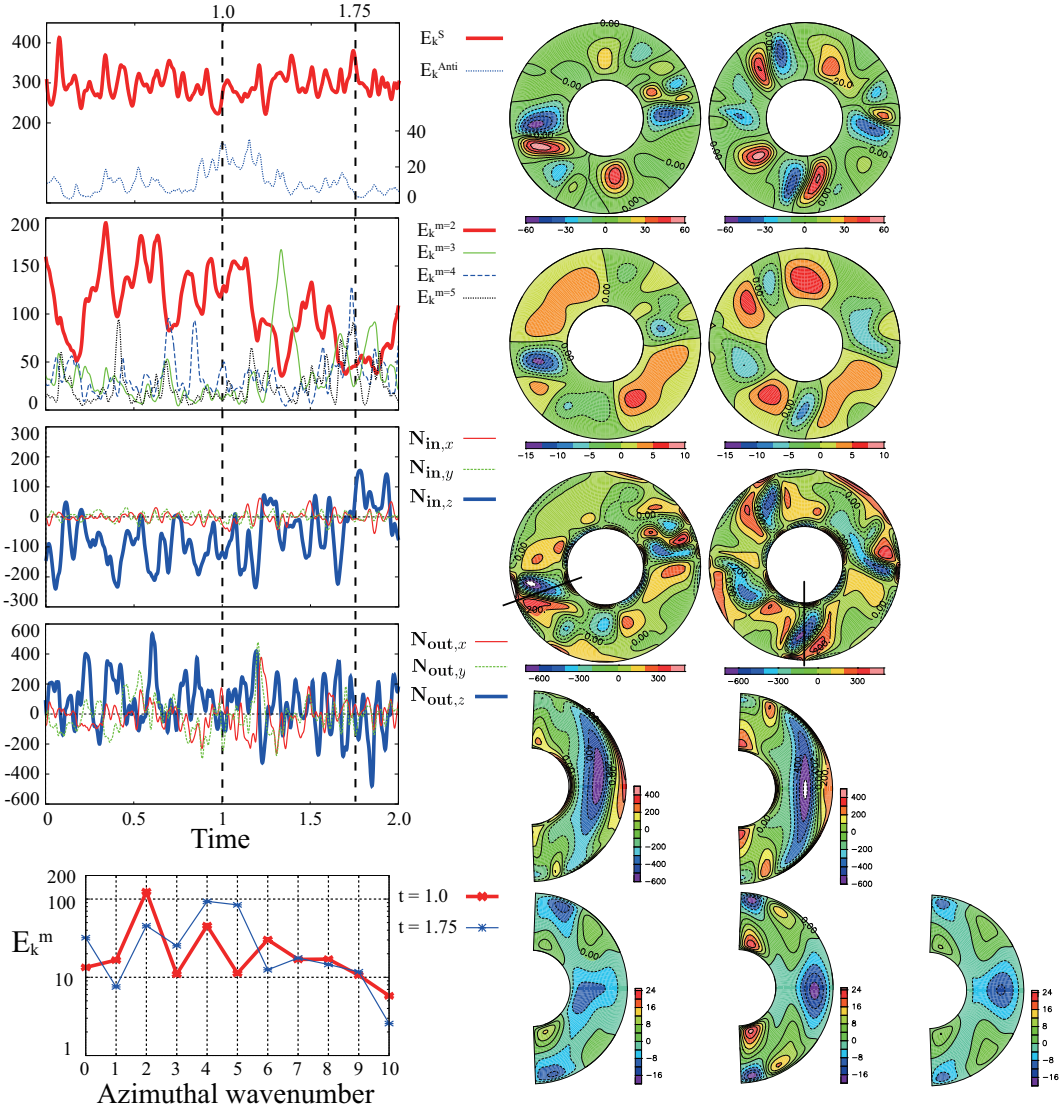

Figure 4.9: Time series of the mean kinetic energy densities, those of torques on both spheres, the energy spectra and typical convection patterns at $R = 3.4 \times 10^4$ in the co-rotating system, same as Fig. 4.5. The five panels at the second and third columns show the convection patterns at $t = 1.0$ and $t = 1.75$, respectively, same as the right five panels in Fig. 4.5. The rightmost lower panel shows the time averaged mean zonal flow. Note that the time series of the antisymmetric part of the mean kinetic energy density E_k^{Anti} is also shown in the left uppermost panel, whose right longitude shows the magnitude of E_k^{Anti}.

these convective solutions are both $\mathrm{C^A}$ (not shown in Fig. 4.2).

However, it is found in each case that the antisymmetric part of the mean kinetic energy density E_k^{Anti} is still small compared with the symmetric part of that E_k^{S}, but the ratio is large compared with that at $R = 2.6 \times 10^4$: $\max(E_k^{\mathrm{Anti}})/\overline{E_k^{\mathrm{S}}} = 37.2/300 \simeq 12\%$ in the system allowing the rotation of both spheres, and $\max(E_k^{\mathrm{Anti}})/\overline{E_k^{\mathrm{S}}} = 39.4/295 \simeq 13\%$ in the co-rotating system. The perpendicular components of the rotation rate of the inner sphere $\tilde{\Omega}_{\mathrm{in},x}$ and $\tilde{\Omega}_{\mathrm{in},y}$ are relatively still small compared with the axial component of that $\tilde{\Omega}_{\mathrm{in},z}$ in the system allowing the rotation of both spheres: $|\tilde{\Omega}_{\mathrm{in},x}|/|\tilde{\Omega}_{\mathrm{in},z}| \sim 10 - 20\%$ except near the transition time of the signature of $\tilde{\Omega}_{\mathrm{in},z}$. The perpendicular components of the torque on the inner sphere $N_{\mathrm{in},x}$ and $N_{\mathrm{in},y}$ are also relatively still small compared with the axial component of that $N_{\mathrm{in},z}$: $|N_{\mathrm{in},x}|/|N_{\mathrm{in},z}| \sim 10 - 30\%$ except the region around the transition time of the signature of $N_{\mathrm{in},z}$. On the other hand, the perpendicular components of the rotation rate of the outer sphere $\tilde{\Omega}_{\mathrm{out},x}$ and $\tilde{\Omega}_{\mathrm{out},y}$ are relatively large compared with the axial component of that $\tilde{\Omega}_{\mathrm{out},z}$ in the system allowing the rotation of both spheres: $|\tilde{\Omega}_{\mathrm{out},x}|/|\tilde{\Omega}_{\mathrm{out},z}| \sim 20 - 40\%$ except for the region around $t = 4.0$. The perpendicular components of the torque on the outer sphere $N_{\mathrm{out},x}$ and $N_{\mathrm{out},y}$ are relatively large compared with the axial component of that $N_{\mathrm{out},z}$ in the co-rotating system: $|N_{\mathrm{out},x}|/|N_{\mathrm{out},z}| \sim 50\%$.

Convection patterns are also equatorially asymmetric, shown at the fourth and fifth panels at the second and third columns in Fig. 4.8 and in Fig. 4.9. These asymmetries are both relatively large compared with that at $R = 3.0 \times 10^4$ in the co-rotating system, which is consistent with the fact that the ratio $E_k^{\mathrm{Anti}}/E_k^{\mathrm{S}}$ is larger than that at $R = 3.0 \times 10^4$ in the co-rotating system. However, the time averaged mean zonal flows, which are shown at the rightmost lower panel in Fig. in Fig. 4.8 and in Fig. 4.9, appear to be equatorially symmetric patterns.

It is found that, in both cases, $E_k^{m=2}$ is the dominant part of the mean kinetic energy density in some parts of the time series shown at the left second panel in Fig. 4.8 and in Fig. 4.9. Note that the intermittent increasing of the other E_k^m occurs more frequently than that of $\mathrm{C^S}$ at $R = 3.0 \times 10^4$ in the system allowing the rotation of both spheres. These typical energy spectra E_k^m, which are shown in the left lowermost panel in Fig. 4.8 and in Fig. 4.9, show that $E_k^{m=2}$ is the dominant part of the kinetic energy density at $t = 2.2$ in the system allowing the rotation of both spheres ($E_k^{m=2}/E_k = 180/346 \simeq 52\%$) and at $t = 1.0$ in the co-rotating system ($E_k^{m=2}/E_k = 124/314 \simeq 39\%$). When $t = 3.9$ in the system allowing the rotation of both spheres, there is no dominant part of E_k^m and E_k^m broads in the range $0 \leq m \leq 8$, and when $t = 1.75$ in the co-rotating system, $E_k^{m=4}$ and $E_k^{m=5}$ are the dominant parts

of E_k^m ($(E_k^{m=4} + E_k^{m=5})/E_k = (93.4 + 84.3)/361 \simeq 49\%$).

The convection patterns also show this tendency: when $t = 2.2$ in the system allowing the rotation of both spheres and when $t = 1.0$ in the co-rotating system, the convection patterns generally have two-fold symmetry in the azimuthal direction (the first, second and third panels at the second column in Fig. 4.8 and those in Fig. 4.9). On the other hand, when $t = 3.9$ in the system allowing the rotation of both spheres the convection patterns seem to consist of mainly $m = 4$ and $m = 6$ modes in the azimuthal direction, and when $t = 1.75$ in the co-rotating system, those seem to consist of mainly $m = 4$ and $m = 5$ modes in the azimuthal direction. Note that, the vortex tubes still always elongate in the direction of the axis of rotation (the fourth panels at the second and third columns in Fig. 4.8 and those in Fig. 4.9), whenever $E_k^{m=2}$ is dominant or not.

We also found that, in the system allowing the rotation of both spheres, the rotation rate of the inner sphere $\tilde{\Omega}_{\mathrm{in},z}$ keeps negative for almost all time in $0 \leq t \leq 5$, but sometimes become positive intermittently (shown at the third panel of the first column in Fig. 4.8). The amplitude of the inner sphere rotation rate is that $-13.3 \lesssim \tilde{\Omega}_{\mathrm{in},z} \lesssim +14.7$, which is at most 5.9% against the rotation rate of the reference frame. This ratio is a little larger than that at $R = 3.0 \times 10^4$ in the system allowing the rotation of both spheres. The time average of the axial component of the inner sphere rotation $\overline{\tilde{\Omega}_{\mathrm{in},z}} = -3.2$, while $\overline{\tilde{\Omega}_{\mathrm{in},z}} = -5.2$, at $R = 3.0 \times 10^4$ ($\mathrm{C^S}$ solution). On the other hand, the rotation of the outer sphere $\tilde{\Omega}_{\mathrm{out},z}$ keeps positive for all time in $0 \leq t \leq 5$ and the time average $\overline{\tilde{\Omega}_{\mathrm{out},z}} = 0.36$ while $\overline{\tilde{\Omega}_{\mathrm{out},z}} = 0.41$ at $R = 3.0 \times 10^4$ ($\mathrm{C^S}$ solution).

As is seen the $\mathrm{C^S}$ solution at $R = 3.0 \times 10^4$, $\tilde{\Omega}_{\mathrm{in},z}$ keeps about -7 with fluctuations and $\tilde{\Omega}_{\mathrm{out},z}$ also keeps about $+0.4$ with fluctuations when $E_k^{m=2}$ is dominant. On the other hand, when $E_k^{m=2}$ suddenly decreases and the other parts of the mean kinetic energy density increases, $\tilde{\Omega}_{\mathrm{in},z}$ increases and also $\tilde{\Omega}_{\mathrm{out},z}$ decreases rapidly. This tendency can be also understood as the change of the structure of the mean zonal flow, as is discussed for $\mathrm{C^S}$ solution at $R = 3.0 \times 10^4$: when $t = 2.2$ the prograde zonal flows locate near the mid-latitude near the outer sphere while the retrograde zonal flows locate almost all the region near and inside the tangential cylinder and also locate on the equatorial plane near the outer sphere, while when $t = 3.9$ the strong prograde zonal flows locate in the vicinity of the poles near the inner sphere while the strong retrograde zonal flows locate in the vicinity of the poles near the outer sphere and also locate on the equatorial plane near the outer sphere.

It is also found that $\mathrm{C^A}$ solution at $R = 3.4 \times 10^4$ in the co-rotating system

has the same behaviour: when $E_k^{m=2}$ is dominant $N_{\mathrm{in},z}$ keeps negative (about -100), while when the other modes E_k^m increase $N_{\mathrm{in},z}$ becomes positive. This behaviour also can be understood as the change of the structure of the mean zonal flow, discussed in the above paragraph.

4.4 Conclusion and discussion

We have investigated the route from the equatorial symmetric pattern to the equatorial asymmetric pattern in the system allowing the rotation of both spheres and in the co-rotating system, under the impermeable, no-slip and fixed-temperature boundary conditions for the ratio of inner and outer radii of the shell $\eta = 0.4$, the Prandtl number $P = 1$, the rotation rate $\tau = 500$, the inertial moments of the inner and outer spheres $I_{\mathrm{in}} \simeq 0.22$ and $I_{\mathrm{out}} = 100$, respectively. We found that, as the Rayleigh number is increased in the range $2.7 \times 10^4 \leq R \leq 3.2 \times 10^4$, the convective solution transits as $\mathrm{QP^S} \to \mathrm{QP^A} \to \mathrm{C^A}$ in the co-rotating system, while that transits as $\mathrm{QP^S} \to \mathrm{C^S} \to \mathrm{C^A}$ in the system allowing the rotation of both spheres (Fig. 4.2): $\mathrm{QP^A}$ does not appear in the system allowing the rotation of both spheres and $\mathrm{C^S}$ does not appear in the co-rotating system. In the system allowing the rotation of only the inner sphere, the route is exactly same as that in the system allowing the rotation of both spheres, and the transition Rayleigh number from $\mathrm{QP^S}$ to $\mathrm{C^S}$ is $2.6 \times 10^4 < R < 2.7 \times 10^4$ and that from $\mathrm{C^S}$ to $\mathrm{C^A}$ is $3.0 \times 10^4 < R < 3.2 \times 10^4$, respectively. Therefore we conclude that the inner sphere rotation causes the different transition route from that in the co-rotating system.

Convection patterns of $\mathrm{QP^S}$ in the system allowing the rotation of both spheres is qualitatively similar to that in the co-rotating system at $R = 2.6 \times 10^4$ (Figs. 4.4 and 4.5) in spite of the inner sphere retrograde rotation $\tilde{\Omega}_{\mathrm{in},z} = -7.0 \pm 1.5$, at most 3.4 % against the rotation rate of the reference. In both cases, $E_k^{m=2}$ is the dominant part of the mean kinetic energy density even though the azimuthal wavenumber of the critical mode $m_c = 4$. This means the azimuthal structure of convective solutions becomes larger as the Rayleigh number is increased; this tendency is same as that in Ardes *et al.* [18]. Moreover the amplitudes of the time averaged mean zonal flows are quantitatively similar: $\max\left(\overline{\langle U_\phi \rangle}\right) = +4.38$ and $\min\left(\overline{\langle U_\phi \rangle}\right) = -10.39$ in the system allowing the rotation of both spheres while $\max\left(\overline{\langle u_\phi \rangle}\right) = +4.48$ and $\min\left(\overline{\langle u_\phi \rangle}\right) = -10.53$ in the co-rotating system. However, the magnitude of the propagating velocity in the azimuthal direction of $\mathrm{QP^S}$ in

the system allowing the rotation of both spheres ($\overline{v_p} \simeq -2.0$) is larger than that in the co-rotating system ($\overline{v_p} \simeq -1.5$) by about 33%. This fact that, the propagating velocities are effectively different while the convection patterns and the mean zonal flows are qualitatively similar, appear to be inconsistent with the propagating mechanism proposed in our previous work shown in Chap. 1. Further detailed analyses should be done in order to find the origin of the difference of the propagating velocities of stable QP$^{\mathrm{S}}$s.

As the Rayleigh number is increased to $R = 3.0 \times 10^4$, chaotic solution with equatorial symmetry C$^{\mathrm{S}}$ appears in the system allowing the rotation of both spheres while QP$^{\mathrm{A}}$ does in the co-rotating system.

The convection patterns of QP$^{\mathrm{A}}$ is qualitatively similar to those of QP$^{\mathrm{S}}$ at $R = 2.6 \times 10^4$ in the co-rotating system, because the antisymmetric part of QP$^{\mathrm{A}}$ is very small compared with the symmetric one. However, the dominant frequency of QP$^{\mathrm{A}}$ is five times larger than that of QP$^{\mathrm{S}}$ at $R = 2.6 \times 10^4$ in the co-rotating system.

The typical feature of convective solution C$^{\mathrm{S}}$ is as follows: $E_k^{m=2}$ is averagely the dominant part of the mean kinetic energy density and sometimes the other parts of E_k^m suddenly increase intermittently. When $E_k^{m=2}$ is the dominant part, $\tilde{\Omega}_{\mathrm{in},z}$ keeps negative with fluctuations and $\tilde{\Omega}_{\mathrm{out},z}$ keeps positive with fluctuations, while the rapid inner sphere acceleration and the simultaneous outer sphere deceleration occur intermittently when the other parts of E_k^m suddenly increase. When $E_k^{m=2}$ is dominant, the prograde zonal flows locate near the mid-latitude near the outer sphere while the retrograde zonal flows locate almost all the region near and inside the tangential cylinder [2] and also locate on the equatorial plane near the outer sphere, which is also seen at the convective solution QP$^{\mathrm{S}}$ On the other hand, when E_k^m broads and becomes flat around $m = 5$, the strong prograde zonal flows locate in the vicinity of the poles near the inner sphere while the strong retrograde zonal flows locate in the vicinity of the poles near the outer sphere and also locate on the equatorial plane near the outer sphere. We conclude that this change of the structure of the mean zonal flow causes the sudden acceleration/deceleration of the inner and outer spheres at the convective solutions C$^{\mathrm{S}}$.

As the Rayleigh number is further increased to $R = 3.4 \times 10^4$, chaotic solution with equatorial asymmetry C$^{\mathrm{A}}$ appears in both systems. The behaviour of the convective solution C$^{\mathrm{A}}$s at $R = 3.4 \times 10^4$ in both systems are qualitatively similar to that of C$^{\mathrm{S}}$ in the system allowing the rotation of both spheres, because the antisymmetric part of C$^{\mathrm{A}}$ is relatively small com-

[2] Tangential cylinder means the cylinder tangent to the inner sphere on the equatorial plane.

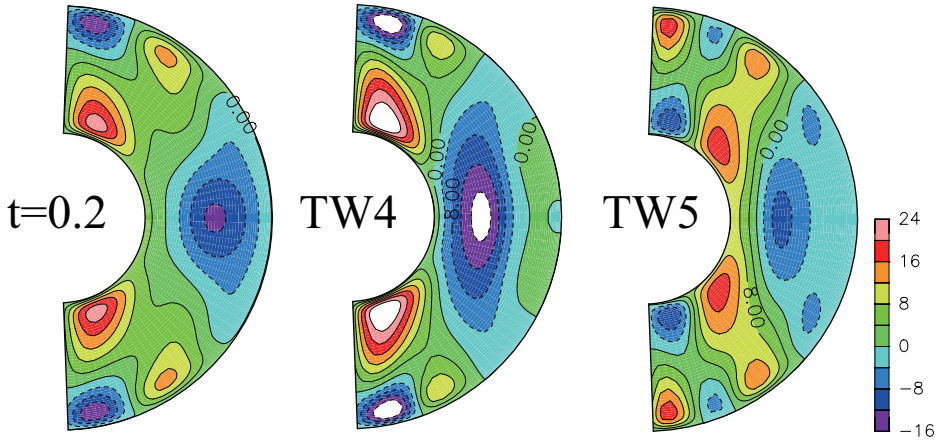

Figure 4.10: Distributions of the mean zonal flows of the unstable traveling wave solutions TW4 and TW5 with that of C^S ($t = 0.2$) at $R = 3.0 \times 10^4$.

pared with the symmetric one in each system. However, the sudden acceleration/deceleration of the inner and outer spheres with the change of distribution of E_k^m occurs more frequently compared with that of C^S at $R = 3.0 \times 10^4$ in the system allowing rotation of both spheres.

Considering the (unstable) traveling wave solutions, we may understand the reason why the sudden inner sphere prograde rotation of the convective solution C^S occurs in the system allowing the rotation of both spheres.

Figure 4.10 shows the distributions of the mean zonal flows of the unstable traveling wave solutions TW4 and TW5 at $R = 3.0 \times 10^4$ in the system allowing the inner sphere rotation, comparing with that of C^S at $t = 0.2$ and $R = 3.0 \times 10^4$. These TW4 and TW5 solutions are bifurcated at the critical point whose critical Rayleigh numbers are $R_c^{m=4} = 6387$ and $R_c^{m=5} = 6585$, respectively, and both propagate in the retrograde direction: $v_p = -8.4$ at TW4 and $v_p = -4.3$ at TW5. The inner sphere rotates in the prograde direction at both traveling wave solutions: $\tilde{\Omega}_{\mathrm{in},z} = +6.2$ at TW4 [3] and $\tilde{\Omega}_{\mathrm{in},z} = +18.3$ at TW5. We found that the strong prograde (retrograde) zonal flows of C^S in the vicinity of the poles near the inner (outer) sphere are qualitatively similar to those of unstable TW4 solution, while $E_k^{m=4}$ is the second largest component in E_k^m (Fig. 4.6). Further quantitative researches should be done, but we expect that the chaotic solution C^S at $R = 3.0 \times 10^4$ in the

[3] Note that the inner sphere rotates in the retrograde direction near the critical region, shown in Fig. 3.2 and 3.3. The transition of the direction of the inner sphere rotation from retrograde to prograde occurs around $R \simeq 2.2 \times 10^4$.

system allowing the rotation of both spheres wanders around the unstable QP^S solution, and intermittently goes away from QP^S to near the unstable traveling wave solutions such as TW4 solutions.

Chapter 5

Conclusion and discussion

In this thesis, we investigated the effects of rotation of the inner and outer spheres on the behaviour of Boussinesq thermal convection in a rotating spherical shell, especially focusing on the bifurcation structure of convective solutions (Chap. 3) and emergence of equatorial asymmetric convective solutions (Chap. 4).

We chose impermeable, no-slip and fixed temperature boundary conditions. The control parameters are as follows: the ratio of inner and outer radii and the Prandtl number are fixed to $\eta = 0.4$ and $P = 1$, respectively, while the square root of the Taylor number τ is varied from 52 to 500, and the Rayleigh number $1.5 \times 10^3 \leq R \leq 3.4 \times 10^4$. The inertial moment of the inner sphere $I_{\rm in}$ is fixed to about 0.22 assumed that the density of the inner sphere is same as that of fluid; this assumption is consistent with the self-gravitational field whose magnitude is proportional to the distance from the center of the shell. The inertial moment of the outer sphere $I_{\rm out}$ is fixed to 100 when the outer sphere rotation is allowed.

In this parameter region, traveling wave solution TW4, which has four-fold symmetry and propagates in the azimuthal direction, bifurcates supercritically at a critical point, whenever the inner sphere can rotate or not (Chaps. 1 and 3). In the system allowing rotation of the inner sphere, the inner sphere rotates in the prograde direction when the rotation rate is small ($\tau \lesssim 160$), while retrograde when the rotation rate is large ($\tau \gtrsim 400$), in the stable region of TW4 solutions. (Figs. 3.2 and 3.3). These rotation directions correspond to the directions of torques on the inner sphere in the co-rotating system (Fig. 2.2), where these torques are generated by the nonlinear term in the energy equation in slowly rotating region and by the azimuthal (longitudinal) component of the nonlinear term in the Navier-Stokes equation in moderately rotating region (Sec. 2.4.1).

The bifurcation structure of TW4 solutions is quantitatively similar to

that in the co-rotating system (Figs. 1.1 and 3.4): TW4s are stable in the region $R_c \leq R \lesssim 1.2 - 2R_c$ depending on the rotation rate, where R and R_c are the Rayleigh number and the critical value, respectively. The convective motions of stable TW4 solutions in the system allowing the inner sphere rotation are also quantitatively similar to those in the co-rotating system (Fig. 3.5). On the other hand, the amplitude of mean zonal flow and the propagating velocity of TW4 solution are effectively changed due to the inner sphere free rotation (Fig. 3.9). This tendency can be explained that the nonlinear effect is small and the behaviour of stable TW4 solutions can be understood with the weakly nonlinear analyses, because the TW4 solutions are stable only near the critical curve. These are quantitatively confirmed in Sec.2.4.2: the inner sphere rotation is $O(\epsilon^2)$ because the zonal flow and torque on the inner sphere are both $O(\epsilon^2)$ in the co-rotating system, where ϵ means the amplitude of the convective motion (Sec. 3.4).

As the Rayleigh number is increased up to around $5R_c$ in moderately rotating case $\tau = 500$, the equatorial asymmetric convection patterns appear both in the co-rotating system and in the system allowing both spheres rotation (Chap. 4). We found that the route from the equatorial symmetric convective solution to the equatorial asymmetric one in the system allowing the rotation of both spheres is different from that in the co-rotating system (Fig. 4.2). In the co-rotating system, as the Rayleigh number is increased around $4R_c - 5R_c$, the convective solutions transit as $\mathrm{QP}^{\mathrm{S}} \rightarrow \mathrm{QP}^{\mathrm{A}} \rightarrow \mathrm{C}^{\mathrm{A}}$, where QP^{S} means the quasi-periodic (or periodic) solution with equatorial symmetry, QP^{A} the quasi-periodic (or periodic) solution with equatorial asymmetry, and C^{A} the chaotic solution with equatorial asymmetry. On the other hand, in the system allowing both spheres rotation, the convective solutions transit as $\mathrm{QP}^{\mathrm{S}} \rightarrow \mathrm{C}^{\mathrm{S}} \rightarrow \mathrm{C}^{\mathrm{A}}$, where C^{S} means the chaotic solution with equatorial symmetry. The transition route in the system where only the inner sphere rotation is permitted is exactly same as that in the system allowing rotation of both spheres. Therefore we conclude that the inner sphere rotation causes the different transition route from that in the co-rotating system.

Considering these behaviours of convective solutions, we conclude that the inner sphere rotation can affect the behaviour of convective solutions effectively, despite the fact that the inertial moment of the inner sphere is much smaller than those of fluid and the outer sphere: $I_{\mathrm{in}} \simeq 0.22$ while $I_{\mathrm{fluid}} \simeq 21.33$ and $I_{\mathrm{out}} = 100$.

We should indicate the importance of investigating the bifurcation structure in this convection model.

We found that, when $R = 3.0 \times 10^4$, the convective solution C^{S} exist in the system allowing the rotation of both the spheres, shown in Fig. 4.6.

When the inner sphere rotates in the retrograde direction with fluctuations ($t = 2.0$), the convection patterns of $\mathrm{C^S}$ are qualitatively similar to those of $\mathrm{QP^S}$ solutions obtained at $R = 2.6 \times 10^4$ except for their amplitudes. On the other hand, when the inner sphere rotates in the prograde direction ($t = 0.2$), the zonal flow structure of $\mathrm{C^S}$ inside the tangential cylinder is qualitatively similar to those of unstable TW4 solution (Fig. 4.10). This suggests that the unstable TW4 solution would be a key to understand the reason why the sudden inner sphere prograde rotation occurs. We expect that this chaotic solution $\mathrm{C^S}$ wanders around the (unstable) $\mathrm{QP^S}$ solution, while intermittently goes near (unstable) traveling wave solutions such as TW4 solution.

In this way, the bifurcated solutions could be a clue to understand a chaotic solution, *i.e.*, investigating the bifurcation structure in this convection system is important not only for understanding the behaviours of the obtained solutions but also could be important for understanding the behaviours of the chaotic solutions. Further detailed analyses for bifurcation structures would leads to better understanding for finite-amplitude convection patterns. Especially, if we could find a traveling wave solution which is the "skeleton" of the quasi-periodic solution $\mathrm{QP^S}$, investigating the stability of this traveling wave solution would bring some information for appearing the $\mathrm{QP^A}$ and $\mathrm{C^S}$ solutions.

Bifurcation structures and behaviours of finite-amplitude convective solutions would be different, especially in more rapid rotation case or in lower Prandtl number, because not only columnar convection pattern but also spiralling columnar convection pattern or equatorially attached convection pattern appears in these region. Behaviours of convective solutions with different inertial moments of both spheres also would be of interests. Note that, if the inertial moment of the inner sphere is changed, we should also change the profile of gravitational field in order to keep the physical consistency. Considering the motions of the center of both spheres, the more physically consistent model could be constructed as a next step toward a more realistic model.

Appendix A

Numerical method

A.1 Numerical method for obtaining the traveling wave solutions

In order to obtain the critical modes, we linearize the governing equations (2.8), (2.9) and (2.10) with respect to the state of rest and the basic temperature profile as follows:

$$\frac{\partial}{\partial t}\hat{A}\boldsymbol{x} = \hat{B}\boldsymbol{x}, \tag{A.1}$$

where the vector $\boldsymbol{x}$ is the dependent variables defined as $\boldsymbol{x} = {}^t[v, w, \Theta]$, and both $\hat{A}$ and $\hat{B}$ are the operators defined as

$$\hat{A} = \begin{bmatrix} \hat{L}_2\Delta & & \\ & \hat{L}_2 & \\ & & P \end{bmatrix},$$

$$\hat{B} = \begin{bmatrix} \Delta^2\hat{L}_2 + \tau\dfrac{\partial}{\partial\phi}\Delta & \tau\hat{Q} & -\hat{L}_2 \\ -\tau\hat{Q} & \Delta\hat{L}_2 + \tau\dfrac{\partial}{\partial\phi} & \\ R\hat{L}_2 & & \Delta \end{bmatrix},$$

respectively. Assuming $\boldsymbol{x} \propto \exp(\sigma t)$ ($\sigma \in \mathbb{C}$), the equations (A.1) becomes as follows:

$$\sigma\hat{A}\boldsymbol{x} = \hat{B}\boldsymbol{x}. \tag{A.2}$$

This is an eigenvalue problem and the real part of σ is the growth rate and the imaginary part is the frequency of the eigenmode. We expand the dependent

variables v, w and Θ with the combinations of Chebyshev polynomials, which satisfy the boundary conditions (2.13), in the radial direction (described in the next section) and the spherical harmonics in the longitudinal and latitudinal direction, respectively. The equations (A.2) are separated into those for each longitudinal wavenumber m. Therefore, the critical Rayleigh numbers R_c^m for each longitudinal wavenumber m are determined, and the critical Rayleigh number is defined as $R_c \equiv \min_{m\in\mathbb{Z}_{\geq 0}} R_c^m$. We find the value of R_c^m by the bisection method. The truncation wavenumber of spherical harmonics L and the maximum degree of the Chebyshev polynomials N are both fixed to 25, while $(N, L) = (30, 30)$ is used in some numerical calculations in order to verify the results.

In order to obtain the nonlinear traveling waves bifurcating at the critical points, we assume that the propagating velocity of the nonlinear traveling wave in the longitudinal direction is v_p. Then they become stationary solutions in the frame of reference moving with the longitudinal velocity v_p with respect to the rotating frame. We transform the time t and longitude ϕ into $T \equiv t$ and $\Phi \equiv \phi - v_p t$, then the governing equations become as follows;

$$\left[\frac{\partial}{\partial T} - v_p \frac{\partial}{\partial \Phi}\right] \hat{L}_2 w = \Delta \hat{L}_2 w + \tau \frac{\partial}{\partial \Phi} w - \tau \hat{Q} v - \boldsymbol{r} \cdot [\nabla \times ((\boldsymbol{u} \cdot \nabla)\boldsymbol{u})], \tag{A.3}$$

$$\left[\frac{\partial}{\partial T} - v_p \frac{\partial}{\partial \Phi}\right] \hat{L}_2 \Delta v = \Delta \hat{L}_2 \Delta v + \tau \frac{\partial}{\partial \Phi} \Delta v + \tau \hat{Q} w - \hat{L}_2 \Theta + \boldsymbol{r} \cdot [\nabla \times \nabla \times ((\boldsymbol{u} \cdot \nabla)\boldsymbol{u})], \tag{A.4}$$

$$P\left[\frac{\partial}{\partial T} - v_p \frac{\partial}{\partial \Phi}\right] \Theta = R \hat{L}_2 v + \Delta \Theta - P(\boldsymbol{u} \cdot \nabla)\Theta, \tag{A.5}$$

The boundary conditions (2.13) are invariant because the dependent variables are all scalar. Therefore we find the stationary solution of the equations (A.3), (A.4) and (A.5) with the boundary conditions (2.13). Note that in the equations (A.3), (A.4) and (A.5), v_p is also an unknown variable, and this problem is a nonlinear eigenvalue problem.

In order to solve the nonlinear equations (A.3), (A.4) and (A.5) with the boundary conditions (2.13), we use the Galerkin-spectral method again. The expansion functions are the same as in the computation of the critical modes. For calculation of the nonlinear terms, we use the spectral transform method, that is, the nonlinear terms are evaluated in the physical space and are converted back into the spectral space. Since the nonlinear terms cause the interaction between the different longitudinal wavenumbers, the calculation of the nonlinear solutions needs much computer resources than

those of the critical modes. The stationary solution satisfies the equations (A.3), (A.4) and (A.5) with the time derivative terms dropped. We denote the spectral coefficients of the expansion of the dependent variables as the vector $\boldsymbol{s}$, then the stationary solution $\boldsymbol{s}_0$ satisfy the following equations,

$$\mathbf{0} = \frac{d\boldsymbol{s}_0}{dT} = \boldsymbol{F}(\boldsymbol{s}_0, v_p), \tag{A.6}$$

where $\boldsymbol{F}$ are quadratic functions of $\boldsymbol{s}$ and v_p, whose dimension is the same as the number of the component of $\boldsymbol{s}$. Therefore, the equations (A.6) have one arbitrariness, which corresponds to the arbitrariness of the origin of the longitude Φ. In order to eliminate the arbitrariness, we lock the phase of the complex spectral coefficient whose absolute value is maximum among all the spectral coefficients in the critical state as 0[rad]. We use the Newton method to solve the nonlinear equations (A.6). When the Rayleigh number is varied with τ fixed, we choose the critical mode or the nonlinear traveling wave solution obtained before as the initial guess in the Newton method. Also, we investigate the stability of the obtained traveling wave by calculating the eigenvalues of the linearized equations around the traveling wave solution.

A.2 The expansion functions in the radial direction

On calculating the critical modes and the finite amplitude traveling wave solutions, we expand the dependent variables v, w and Θ as follows,

$$\begin{aligned}
v(r,\theta,\phi,t) &\equiv \sum_{l=1}^{L}\sum_{m=-l}^{l}\sum_{n=0}^{N-4} V_{l,n}^{m}(t)Y_l^m(\theta,\phi)\zeta_n(x(r)),\\
w(r,\theta,\phi,t) &\equiv \sum_{l=1}^{L}\sum_{m=-l}^{l}\sum_{n=0}^{N-2} W_{l,n}^{m}(t)Y_l^m(\theta,\phi)\psi_n(x(r)),\\
\Theta(r,\theta,\phi,t) &\equiv \sum_{l=0}^{L}\sum_{m=-l}^{l}\sum_{n=0}^{N-2} \Theta_{l,n}^{m}(t)Y_l^m(\theta,\phi)\xi_n(x(r)),
\end{aligned}$$

where N means the maximum degree of Chebyshev polynomials and L means the truncation wavenumber of the spherical harmonics (the time t and the longitude ϕ are transformed into T and Φ respectively in solving the nonlinear traveling wave). The relation between r and x is defined as

$$\begin{aligned}
r = r(x) &\equiv \frac{r_{\mathrm{in}} + r_{\mathrm{out}}}{2} + \frac{r_{\mathrm{out}} - r_{\mathrm{in}}}{2}x,\\
\Leftrightarrow \quad x(r) &= 2r - r_{\mathrm{in}} - r_{\mathrm{out}},
\end{aligned}$$

and the basis functions ζ_n, ψ_n, ξ_n are as follows:

$$\begin{aligned}
\zeta_n(x) &\equiv T_n(x) - \frac{2n+4}{n+3} T_{n+2}(x) + \frac{n+1}{n+3} T_{n+4}(x), \\
\psi_n(x) &\equiv T_n(x) - T_{n+2}(x), \\
\xi_n(x) &\equiv T_n(x) - T_{n+2}(x),
\end{aligned}$$

where $T_n(x) = \cos(n \arccos(x))$ is the Chebyshev polynomial of degree n. With the above expansion functions in the radial direction, the boundary conditions (2.13) are satisfied automatically.

Acknowledgements

I would like to express my deep respect for Prof. Michio Yamada. His fruitful and suggestive advice with his enormous background knowledge has always encouraged me in my studies during my studentship at Kyoto University.

I also would like to express my great appreciation for Prof. Shin-ichi Takehiro. His attitude to research as a scholar, as well as his deep and perceptive insight into research objects, have always inspired me to make efforts to study more.

I appreciate Dr. Yoshitaka Saiki, Dr. Miki U. Kobayashi, Dr. Kiori Obuse and Dr. Youhei Sasaki, who have given me a lot of helpful comments on my research. I also would like to thank my colleagues Masanobu Inubushi, Eiichi Sasaki and Kenta Ishimoto for sharing the great experience at the Research Institute for Mathematical Sciences, Kyoto University.

My heartfelt appreciation goes to my families, who have been always supporting me in many aspects throughout my life.

In the last, I am grateful to the RIMS for providing me a stimulating and brilliant research environment. I sincerely treasure the experience of working in this wonderful institute. I will always be proud of having been a member of the RIMS.

Numerical calculations were performed with the computer systems of the Institute for Information Management and Communication (IIMC) of Kyoto University and with the computer systems of Research Institute for Mathematical Sciences (RIMS), Kyoto University. For the calculations of the critical modes, the nonlinear finite-amplitude solutions and the weakly nonlinear analyses, we used the library for spectral transform 'ISPACK' (http://www.gfd-dennou.org/arch/ispack/) [54] and its Fortran90 wrapper library 'SPMODEL library' (http://www.gfd-dennou.org/library/spmodel/) [55]. The subroutines of LAPACK (http://www.netlib.org/lapack/) and the Fujitsu SSL Ⅱ were used in the calculation of eigenvalues to obtain the critical modes and to examine the stability of solutions. The products of the Dennou Ruby project (http://www.gfd-dennou.org/library/ruby/) were used to

draw the figures. This work was supported by a Grant in-Aid for the Global COE Program “Fostering top leaders in mathematics – broadening the core and exploring new ground” from the Ministry of Education, Culture, Sports, Science and Technology (MEXT) of Japan.

References

[1] S. Chandrasekhar, "Hydrodynamic and Hydromagnetic stability," Oxford Univ. Press, pp654 (1961).

[2] K. Kimura, S. Takehiro and M. Yamada, "Stability and bifurcation diagram of Boussinesq thermal convection in a moderately rotating spherical shell," Phys. Fluids, **23**, 074101 (2011).

[3] J. Yano, "Asymptotic theory of thermal convection in rapidly rotating systems," J. Fluid Mech., **243**, 103 (1992).

[4] K. Zhang, "On coupling between the Poincare equation and the heat equation," J. Fluid Mech., **268**, 211 (1994).

[5] K. Zhang, "On coupling between the Poincare equation and the heat equation: non-slip boundary condition," J. Fluid Mech., **284**, 239 (1995).

[6] C. A. Jones, A. M. Soward and A. I. Mussa, "The onset of thermal convection in a rapidly rotating sphere," J. Fluid Mech., **405**, 157 (2000).

[7] E. Dormy, A. M. Soward, C. A. Jones, D. Jault and P. Cardin, "The onset of thermal convection in rotating spherical shells," J. Fluid Mech., **501**, 43 (2004).

[8] K. K. Zhang and X. Liao, "A new asymptotic method for the analysis of convection in a rapidly rotating sphere," J. Fluid Mech., **518**, 319 (2004).

[9] K. K. Zhang, X. Liao and F. H. Busse, "Asymptotic solutions of convection in rapidly rotating non-slip spheres," J. Fluid Mech., **578**, 371 (2007).

[10] S. Takehiro and Y.-Y. Hayashi, "Boussinesq convection in rotating spherical shells –a study on the equatorial superrotation," The Earth's

Central Part: Its Structure and Dynamics, edited by T. Yukutake, 123 (1995).

[11] P. H. Roberts, "On the thermal instability of a rotating-fluid sphere containing heat sources," Phil. Trans. R. Soc. Lond. A, **263**, 93 (1968).

[12] F. H. Busse, "Differential rotation in stellar convection zones," Astrophys. J., **159**, 629 (1970).

[13] F. H. Busse, "Thermal instabilities in rapidly rotating systems," J. Fluid Mech., **44**, part3, 441 (1970).

[14] F. H. Busse, 1973 "Differential rotation in stellar convection zones Ⅱ," Astron. Astrophys., **28**, 27 (1973).

[15] G. Geiger and F. H. Busse, "On the onset of thermal convection in slowly rotating fluid shells," Geophys. Astrophys. Fluid Dynamics, **18**, 147 (1981).

[16] K. Zhang, "Spiralling columnar convection in rapidly rotating spherical fluid shells," J. Fluid Mech., **236**, 535 (1992).

[17] K. Zhang and F. H. Busse, "On the onset of convection in rotating spherical shells," Geophys. Astrophys. Fluid Dynamics, **39**, 119 (1987).

[18] M. Ardes, F. H. Busse and J. Wicht, "Thermal convection in rotating spherical shells," Physics of the Earth and Planetary Interiors, **99**, 55 (1997).

[19] R. Simitev and F. H. Busse, "Patterns of convection in rotating spherical shells," New Journal of Physics, **5**, 97.1 (2003).

[20] M. Net, F. Garcia and J. Sánchez, "On the onset of low-Prandtl-number convection in rotating spherical shells: non-slip boundary conditions," J. Fluid Mech., **601**, 317 (2008).

[21] F. Garcia, J. Sánchez and M. Net, "Antisymmetric polar modes of thermal convection in rotating spherical fluid shells at high Taylor numbers," Phys. Rev. Lett., **101**, 194501 (2008).

[22] U. Christensen, "Zonal flow driven by strongly supercritical convection in rotating spherical shells," J. Fluid Mech, **470**, 115 (2002).

[23] M. Heimpel and J. Aurnou, "Turbulent convection in rapidly rotating spherical shells: A model for equatorial and high latitude jets on Jupiter and Saturn," Icarus, **187**, 540 (2007).

[24] J. Aurnou, M. Heimpel and J. Wicht, "The effects of vigorous mixing in a convective model of zonal flow on the ice giants," Icarus, **190**, 110 (2007).

[25] T. Miyagoshi, A. Kageyama and T. Sato, "Zonal flow formation in the Earth's core," Nature **463**, 793 (2010).

[26] F. H. Busse, "A simple model of convection in the Jovian atmosphere," Icarus **29**, 255 (1976).

[27] F. H. Busse, "A model of mean zonal flows in the major planets," Geophys. Astrophys. Fluid Dynamics, **23**, 153 (1983).

[28] F. H. Busse, "Convection-driven zonal flows in the major planets," PAGEOPH, **121**, 375 (1983).

[29] C. C. Porco, R. A. West, A. McEwen, A. D. Del Genio, A. P. Ingersoll, P. Thomas, S. Squyres, L. Dones, C. D. Murray, T. V. Johnson, J. A. Burns, A. Brahic, G. Neukum, J. Veverka, J. M. Barbara, T. Denk, M. Evans, J. J. Ferrier, P. Geissler, P. Helfenstein, T. Roatsch, H. Throop, M. Tiscareno, and A. R. Vasavada, "Cassini imaging of Jupiter's atmosphere, satellites, and rings," Science **299**, 1541 (2003).

[30] A. Sanchez-Lavega, J. F. Rojas and P. V. Sada, "Saturn's zonal winds at cloud level," Icarus **147**, 405 (2000).

[31] H. B. Hammel, K. Rages, G. W. Lockwood, E. Karkoschka and I. de Peter, "New measurements of the winds of Uranus," Icarus **153**, 229 (2001).

[32] H. B. Hammel, I. de Peter, S. Gibbard, G. W. Lockwood and K. Rages, "Uranus in 2003: Zonal winds, banded structures and discrete features," Icarus **175**, 534 (2005).

[33] L. A. Sromovsky, P. M. Fry, T. E. Dowling, K. H. Baines and S. S. Limaye, "Coordinated 1996 HST and IRTF imaging of Neptune and Triton Ⅲ. Neptune's atmospheric circulation and cloud structure," Icarus **149**, 459 (2001).

[34] A. Tilgner and F. H. Busse, "Finite-amplitude convection in rotating spherical fluid shells," J. Fluid Mech., **332**, 359 (1997).

[35] E. Grote and F. H. Busse, "Dynamics of convection and dynamos in rotating spherical fluid shells," Fluid Dynamics Research, **28**, 349 (2001).

[36] P. Chossat, "Bifurcation and stability of convective flows in a rotating or not rotating spherical shell," SIAM J. Applied Math., **37**, No.3, 624 (1979).

[37] S. Takehiro, "On the retrograde propagation of critical thermal convection in a slowly rotating spherical shell," J. Fluid Mech., **659**, 505 (2010).

[38] J. Tromp, "Inner-core anisotropy and rotation," Annu. Rev. Earth Planet. Sci., **29**, 47 (2001).

[39] A. Souriau, R. Garcia and G. Poupinet, "The seismological picture of the inner core: structure and rotation," C.R.Geoscience, **335**, 51 (2003).

[40] J. Zhang, X. Song, Y. Li, P. G. Richards, X. Sun and F. Waldhauser, "Inner core differential motion confirmed by earthquake waveform doublets," Science, **309**, 1357 (2005).

[41] G. A. Glatzmaier and P. H. Roberts, "A three-dimensional convective dynamo solution with rotating and finitely conducting inner core and mantle," Phys. Earth Planet. Inter., **91**, 63 (1995).

[42] J. Aurnou and P. Olson, "Control of inner core rotation by electromagnetic, gravitational and mechanical torques," Phys. Earth Planet. Inter., **117**, 111 (2000).

[43] R. Hollerbach, "A spectral solution of the magneto-convection equations in spherical geometry," Int. J. Numer. Meth. Fluids, **32**, 773 (2000).

[44] U. R. Christensen, J. Aubert, P. Cardin, E. Dormy, S. Gibbons, G. A. Glatzmaier, E. Grote, Y. Honkura, C. Jones, M. Kono, M. Matsushima, A. Sakuraba, F. Takahashi, A. Tilgner, J. Wicht, K. Zhang, "A numerical dynamo benchmark," Phys. Earth Planet. Inter., **128**, 25 (2001).

[45] J. Aubert and M. Dumberry, "Steady and fluctuating inner core rotation in numerical geodynamo models," Geophys. J. Int., **184**, 162 (2011).

[46] K. Araki, S. Yanase and J. Mizushima, "Symmetry breaking by differential rotation and saddle-node bifurcation of the thermal convection in a spherical shell," J. Phys. Soc. Japan, **65**, No.12, 3862 (1996).

[47] S. Takehiro and Y.-Y. Hayashi, "Mean zonal flows excited by critical thermal convection in rotating spherical shells," Geophys. Astrophys. Fluid Dynamics, **90**, 43 (1999).

[48] K. Kimura, S. Takehiro and M. Yamada, "Torques on the inner and outer spheres induced by the Boussinesq thermal convection in a rotating spherical shell," J. Phys. Soc. Japan, **81**, 084401 (2012).

[49] L. D. Landau and E. M. Lifshitz, "Fluid Mechanics, Second edition: Volume 6 (Course of Theoretical Physics)," Butterworth-Heinemann (1987).

[50] I. Proudman, "The almost-rigid rotation of viscous fluid between concentric spheres," J. Fluid Mech., **1**, 505 (1956).

[51] K. Stewartson, "On almost rigid rotations Part 2," J. Fluid Mech., **26**, 131 (1966).

[52] R. Hollerbach, "Magnetohydrodynamic Ekman and Stewartson layers in a rotating spherical shell," Proc. R. Soc. Lond. A, **444**, 333 (1994).

[53] E. Dormy, P. Cardin and D. Jault, "MHD flow in a slightly differentially rotating spherical shell, with conducting inner core, in a dipolar magnetic field," Earth Planet. Sci. Lett., **160**, 15 (1998).

[54] K. Ishioka, ispack-0.96, http://www.gfd-dennou.org/arch/ispack/, GFD Dennou Club (2011).

[55] S. Takehiro, Y. SASAKI, Y. Morikawa, K. Ishioka, M. Odaka, Y.O. Takahashi, S. Nishizawa, K. Nakajima, M. Ishiwatari and Y.-Y. Hayashi, SPMODEL Development Group, Hierarchical Spectral Models for GFD (SPMODEL), http://www.gfd-dennou.org/library/spmodel/, GFD Dennou Club (2011).